T2K-TN-460-v3.0
September 25, 2023

A Markov Chain Monte Carlo oscillation data analysis using SK atmospheric and T2K beam neutrinos

Daniel Barrow[1], Aoi Eguchi[3], Mo Jia[2], Junjie Jiang[2], Wei Shi[2], Michael Wilking[2], and Clarence Wret[1]

[1]University of Oxford, UK
[2]Stony Brook University, USA
[3]University of Tokyo, Japan

September 25, 2023

Todo list

Abstract

This document describes the fit to real data of T2K's near and far detector beam samples, combined with the SK atmospheric samples. It also covers the updated sensitivity (Asimov A fit), and the implementation of model updates. Comparisons to the T2K OA2020 result and the analysis from the P-Theta group are also documented. For the atmospheric analysi, the full SK-IV live time of 3244.4 days is used. For the far-detector analysis, 1.9664×10^{21} POT in FHC, 1.6346×10^{21} POT in RHC is used, corresponding to T2K beam runs 1-10. For the near-detector analysis, 1.1531×10^{21} POT in FHC and 8.336×10^{20} POT in RHC is used, corresponding to runs 2-9. Asimov and data fit results include smearing of Δm^2_{32} from fake-data studies, and results with and without reactor constraint are studied. The impact of a flat prior on $\sin \delta_{\rm CP}$ and a flat prior on $\delta_{\rm CP}$ is also studied for the Jarlskog invariant.

The fit to data with the reactor constraint on $\sin^2 \theta_{13}$ applied finds a Bayes factor of normal ordering over inverted ordering $B(\mathrm{NO/IO})$ of 7.33. This compares to the T2K

results of $B(\mathrm{NO/IO}) = 4.2$ in the 2020 analysis. $\delta_{\mathrm{CP}} = 0, \pi$ is excluded above 2σ with a flat prior on δ_{CP} and the 2σ level is just included with a flat prior on $\sin\delta_{\mathrm{CP}}$. A Jarlskog invariant of $J = 0$ is excluded above 2σ with a flat prior on δ_{CP}, and is just excluded at 2σ with a flat prior on $\sin\delta_{\mathrm{CP}}$. The Bayes factor $B[(\sin\delta_{\mathrm{CP}} < 0)/(\sin\delta_{\mathrm{CP}} \geq 0)]$ is 50.0 with the reactor constraint applied and a flat prior on δ_{CP}. The Bayes factor of upper octant over lower octant $B(\mathrm{UO/LO})$ is 1.78, which shows a weaker preference of the upper octant compared to OA2020 [1] ($B(\mathrm{UO/LO}) = 3.36$), due to SK's preference for lower octant and T2K's preference for upper octant. The posterior predictive p-values find that the samples are well-predicted by the model, with an overall $p = 0.42$ for the rate-based p-value, and $p = 0.11$ for the shape-based p-value.

Contents

1 Introduction

This note documents the results and discussion of the joint-fit of near detector samples (ND280 data from runs 2-9) and far detector samples (5 T2K beam samples from runs 1-10 and 18 SK atmospheric samples of 3224.4 days from SK-IV) performed in MaCh3 framework.

MaCh3 is an oscillation fitter which uses Bayesian inference and Markov chain Monte Carlo (MCMC) to sample the posterior probability in the high dimensional systematic phase space and using marginalisation to estimate the oscillation parameters posterior probability distributions in the T2K experiment. It is extended to simultaneously fit SK atmospheric and T2K near and far detector samples [2]. Running MCMC for smooth enough contours requires a large amount of computing resources. For results presented in this note, we utilized both the GPU and CPU resources from ComputeCanada clusters and Summit cluster.

The joint fit samples are discussed in further detail in TN428 [3]. The oscillation probability calculation method is documented in TN425 [4]. The joint-fit flux and cross-section model originally described in TN422 [5] and is updated in TN456 [6]. This work is based on the updated joint fit model and the implementation of the updates in MaCh3 framework is documented in Sec. 2. The analysis methods in this work are mostly the same as in the sensitivity studies documented in TN426 [2] and this note studies the sensitivity with the model updates, and the data fit.

Sec. 3 describes the Asimov A fit results for both with and without reactor constraint of $\sin^2\theta_{13}$. Both one dimensional and two dimensional contours of oscillation parameters are presented. In addition, the Jarlskog invariant posterior probability distributions are also presented. Bayes factors of octant hypotheses, mass ordering and CP violation are calculated and discussed.

Sec. 4 describes the data fit results for both with and without reactor constraint of $\sin^2\theta_{13}$. Both one dimensional and two dimensional contours of oscillation parameters are presented. In addition, the Jarlskog invariant posterior probability distributions are also presented. Bayes factors of octant hypotheses, mass ordering and CP violation are calculated and discussed. Effect of reactor constraint is discussed by overlaying the contours with and without the constraint. Finally, the joint-fit data fit results (with reactor constraint) are compared to OA2020 MaCh3 results (T2K-only fit, see TN393 [1]).

Sec. 5 describes the comparison of the joint-fit data fit results between MaCh3 and P-Theta as well as OA2020 results (TN393 [1] and TN397 [7]). Discussion of the results differences between fitters is documented as well.

2 Model updates implementation in MaCh3

This section describes the implementation of model updates in the MaCh3 framework. The motivation of the updates can be found in the joint-fit model updates TN456 [6]Sec. 2. All involved systematics can be found in the joint-fit fitter validation TN471 [8] (Tab. 6, 7, 8).

2.1 Updates of atmospheric detector errors

Joint-fit analysis decides to use the same fiTQun version and CCQE model for SK and T2K samples as T2K official analysis. Hence, SK atmospheric detector errors need to be re-evaluated. The atmospheric detector errors are hard coded in MaCh3 and thus updating the values is straight-forward. The updated errors are documented in Sec. 3 of TN456 [6] and validated through fitter validation recorded in TN471 [8].

2.2 Treatment of SubGeV 1Re1de excess

To deal with the data/MC discrepancy observed in down-going SubGeV CC1pi dominated sample, three different ways are adopted. Details are documented in Sec. 4.4 from TN456 [6].

2.2.1 Updated Adler angle dials

The ad-hoc Adler angle uncertainty was introduced in the model for the sensitivity study last year. In the latest model, the previous Adler angle dial is split into two dials with different dependence on lepton momentum. The parameterization and prior constraints are also changed.

New splines are generated using the same weight files as P-Theta (see Sec. 4.4.4 in TN456 [6] v1.1). The Adler angle dials are implemented as splined cross-section systematics that apply to CC1pi and NC1pi true resonance interaction modes (including both charged and neutral pion) for all beam samples and atmospheric SubGeV samples. Validation is done and documented in fitter validation TN471 [8].

2.2.2 New SK PID errors

To account for the potentially poor performance of e/μ PID at low lepton momentum for CC1π dominated samples, two 50% correlated systematics are developed (see TN456 [6]). Two migration dials are implemented; one moves events between the atmospheric single ring one decay electron and muon-like samples, and the other moves events between the beam FHC 1Re1de and FHC(RHC)1Rmu samples.

Technically, these two systematics are implemented in the same class as the correlated detector systematics and no correlation is applied between them and other detector systematics.

2.2.3 MC with new decay electron cut

The T2K MC was produced with a new cut on the delayed hit clusters reconstructed by fiTQun to reduce the background from neutron capture signals in tagging decay electrons. Similarly, the SK ATMPD group updated the atmospheric MC with this new cut. Thus, the input MC for joint-fit is now updated with this new cut.

Technically, MaCh3 updates a few reconstructed fiTQun variables in the reading in MC inputs process accordingly. Same input is used by other fitters in joint-fit and event rates validation between fitters is done.

2.3 Correlated far detector systematics

The motivation and validation of the correlated far-detector model are documented in Sec. 5 of TN456 [6]. In the current MaCh3 framework, systematics are divided into un-correlated groups so that each group has its own class to store all the necessary methods. To implement this correlated model, a new class of the correlated detector systematics has been developed to implement the correlation, which inherit most of the methods for each class of systematics from the previous un-correlated model. The validation of this implementation can be found in the fitter validations, documented in TN471 [8].

MaCh3 uses different sets of T2K beam detector systematics compared to P-Theta and Osc3++ due to the different fit-binning variables used in MaCh3 and P-Theta (documented in TN456 [6]). MaCh3 uses the set of systematics binned in reconstructed energy for all T2K beam samples (TN456 [6] Tab. 8) while P-Theta and Osc3++ bin in reconstructed lepton momentum for beam e-like samples and reconstructed energy for beam muon-like samples (TN456 [6] Tab. 9).

Another technical difference is that the covariance matrix of the SK detector systematics used in MaCh3 and P-Theta are different in that MaCh3 does not absorb the effect of secondary interaction and photo-nuclear systematics into the matrix while P-Theta does. The SI and photo-nuclear systematics in MaCh3 are instead implemented in another class dedicated to cross-section systematics. This has no impact on physics conclusions in the oscillation analysis, but should be kept in mind when comparing the impact due to difference classes of systematics.

3 Results from fitting Asimov data

The "Asimov data" refers to the far-detector predictions built by reweighting the simulated far-detector samples using the post-BANFF tune, and applying the set of known oscillation parameters in Tab. 1. The set of oscillation parameters named "Asimov A" are applied to produce all results shown in this section. The parameter sets are the same as used in the sensitivity studies TN426 [2]. The Asimov studies are present for two main purposes: validation of the analysis (since the parameter set that generated the data is known), and to provide an estimate of the sensitivity assuming no statistical fluctuations.

Parameter	Asimov A	Asimov B
$\sin^2\theta_{12}$	0.307	0.307
$\sin^2\theta_{23}$	0.528	0.45
$\sin^2\theta_{13}$	0.0218	0.0218
Δm^2_{12} (eV^2)	7.53×10^{-5}	7.53×10^{-5}
Δm^2_{23} (eV^2)	2.509×10^{-3}	2.509×10^{-3}
δ_{CP}	-1.601	0.0

Table 1: Oscillation parameter sets Asimov A and B, set A is used throughout this analysis.

When running an Asimov fit, MaCh3 fits the far-detector Asimov data and the near-detector real data simultaneously. Hence, the results are comparable to the P-Theta Asimov studies using the post-BANFF data fit constraints, with the small caveat of there being slightly different approaches in MaCh3 and BANFF's ND treatment. The full MaCh3 ND treatment can be found in the near-detector fit note, TN395 [9], and some details specific to the joint fit with SK are provided in the sensitivity studies note, TN426 [2].

Due to the model updates—especially the correlated detector systematics—work was done to ensure reasonable behaviour of the MCMC fitting technique of all systematics by looking at the traces of total negative log-likelihood (-LLH) and parameter values, and the autocorrelations for all parameters, from a series of test chains. The aim of the tuning was to achieve 0.2 autocorrelation after 20,000 lag, with no parameters behaving significantly differently to others whilst maintaining high acceptance rates. This aim was achieved.

The final Markov Chains were run such that one chain started from where a previous chain stopped due to the maximum computing time on the computing clusters. The deepest chains were 550,000 steps deep. The test-chains that set the parameter step-sizes were not included in the final Markov Chains that produced the result. For the Asimov fit, a total of 384 independent chains were run in parallel, producing 203,320,244 steps in total including the burn-in period of 80,000 steps per independent chain. This gave 172,599,860 steps after burn-in in total. For results shown in this section, only post burn-in steps are used. Good acceptance rates ($\sim 16-20\%$) and relatively short burn-in periods (80,000 steps) were achieved. The trace of the total negative log-likelihood of all chains for the Asimov A analysis are shown in Fig. 1.

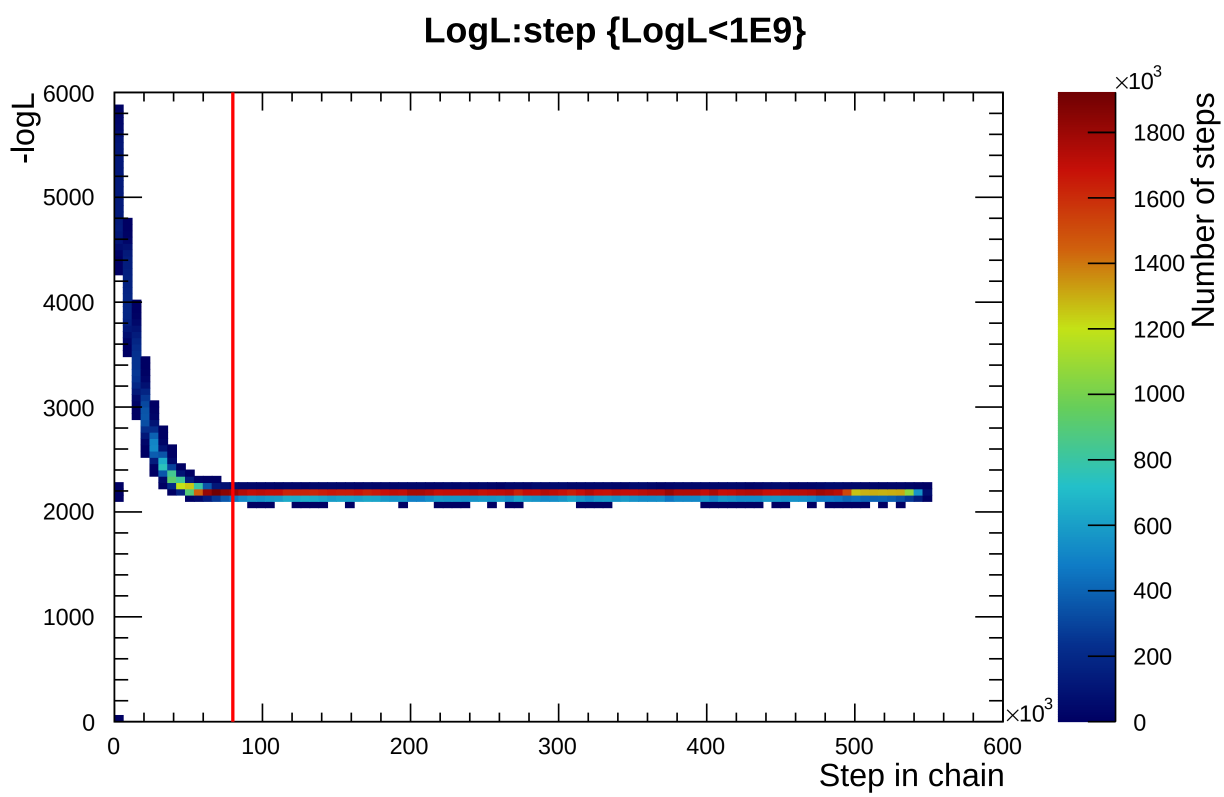

Figure 1: Collection of the traces of the negative log total likelihood from 384 independent chains in the Asimov A fit. The red vertical line shows the chosen burn-in cut at 80,000 steps.

This section first presents Asimov results with the reactor constraint applied, and then without it applied.

3.1 Results applying the reactor constraint

For these results, the reactor constraint on $\sin^2\theta_{13}$ is used with the same value as the T2K OA2020 analysis TN393 [1] from the PDG [10]; $\sin^2\theta_{13} = 0.0218 \pm 0.0007$.

3.1.1 Parameter constraints

Each parameter constraint in this section is shown in normal ordering ($\Delta m^2_{32} > 0$), inverted ordering ($\Delta m^2_{32} < 0$), and over bother orderings.

One-dimensional posteriors Fig. 2, Fig. 3, Fig. 4 and Fig. 5 show the marginalised one-dimensional posterior probability for δ_{CP}, Δm^2_{32}, $\sin^2\theta_{13}$ and $\sin^2\theta_{23}$, respectively.

For the δ_{CP} result, $\sin\delta_{\mathrm{CP}} = 0$ is excluded at exactly 2σ over both orderings. For $\sin^2\theta_{23}$, the correct octant is found, although both octants are well within the 1σ credible interval in both orderings.

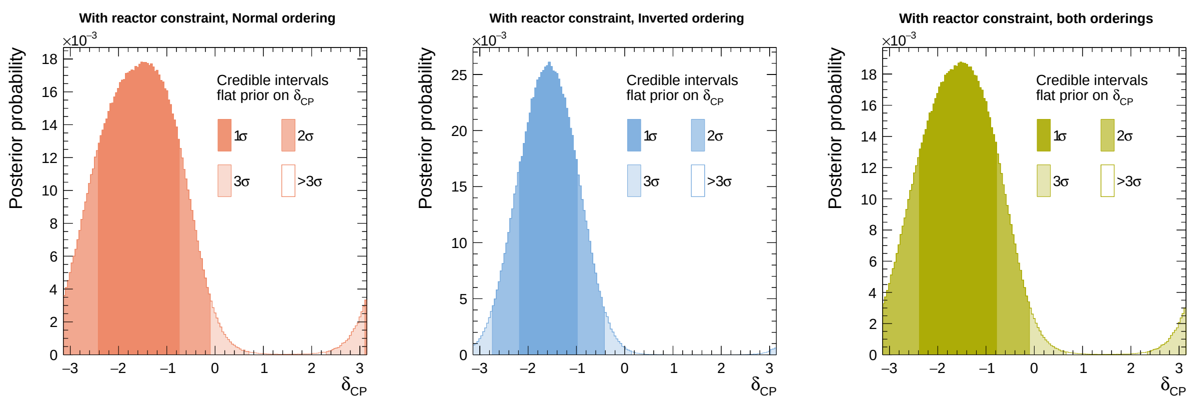

Figure 2: δ_{CP} for the Asimov A analysis, with the reactor constraint applied, for normal (left), inverted (center), and both (right) orderings.

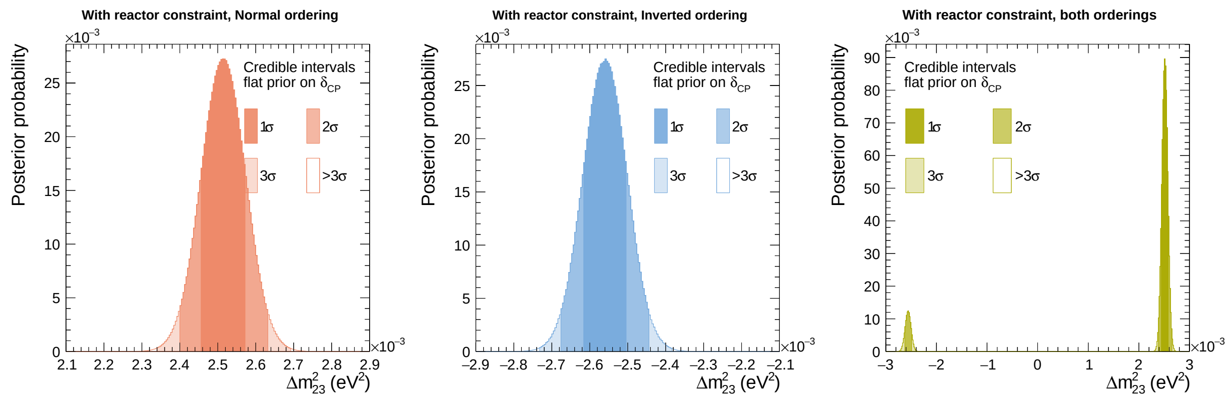

Figure 3: Δm^2_{32} for the Asimov A analysis, with the reactor constraint applied, for normal (left), inverted (center), and both (right) orderings.

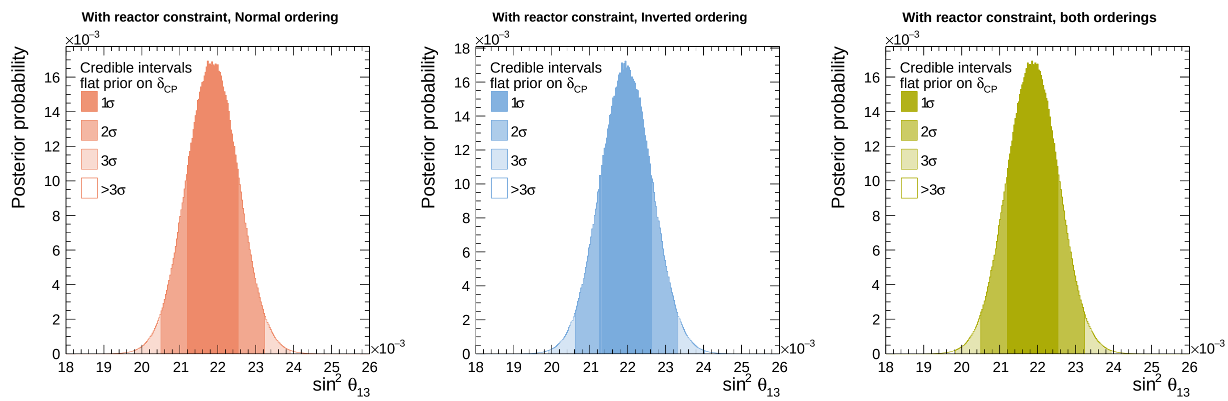

Figure 4: $\sin^2 \theta_{13}$ for the Asimov A analysis, with the reactor constraint applied, for normal (left), inverted (center), and both (right) orderings.

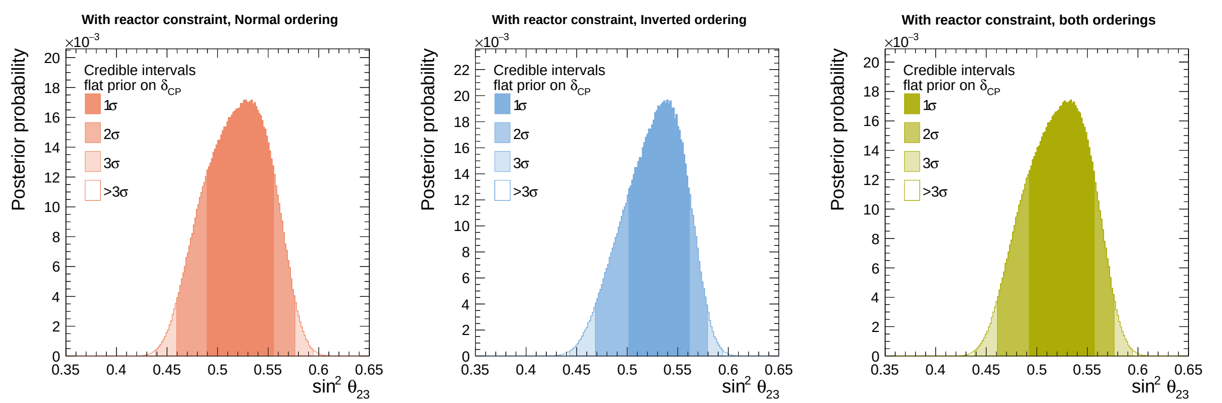

Figure 5: $\sin^2 \theta_{23}$ for the Asimov A analysis, with the reactor constraint applied, for normal (left), inverted (center), and both (right) orderings.

The Jarlskog invariant The posterior distribution of Jarlskog invariant, which is defined as:

$$J = s_{13}c_{13}^2 s_{12}c_{12}s_{23}c_{23}\sin\delta_{CP} \tag{1}$$

where s_{ij} refers to $\sin\theta_{ij}$ and c_{ij} refers to $\cos\theta_{ij}$. More detailed description can be found in TN393 [1] (Appendix H in v9).

Fig. 6 and Fig. 7 show the marginalised Jarlskog invariant (J) posterior for normal ordering, inverted ordering and both ordering with flat prior on $\delta_{\rm CP}$ and $\sin\delta_{\rm CP}$, respectively. As in the mainline T2K analysis, the marginal likelihood for J is computed after the MCMC is run by computing J for each step in the chain after burn-in.

As was found in Fig. 2, $\sin\delta_{\rm CP} = 0 (J = 0)$ is just excluded at 2σ credible interval over both orderings with a flat prior in $\delta_{\rm CP}$. For the prior flat in $\sin\delta_{\rm CP}$, $J = 0$ is included in the 2σ credible interval.

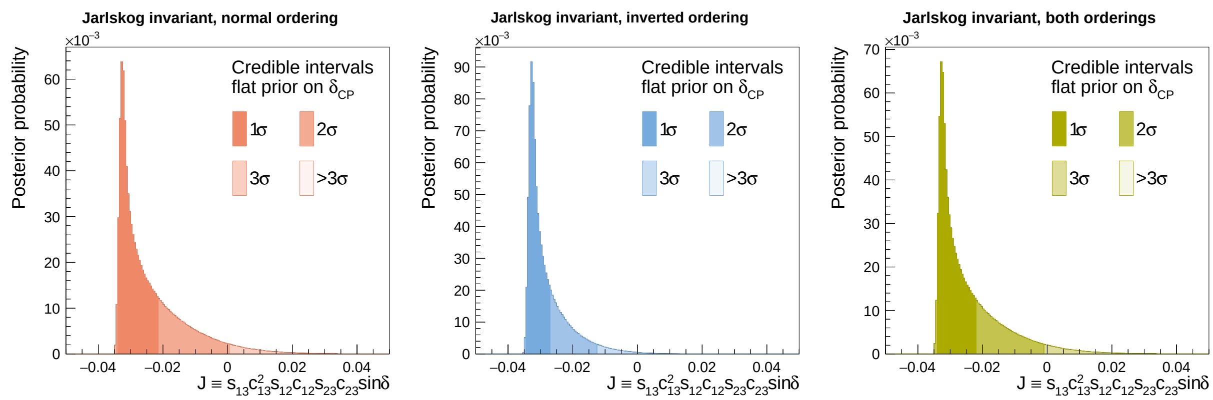

Figure 6: J for the Asimov A analysis, with the reactor constraint applied, for normal (left), inverted (center), and both (right) orderings, with a flat prior on $\delta_{\rm CP}$.

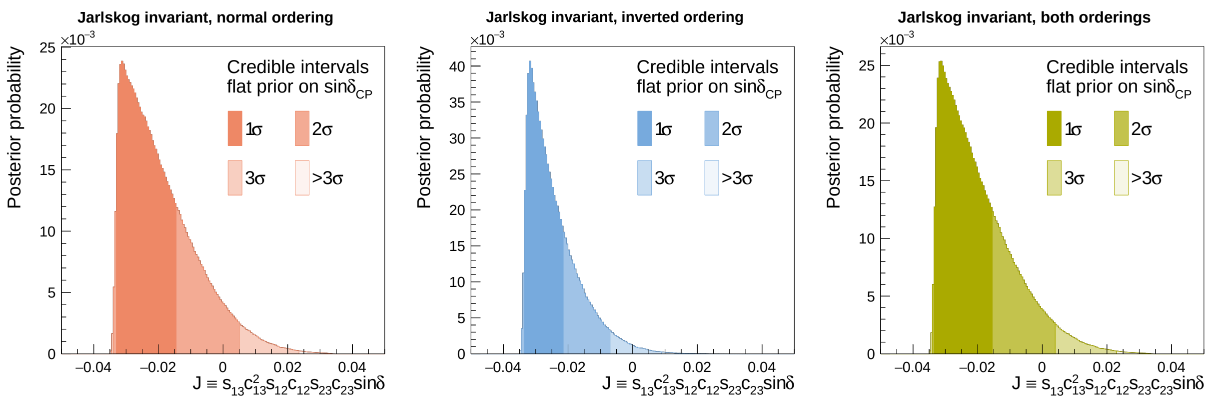

Figure 7: J for the Asimov A analysis, with the reactor constraint applied, for normal (left), inverted (center), and both (right) orderings, with flat prior on $\sin\delta_{\rm CP}$.

Two-dimensional posteriors Fig. 8, Fig. 9, Fig. 10, Fig. 11, Fig. 12, Fig. 13 and Fig. 14 show the two-dimensional marginal posteriors for $\delta_{\text{CP}} - \sin^2\theta_{13}$, $\delta_{\text{CP}} - \sin^2\theta_{23}$, $\delta_{\text{CP}} - \Delta m^2_{32}$, $\Delta m^2_{32} - \sin^2\theta_{13}$, $\Delta m^2_{32} - \sin^2\theta_{23}$, $\sin^2\theta_{13} - \sin^2\theta_{23}$ and $\sin^2\theta_{23} - \Delta m^2_{32}$, respectively. These are shown separately for normal ordering, inverted ordering and both orderings, all applying the reactor constraint.

It is evident that the current MCMC statistics is not sufficient for 3σ credible intervals in 2D with the current binning in the oscillation parameters. No statement is based on the 3σ confidence interval, so computing resources were not allocated to ensure stable 3σ contours.

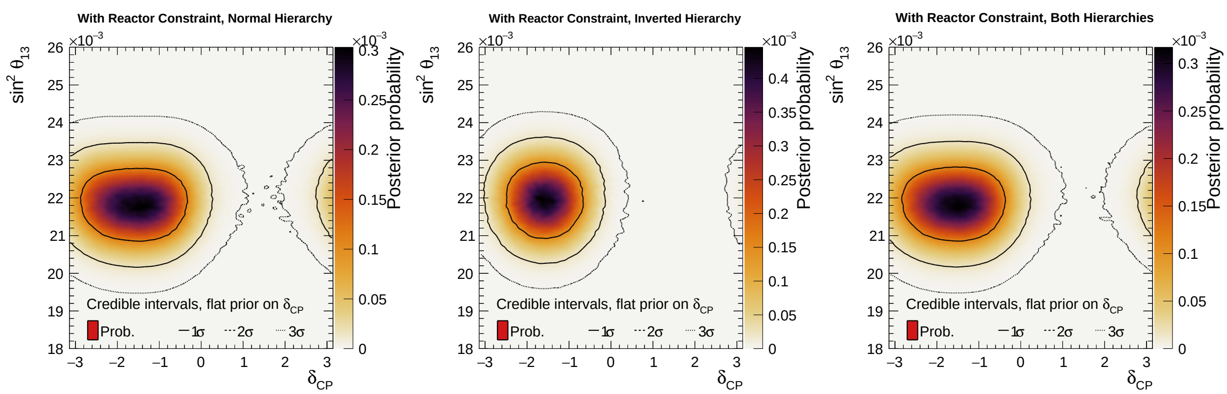

Figure 8: $\delta_{\text{CP}} - \sin^2\theta_{13}$ for the Asimov A analysis, with the reactor constraint applied, for normal (left), inverted (center), and both (right) orderings.

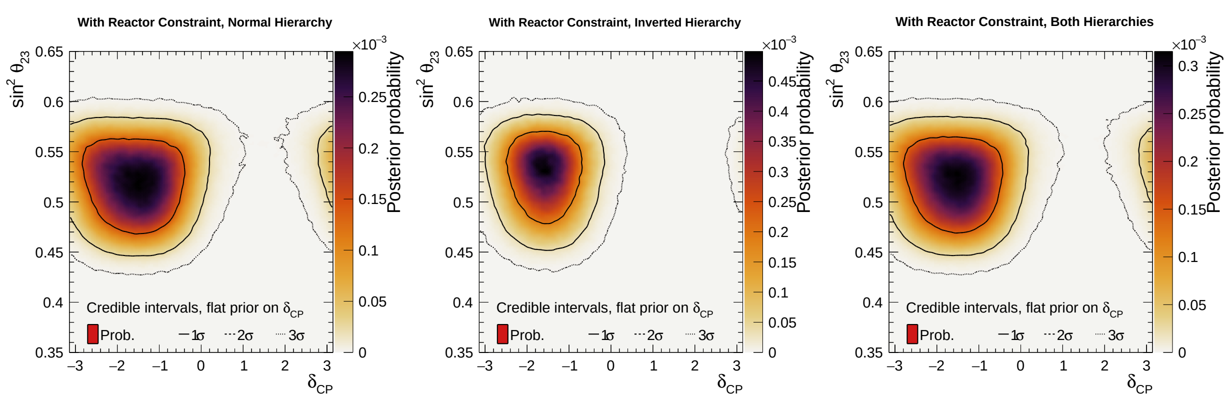

Figure 9: $\delta_{\text{CP}} - \sin^2\theta_{23}$ for the Asimov A analysis, with the reactor constraint applied, for normal (left), inverted (center), and both (right) orderings.

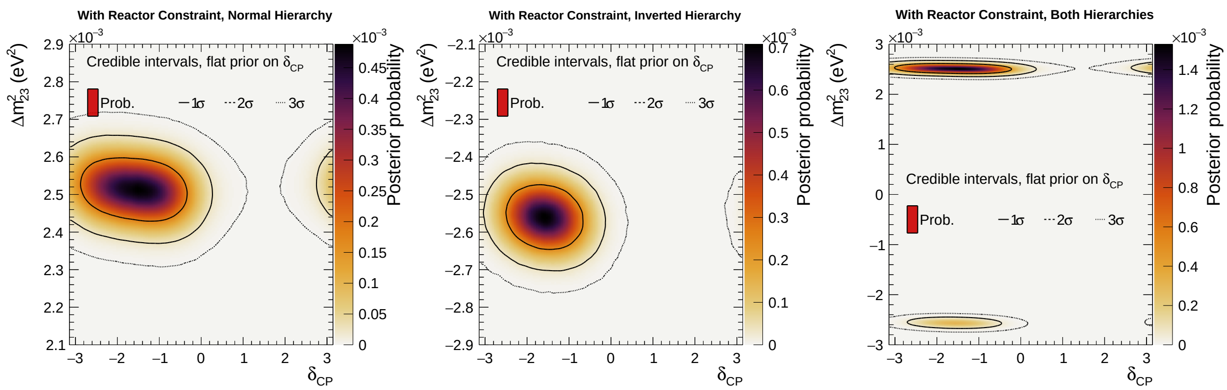

Figure 10: $\delta_{\mathrm{CP}} - \Delta m^2_{32}$ for the Asimov A analysis, with the reactor constraint applied, for normal (left), inverted (center), and both (right) orderings.

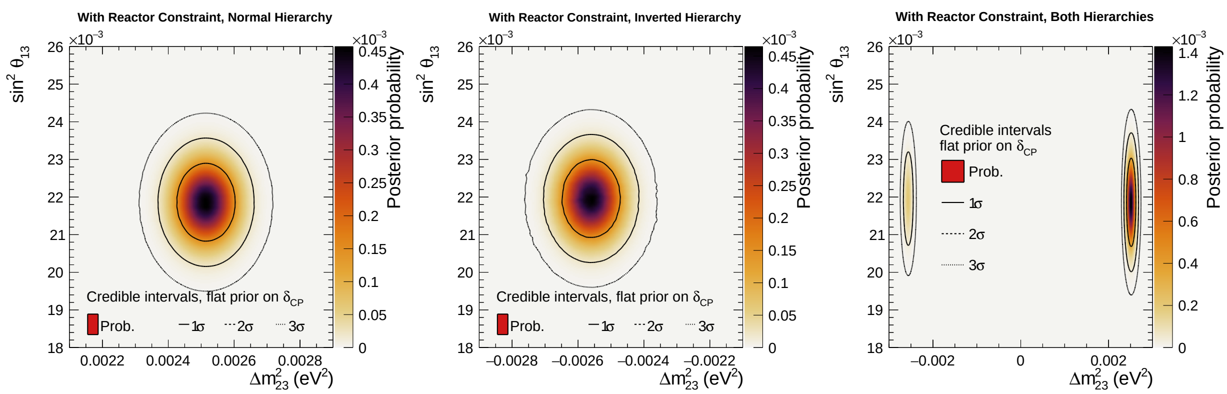

Figure 11: $\Delta m^2_{32} - \sin^2\theta_{13}$ for the Asimov A analysis, with the reactor constraint applied, for normal (left), inverted (center), and both (right) orderings.

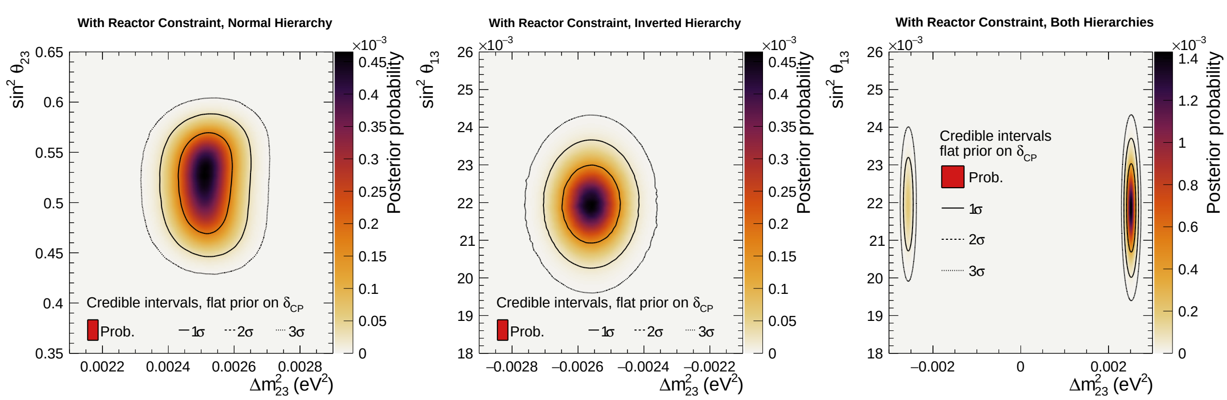

Figure 12: $\Delta m^2_{32} - \sin^2\theta_{23}$ for the Asimov A analysis, with the reactor constraint applied, for normal (left), inverted (center), and both (right) orderings.

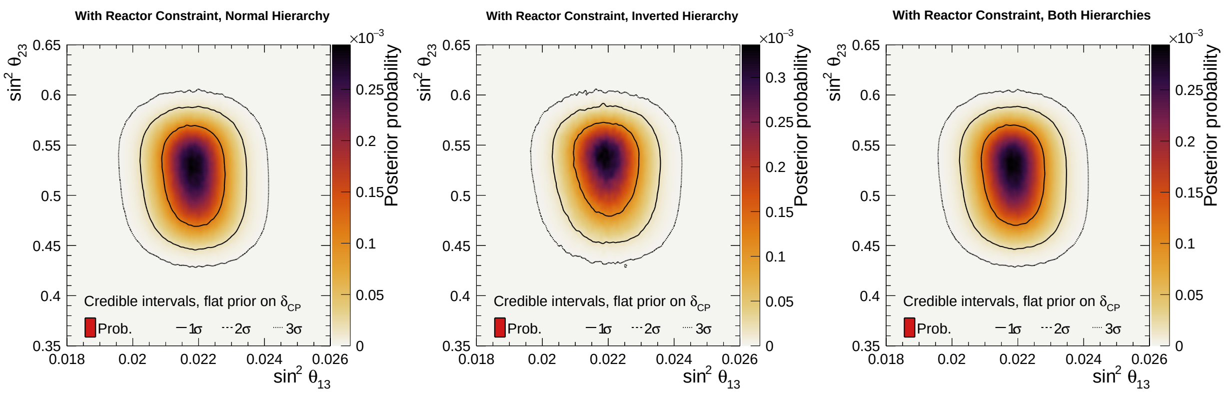

Figure 13: $\sin^2\theta_{13} - \sin^2\theta_{23}$ for the Asimov A analysis, with the reactor constraint applied, for normal (left), inverted (center), and both (right) orderings.

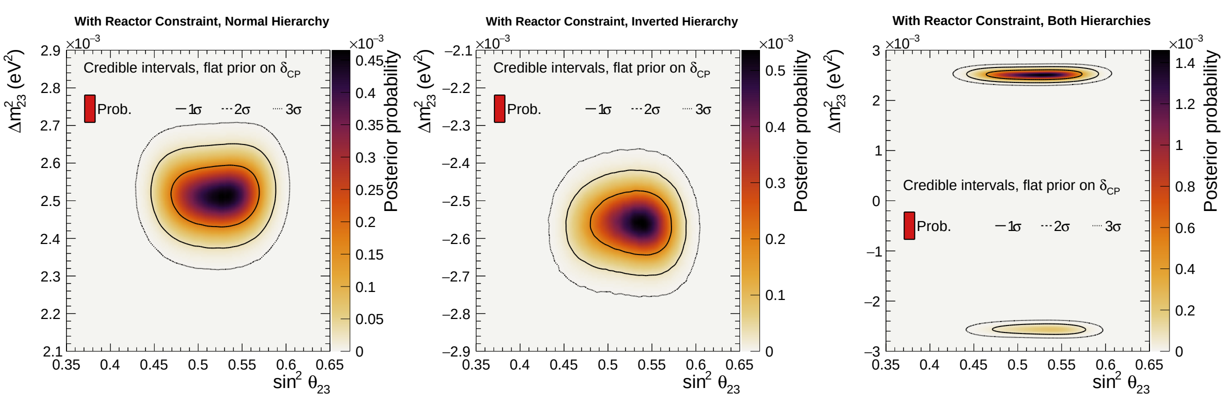

Figure 14: $\sin^2\theta_{23} - \Delta m^2_{32}$ for the Asimov A analysis, with the reactor constraint applied, for normal (left), inverted (center), and both (right) orderings.

The Jarlskog invariant Fig. 15 and Fig. 16 show the two-dimensional $J - \sin^2\theta_{23}$ posteriors for normal ordering, inverted ordering and both orderings, with a flat prior on $\delta_{\rm CP}$ and $\sin\delta_{\rm CP}$ respectively. Fig. 17 shows the two-dimensional $J - \delta_{\rm CP}$ posteriors for the orderings, with a flat prior on $\delta_{\rm CP}$.

As expected from the one-dimensional result in Fig. 6 and Fig. 7, the flat prior on $\sin\delta_{\rm CP}$ results in a weaker constraint at 1σ credible interval. However, at 2σ level the two are very similar, and at 3σ level the result with a flat prior on $\sin\delta_{\rm CP}$ is slightly narrower than that with a flat prior on $\delta_{\rm CP}$. The correlation between J and $\sin^2\theta_{23}$ remains similar to that seen in T2K's analyses.

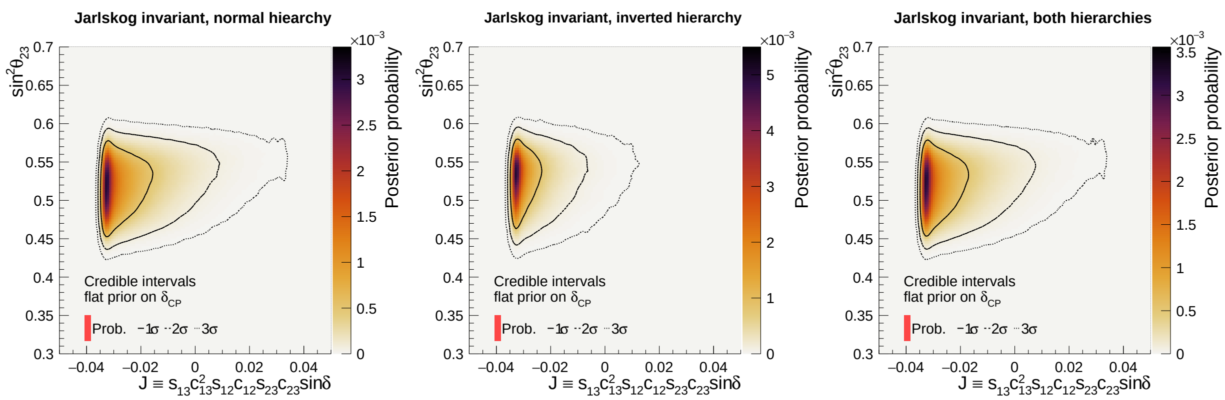

Figure 15: $J - \sin^2\theta_{23}$ for the Asimov A analysis, with the reactor constraint applied, for normal (left), inverted (center), and both (right) orderings, with a flat prior on $\delta_{\rm CP}$.

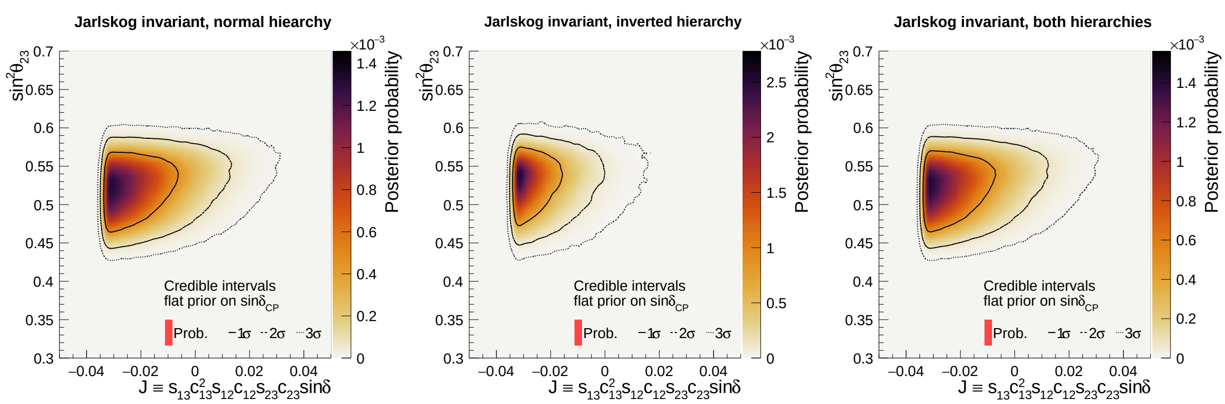

Figure 16: $J - \sin^2\theta_{23}$ for the Asimov A analysis, with the reactor constraint applied, for normal (left), inverted (center), and both (right) orderings, with a flat prior on $\sin\delta_{\rm CP}$.

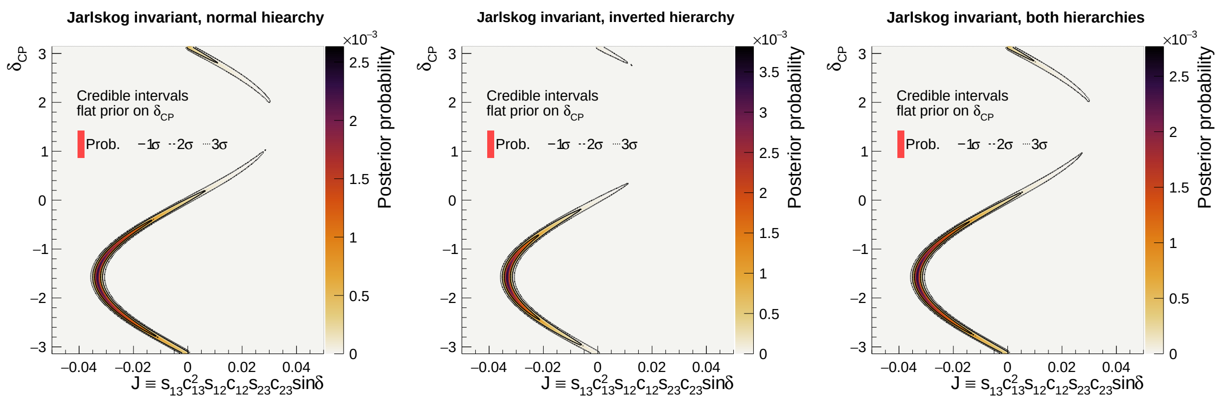

Figure 17: $J - \delta_{\rm CP}$ for the Asimov A analysis, with the reactor constraint applied, for normal (left), inverted (center), and both (right) orderings, with a flat prior on $\delta_{\rm CP}$.

3.1.2 Triangle plots

Fig. 18, Fig. 19, and Fig. 20 show the one and two-dimensional oscillation parameters' posteriors, displayed in triangular form. These all apply the reactor constraint and use a flat prior on δ_{CP}.

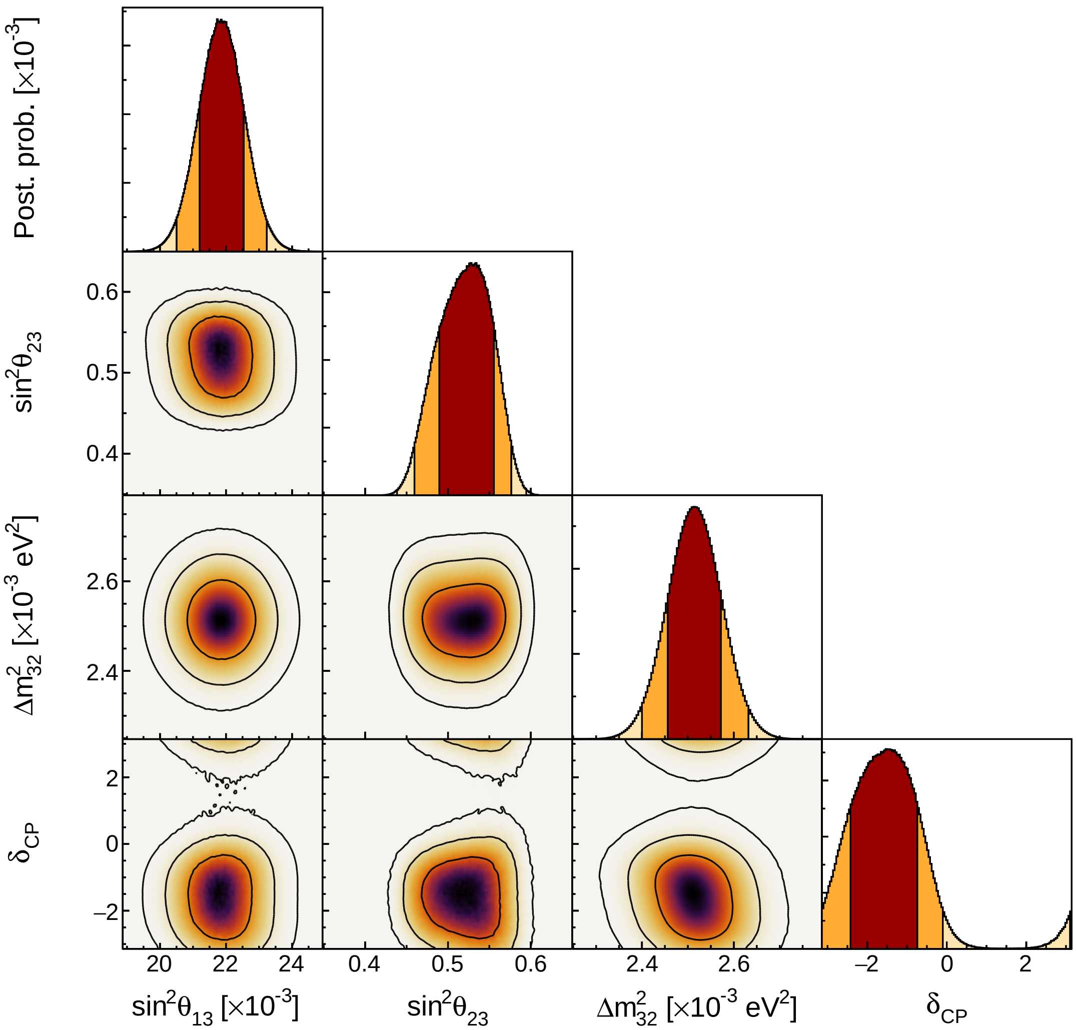

Figure 18: Triangle plots for the Asimov A analysis, with the reactor constraint applied, for the normal ordering, with a flat prior on δ_{CP}. The 1, 2, and 3σ credible intervals are overlaid on the posterior.

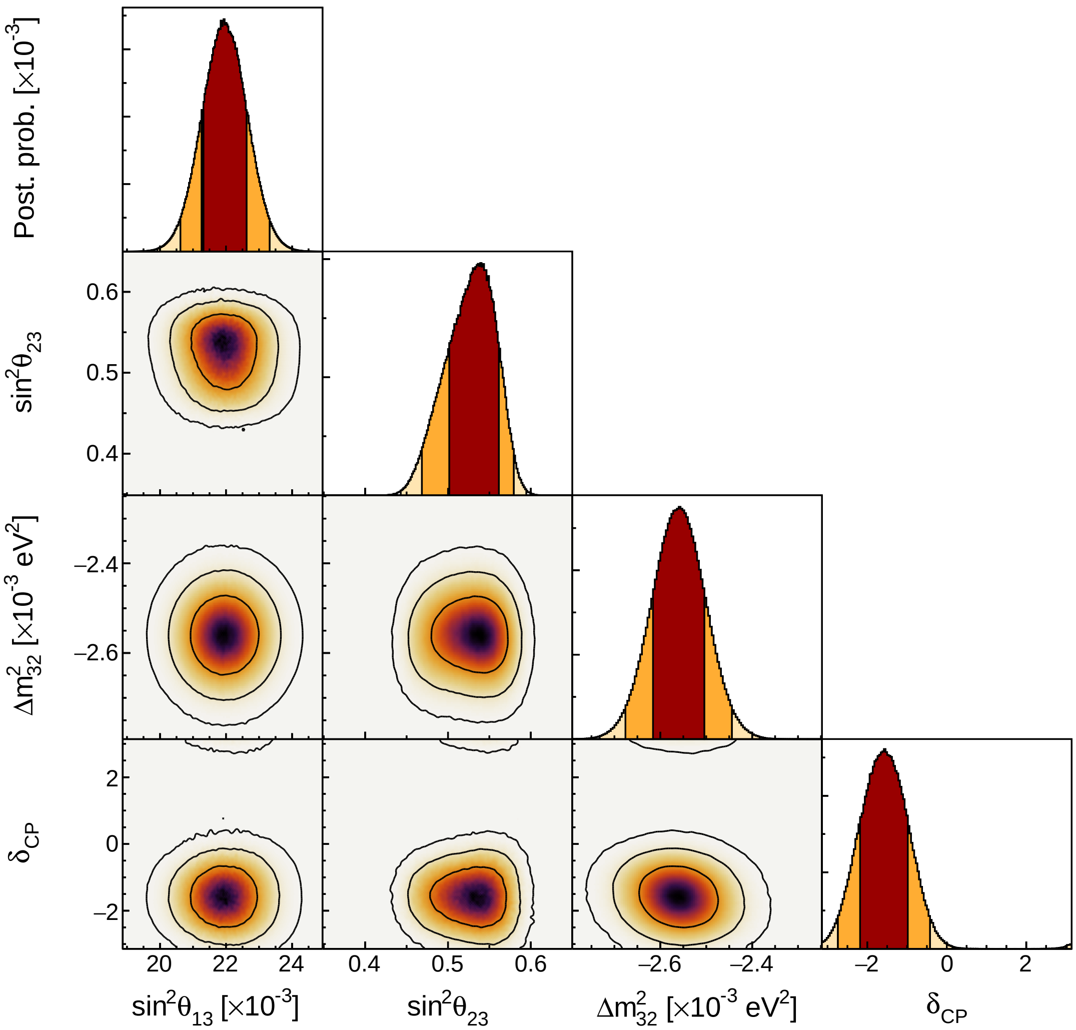

Figure 19: Triangle plots for the Asimov A analysis, with the reactor constraint applied, for the inverted ordering, with a flat prior on δ_{CP}. The 1, 2, and 3σ credible intervals are overlaid on the posterior.

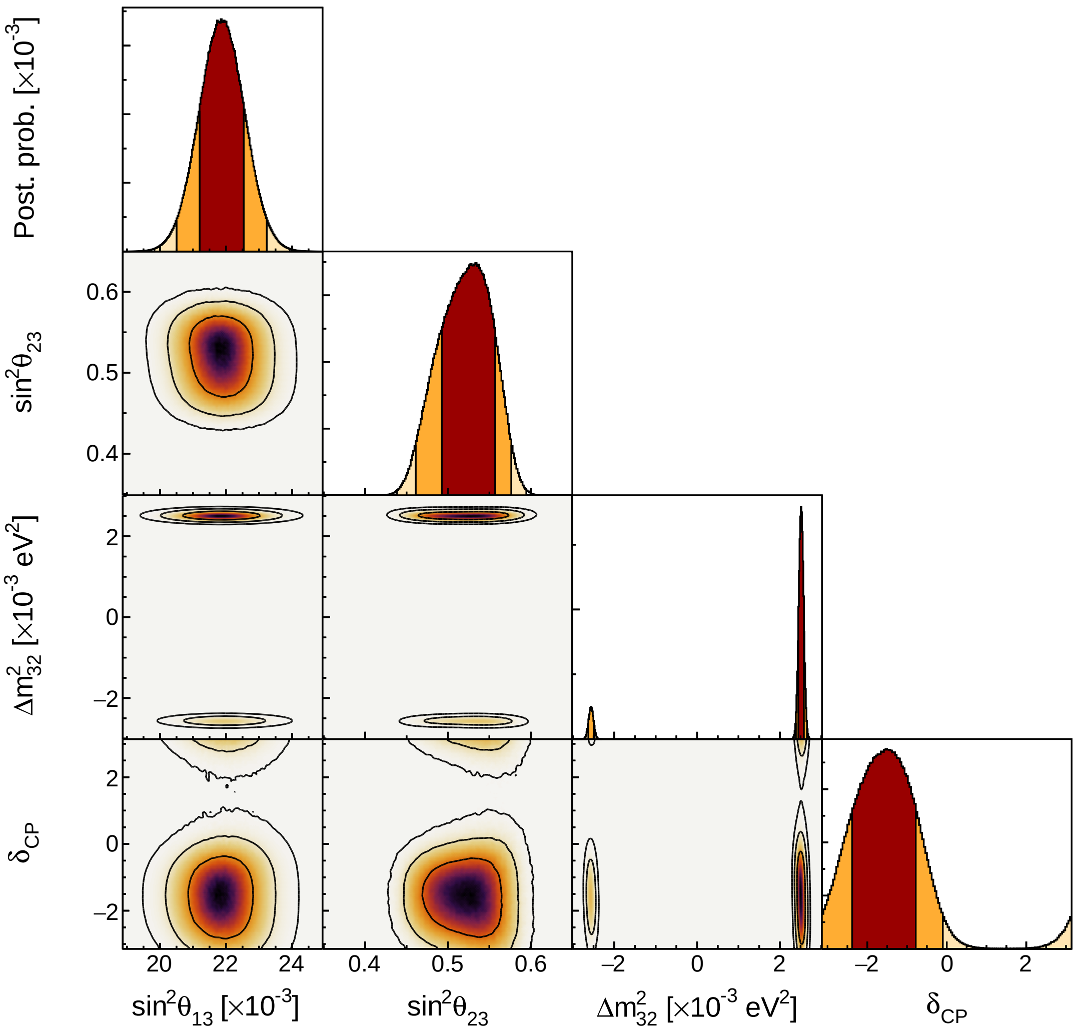

Figure 20: Triangle plots for the Asimov A analysis, with the reactor constraint applied, for both mass orderings, with a flat prior on $\delta_{\rm CP}$. The 1, 2, and 3σ credible intervals are overlaid on the posterior.

3.1.3 Bayes factors for atmospheric parameters

The posterior probabilities of the Asimov A analysis with applying the reactor constraint are summarized in Tab. 2. The Bayes factor of upper octant over lower octant $B(\mathrm{UO/LO}) = 2.72$, and the Bayes factor of normal ordering over inverted ordering $B(\mathrm{NO/IO}) = 7.26$. The Bayes factor for the combination of upper octant and normal ordering is $B([\mathrm{UO{+}NO}]/\mathrm{Other}) = 1.73$.

	$\sin^2\theta_{23} < 0.5$	$\sin^2\theta_{23} > 0.5$	Sum
NO ($\Delta m^2_{32} > 0$)	0.25	0.63	0.88
IO ($\Delta m^2_{32} < 0$)	0.02	0.10	0.12
Sum	0.27	0.73	1.00

Table 2: Posterior probabilities for the mass ordering and the octant in the Asimov A analysis, with the reactor constraint applied.

3.2 Results without applying the reactor constraint

This section shows the Asimov A analysis without applying the reactor constraint on $\sin^2\theta_{13}$. The same Asimov A chains are used with a burn-in period of 80,000 steps per independent chain.

3.2.1 Parameter constraints

Each parameter constraint in this section is shown in normal ordering ($\Delta m^2_{32} > 0$), inverted ordering ($\Delta m^2_{32} < 0$), and over both orderings.

One-dimensional posteriors Fig. 21, Fig. 22, Fig. 23 and Fig. 24 show the marginalised one-dimensional posterior for δ_{CP}, Δm^2_{32}, $\sin^2\theta_{13}$ and $\sin^2\theta_{23}$, respectively.

For the δ_{CP} result, a small region around $\delta_{\mathrm{CP}} \sim \pi/2$ is excluded at 3σ confidence level.

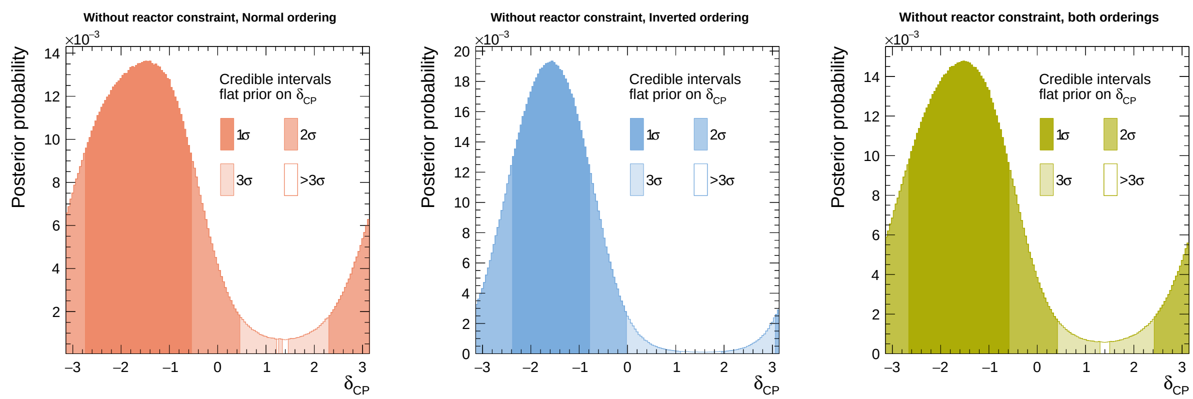

Figure 21: δ_{CP} for the Asimov A analysis, without the reactor constraint applied, for normal (left), inverted (center), and both (right) orderings.

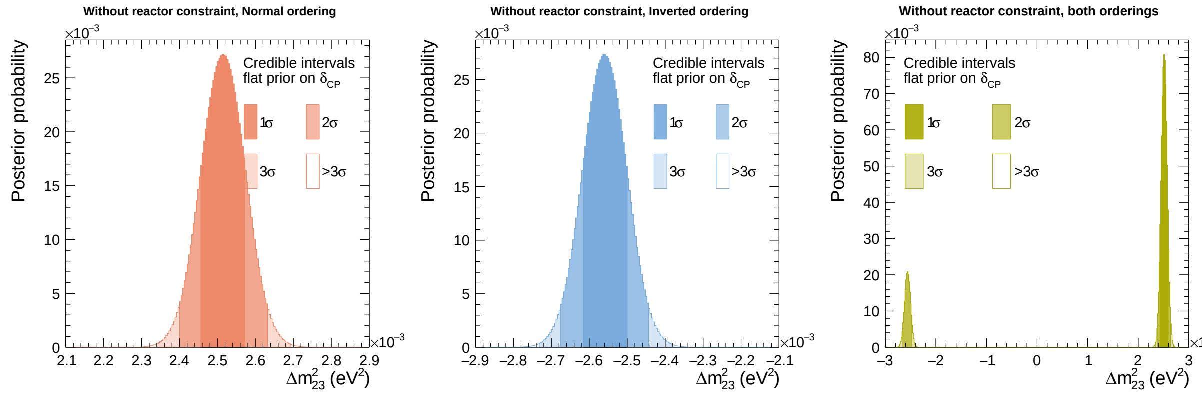

Figure 22: Δm^2_{32} for the Asimov A analysis, without the reactor constraint applied, for normal (left), inverted (center), and both (right) orderings.

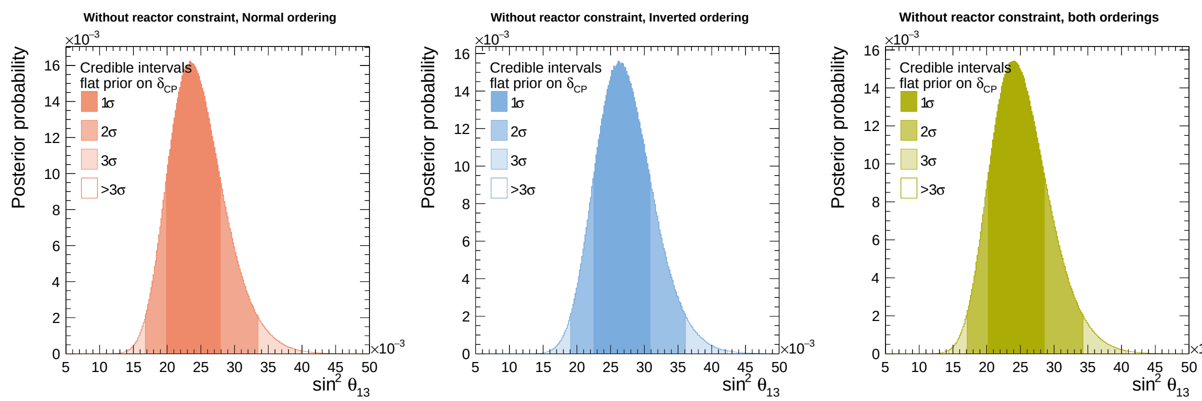

Figure 23: $\sin^2\theta_{13}$ for the Asimov A analysis, without the reactor constraint applied, for normal (left), inverted (center), and both (right) orderings.

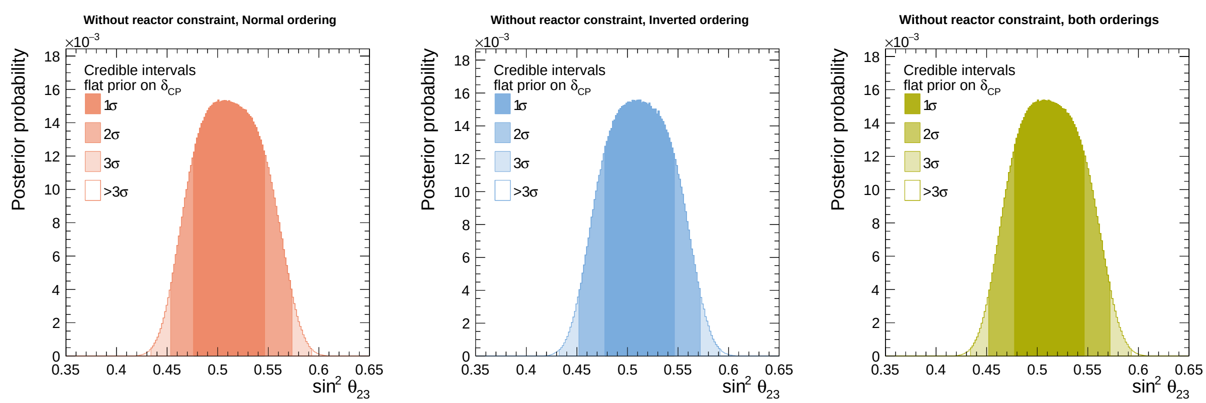

Figure 24: $\sin^2\theta_{23}$ for the Asimov A analysis, without the reactor constraint applied, for normal (left), inverted (center), and both (right) orderings.

The Jarlskog invariant Fig. 25 and Fig. 26 show the marginalised one-dimensional Jarlskog invariant posteriors with flat prior on δ_{CP} and $\sin\delta_{\mathrm{CP}}$ respectively. They are shown without reactor constraint for normal, inverted and both mass orderings. The positive J solution $J \sim 0.04$ is visible in the normal ordering and when marginalising over both orderings, with a weakly bimodal posterior, and the strongest excluded region is between $J = [0.02, 0.035]$.

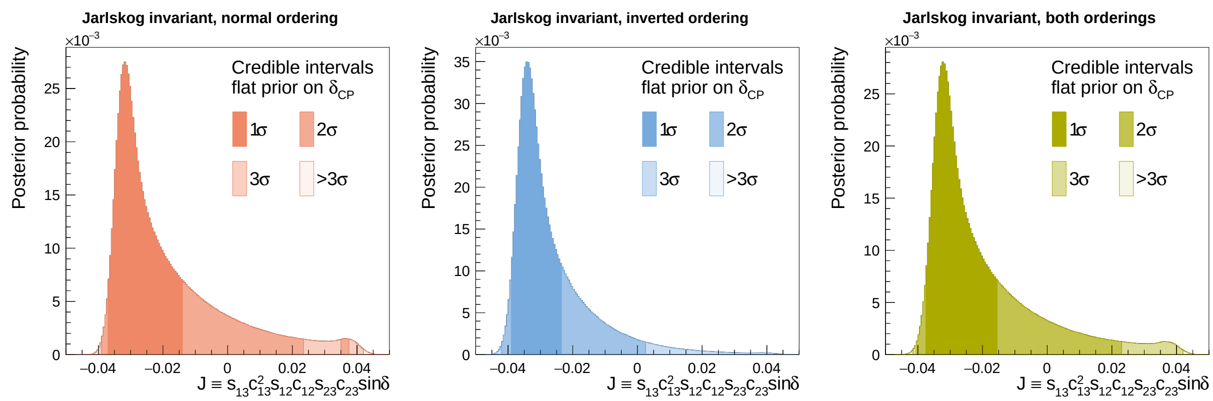

Figure 25: J for the Asimov A analysis, without the reactor constraint applied, for normal (left), inverted (center), and both (right) orderings, with a flat prior on δ_{CP}.

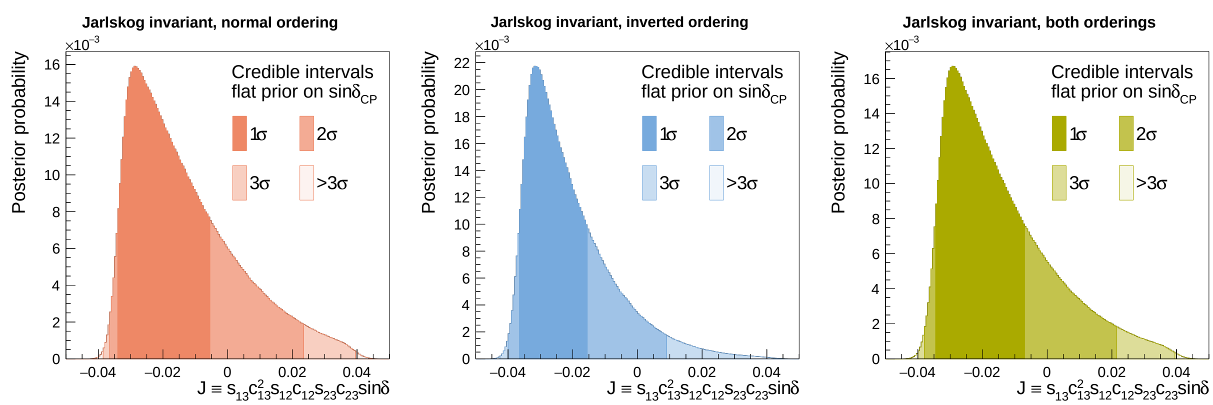

Figure 26: J for the Asimov A analysis, without the reactor constraint applied, for normal (left), inverted (center), and both (right) orderings, with a flat prior on $\sin\delta_{\mathrm{CP}}$.

Two-dimensional posteriors Fig. 27, Fig. 28, Fig. 29, Fig. 30, Fig. 31, Fig. 32 and Fig. 33 show the two-dimensional marginal posteriors for $\delta_{\rm CP} - \sin^2\theta_{13}$, $\delta_{\rm CP} - \sin^2\theta_{23}$, $\delta_{\rm CP} - \Delta m^2_{32}$, $\Delta m^2_{32} - \sin^2\theta_{13}$, $\Delta m^2_{32} - \sin^2\theta_{23}$, $\sin^2\theta_{13} - \sin^2\theta_{23}$ and $\sin^2\theta_{23} - \Delta m^2_{32}$, respectively. These are shown separately for normal ordering, inverted ordering and both orderings, all applying the reactor constraint.

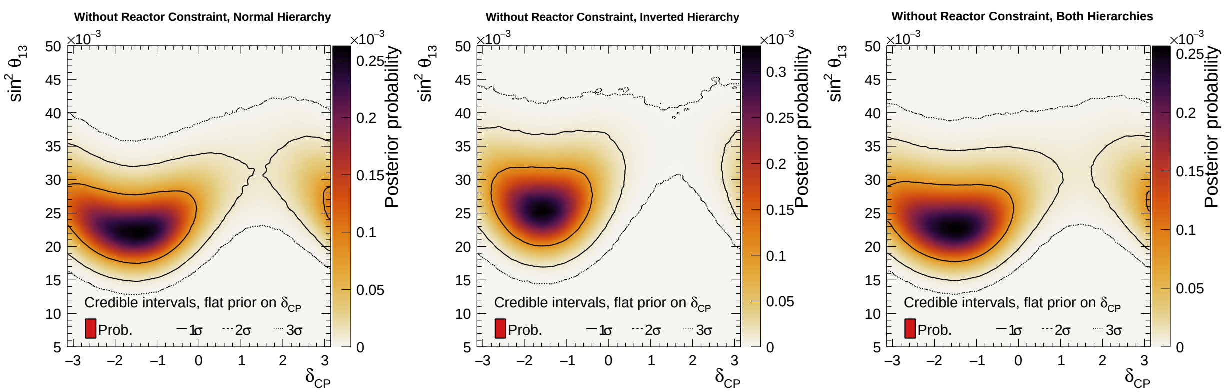

Figure 27: $\delta_{\rm CP} - \sin^2\theta_{13}$ for the Asimov A analysis, without the reactor constraint applied, for normal (left), inverted (center), and both (right) orderings.

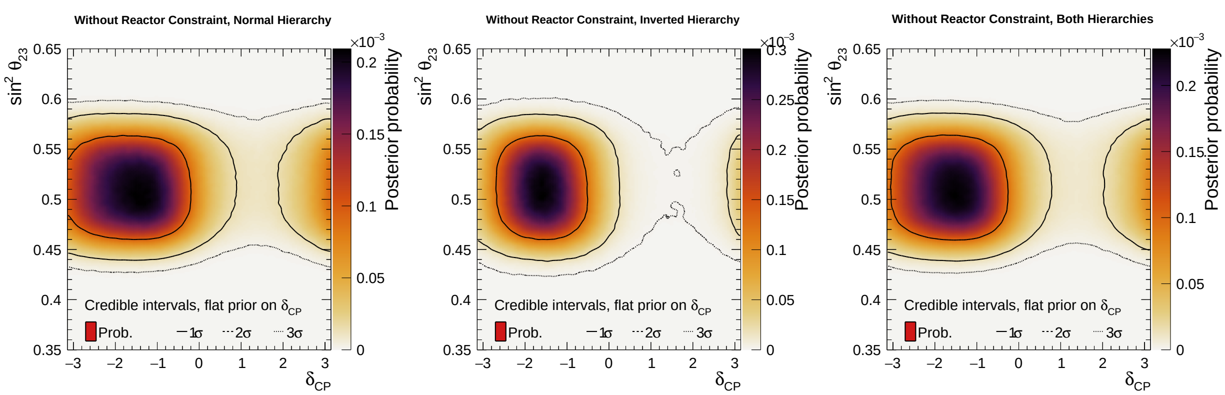

Figure 28: $\delta_{\rm CP} - \sin^2\theta_{23}$ for the Asimov A analysis, without the reactor constraint applied, for normal (left), inverted (center), and both (right) orderings.

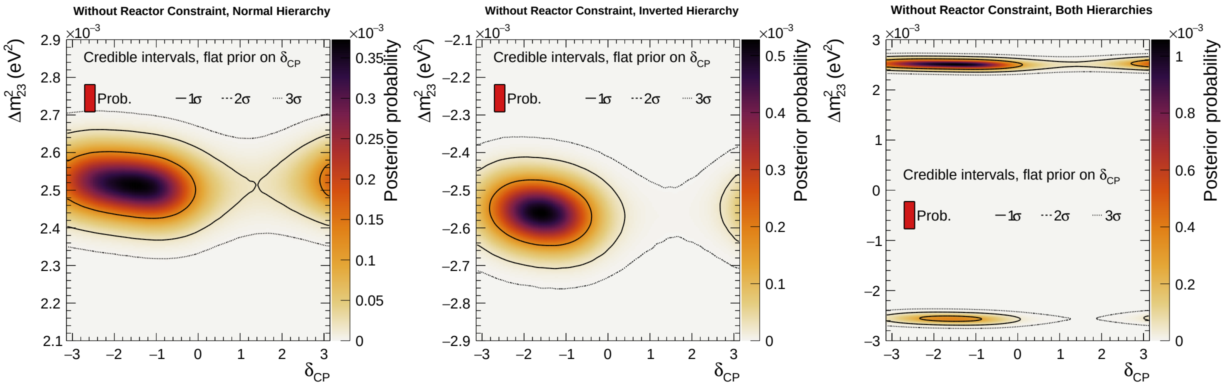

Figure 29: $\delta_{\rm CP} - \Delta m^2_{32}$ for the Asimov A analysis, without the reactor constraint applied, for normal (left), inverted (center), and both (right) orderings.

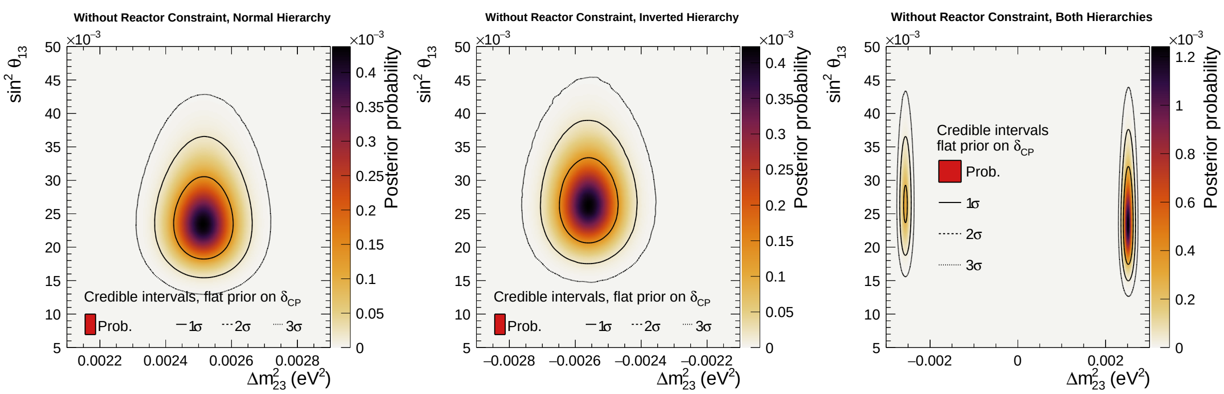

Figure 30: $\Delta m^2_{32} - \sin^2\theta_{13}$ for the Asimov A analysis, without the reactor constraint applied, for normal (left), inverted (center), and both (right) orderings.

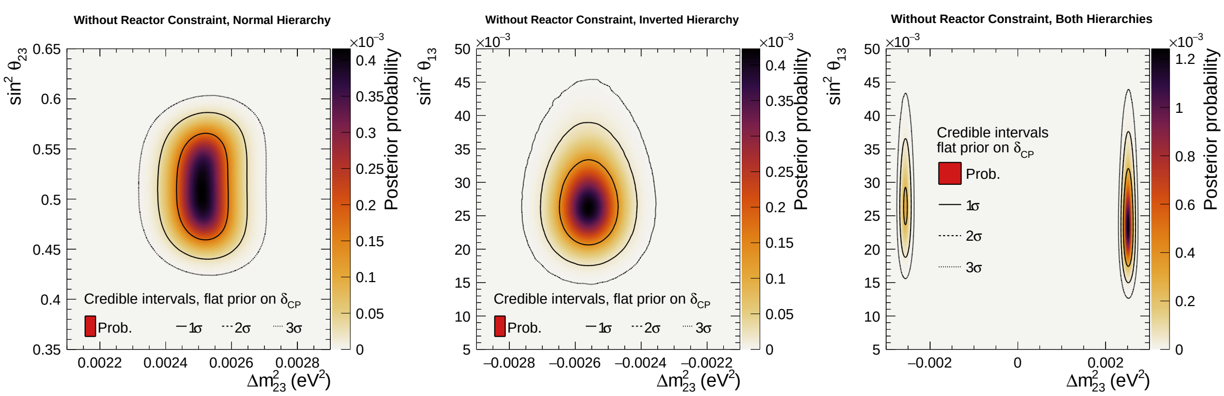

Figure 31: $\Delta m^2_{32} - \sin^2\theta_{23}$ for the Asimov A analysis, without the reactor constraint applied, for normal (left), inverted (center), and both (right) orderings.

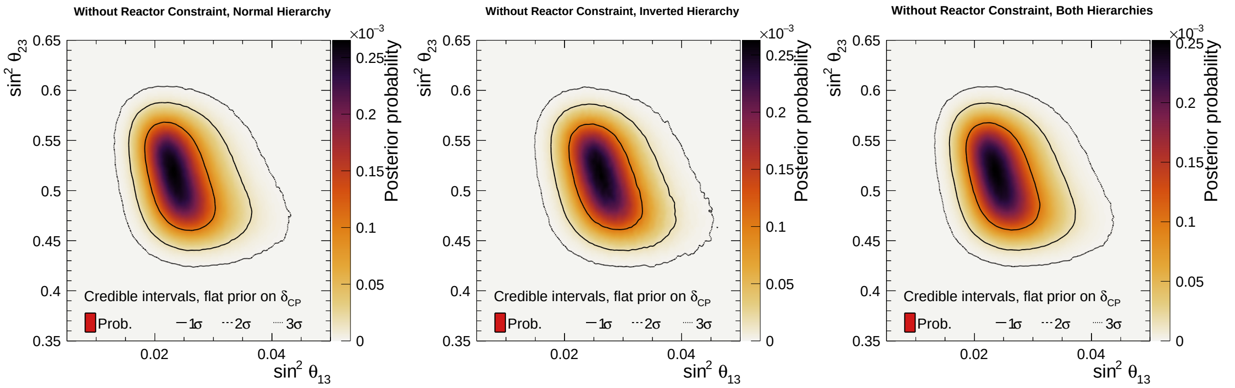

Figure 32: $\sin^2\theta_{13} - \sin^2\theta_{23}$ for the Asimov A analysis, without the reactor constraint applied, for normal (left), inverted (center), and both (right) orderings.

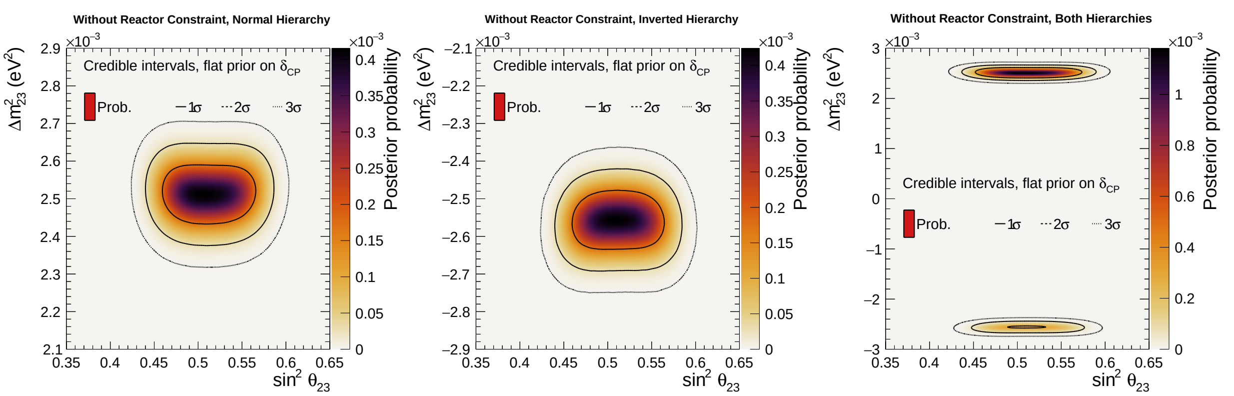

Figure 33: $\sin^2\theta_{23} - \Delta m^2_{32}$ for the Asimov A analysis, without the reactor constraint applied, for normal (left), inverted (center), and both (right) orderings.

The Jarlskog invariant Fig. 34 and Fig. 35 show the two-dimensional $J - \sin^2\theta_{23}$ posteriors for normal ordering, inverted ordering and both orderings, with a flat prior on $\delta_{\rm CP}$ and $\sin\delta_{\rm CP}$ respectively. Fig. 36 shows the two-dimensional $J - \delta_{\rm CP}$ posteriors without reactor constraint for the orderings, with a flat prior on $\delta_{\rm CP}$. As with the one-dimensional case, the $J \sim 0.04$ solution is evident for the result with a flat prior on $\delta_{\rm CP}$, and the posterior is relatively flat in $\sin^2\theta_{23}$ in this region. Interestingly, the $J = 0.04$ is not present for the posterior with a flat prior on $\sin\delta_{\rm CP}$.

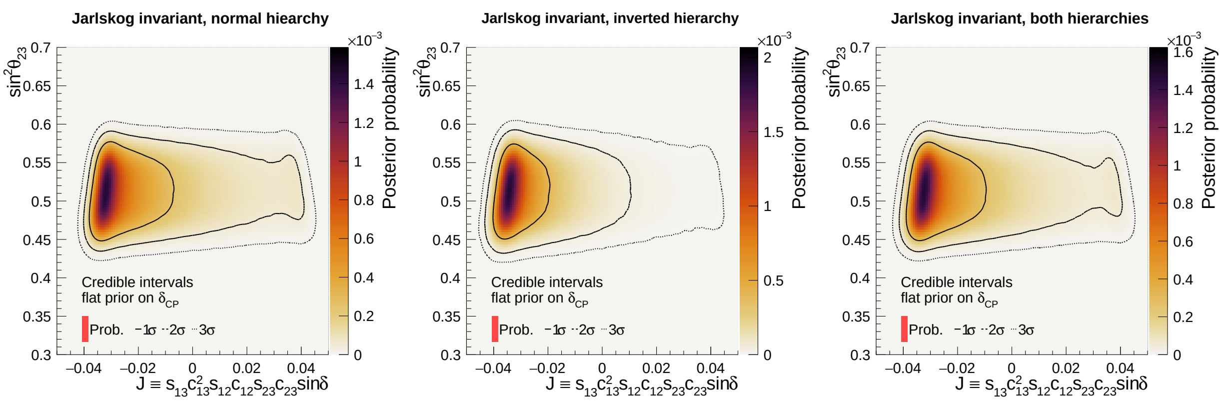

Figure 34: $J - \sin^2\theta_{23}$ for the Asimov A analysis, without the reactor constraint applied, for normal (left), inverted (center), and both (right) orderings, with a flat prior on $\delta_{\rm CP}$.

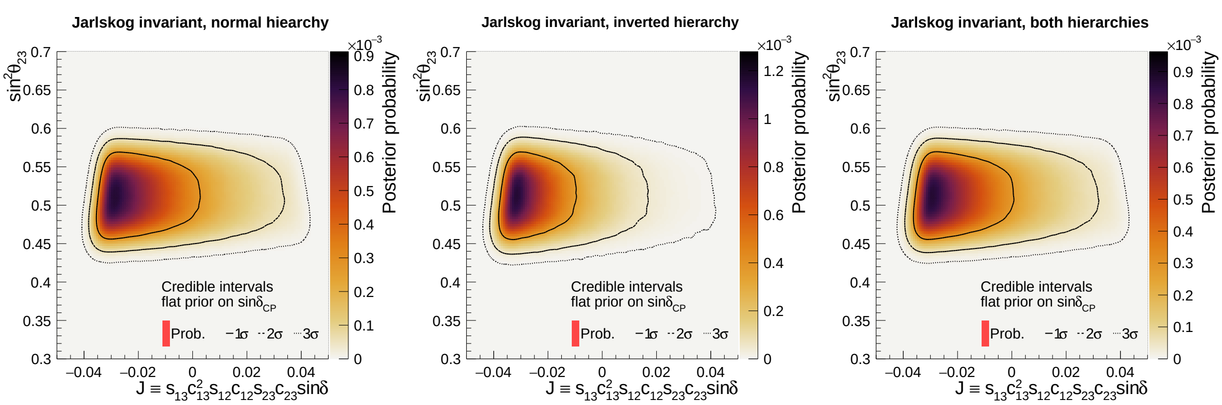

Figure 35: $J - \sin^2\theta_{23}$ for the Asimov A analysis, without the reactor constraint applied, for normal (left), inverted (center), and both (right) orderings, with a flat prior on $\sin\delta_{\rm CP}$.

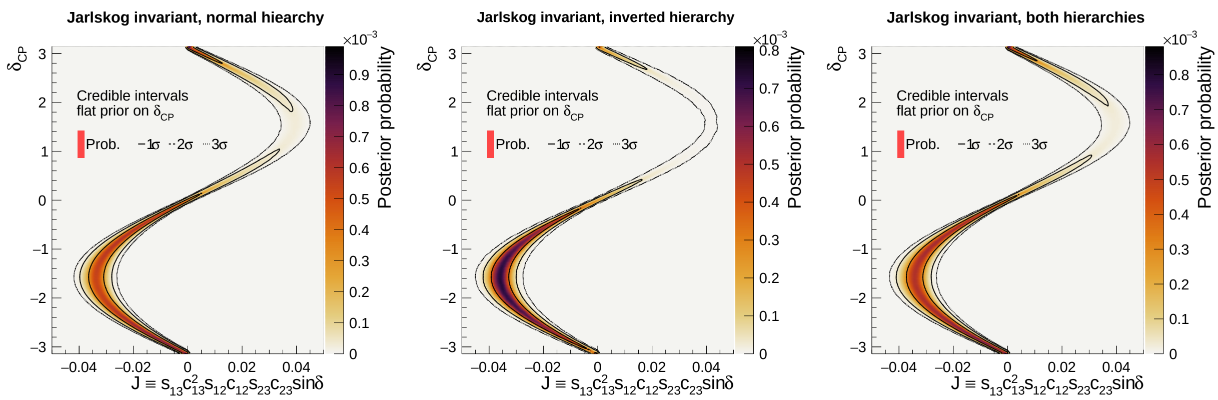

Figure 36: $J - \delta_{\mathrm{CP}}$ for the Asimov A analysis, without the reactor constraint applied, for normal (left), inverted (center), and both (right) orderings, with a flat prior on δ_{CP}.

3.2.2 Triangle plots

Fig. 37, Fig. 38, and Fig. 39 show the one and two-dimensional oscillation parameters' posteriors, displayed in triangular form. These do not apply the reactor constraint, and use a flat prior on δ_{CP}.

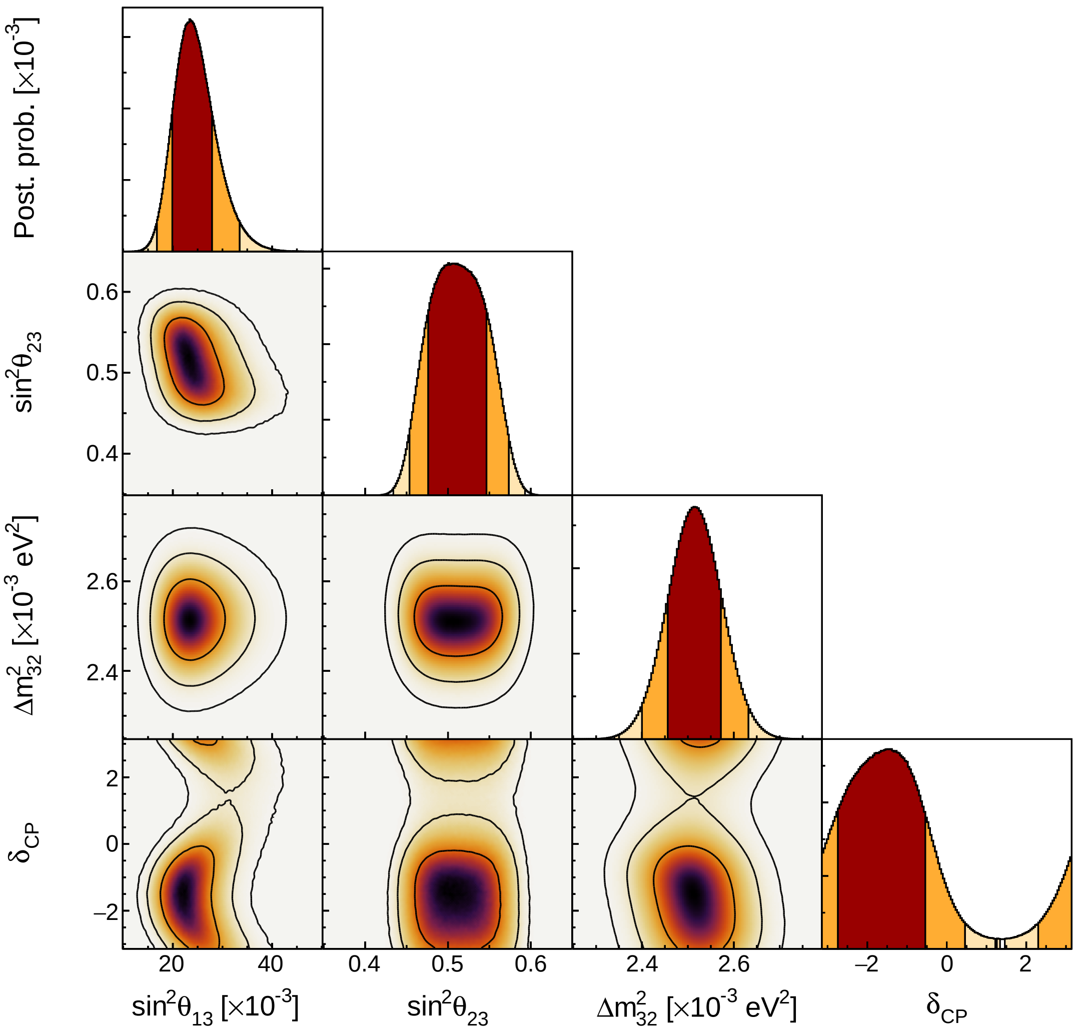

Figure 37: Triangle plots for the Asimov A analysis, without the reactor constraint applied, for the normal ordering, with a flat prior on δ_{CP}. The 1, 2, and 3σ credible intervals are overlaid on the posterior.

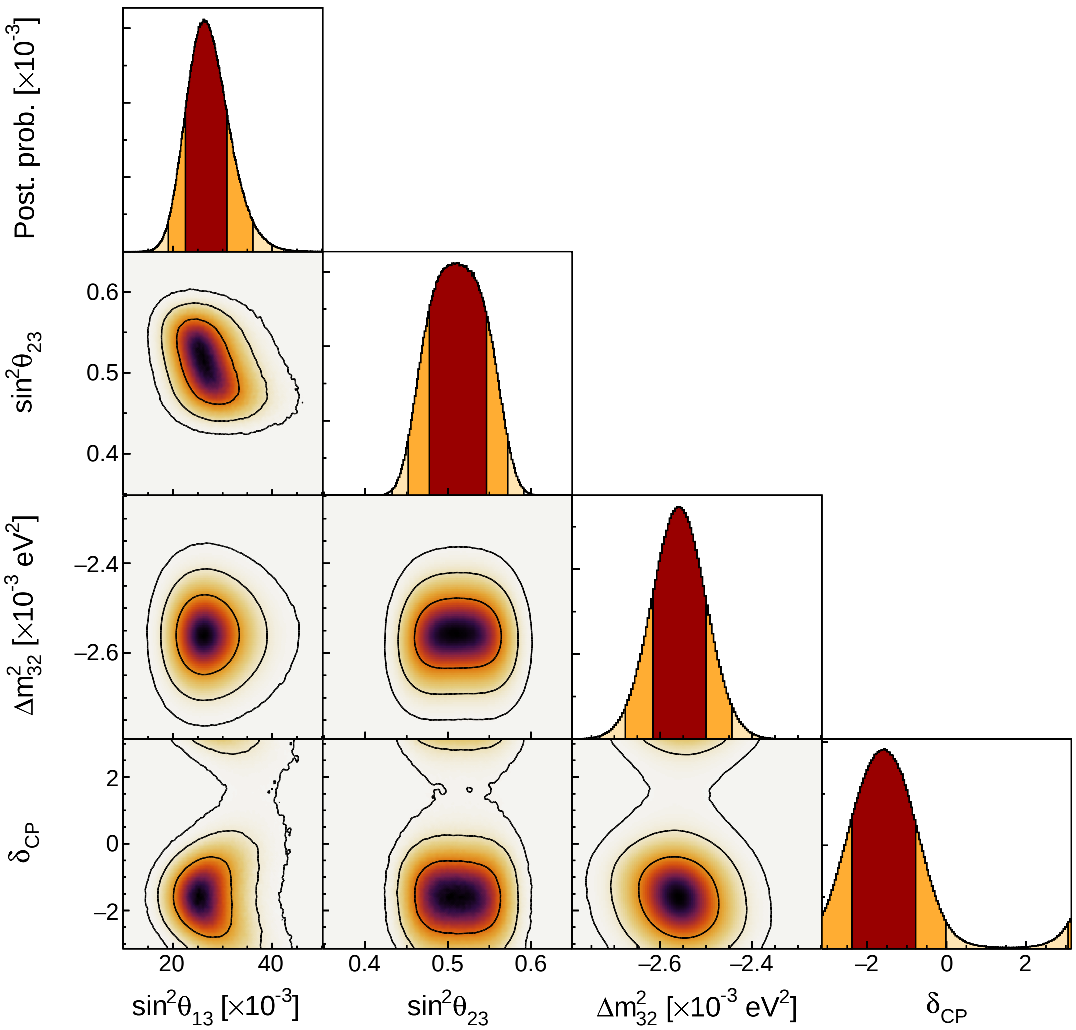

Figure 38: Triangle plots for the Asimov A analysis, without the reactor constraint applied, for the inverted ordering, with a flat prior on δ_{CP}. The 1, 2, and 3σ credible intervals are overlaid on the posterior.

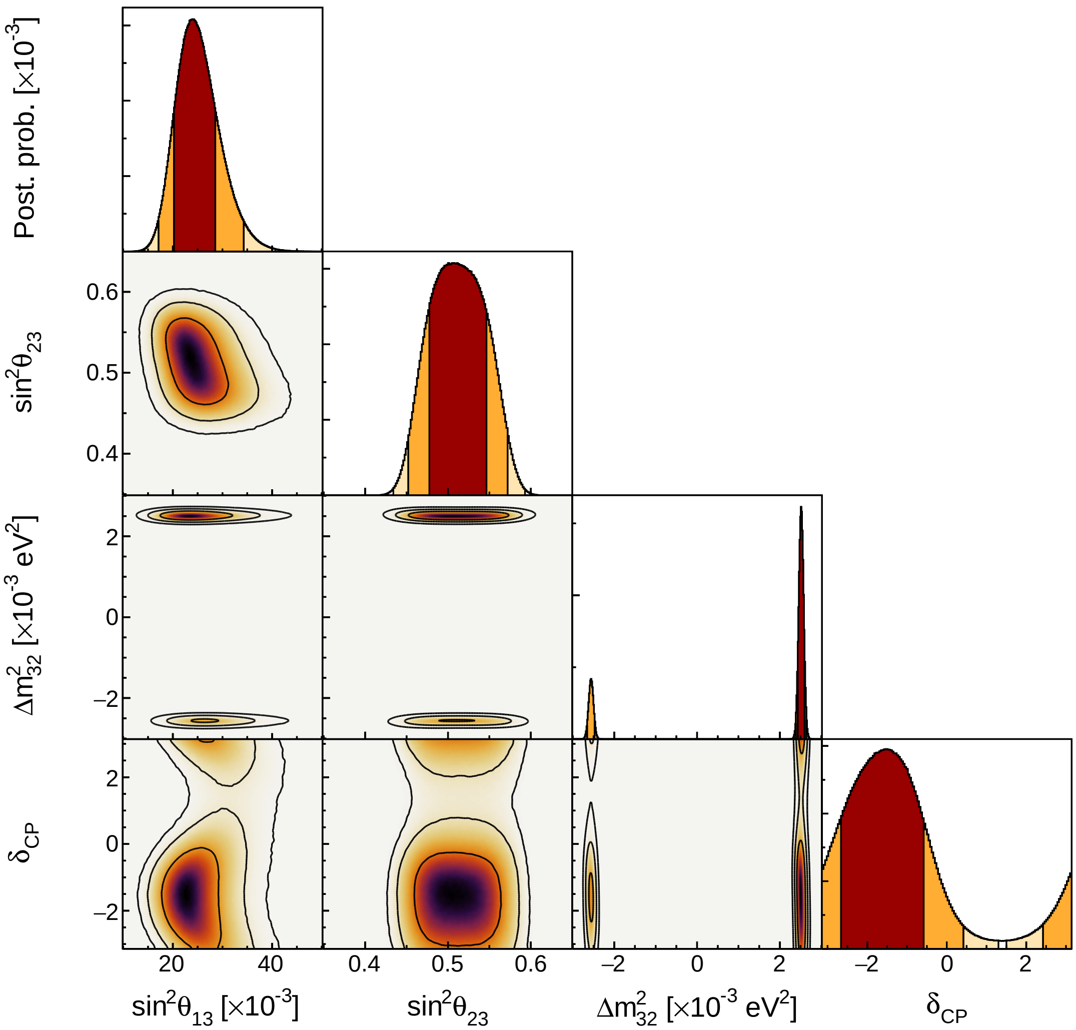

Figure 39: Triangle plots for the Asimov A analysis, without the reactor constraint applied, for both orderings, with a flat prior on $\delta_{\rm CP}$. The 1, 2, and 3σ credible intervals are overlaid on the posterior.

3.2.3 Bayes factors for atmospheric parameters

The posterior probabilities of the Asimov A analysis without applying the reactor constraint are summarized in Tab. 3. The Bayes factor of upper octant over lower octant $B(\mathrm{UO/LO}) = 1.67$, and the Bayes factor of normal ordering over inverted ordering $B(\mathrm{NO/IO}) = 3.98$. The Bayes factor for the combination of upper octant and normal ordering is very weak, with $B([\mathrm{UO{+}NO}]/\mathrm{Other}) = 0.98$.

	$\sin^2\theta_{23} < 0.5$	$\sin^2\theta_{23} > 0.5$	Sum
NO	0.30	0.50	0.80
IO	0.08	0.13	0.20
Sum	0.38	0.62	1.00

Table 3: Posterior probabilities for the mass ordering and the octant in the Asimov A analysis, without the reactor constraint applied.

3.3 Bayes factors for CP violation

Tab. 4 summarises the posterior probabilities of $\sin\delta_{\rm CP} \geq 0$ and $\sin\delta_{\rm CP} < 0$ with and without the reactor constraint. The Bayes factor $B[(\sin\delta_{\rm CP} < 0)/(\sin\delta_{\rm CP} \geq 0)]$ is 24.5(6.3) with(out) the reactor constraint applied.

	$\sin\delta_{\rm CP} \geq 0$	$\sin\delta_{\rm CP} < 0$	Sum
No RC	0.137	0.863	1.000
RC	0.039	0.961	1.000

Table 4: Posterior probabilities for $\sin\delta_{\rm CP}$ in the Asimov A analysis with and without reactor constraint

4 Results from fitting real data

In this section we move from Asimov studies to analysing the real data at all detectors' selections; T2K ND280, T2K SK, and SK atmospheric. After inspecting traces and auto-correlations, the same MCMC configuration is used for the data analysis as with the analysis of Asimov A "data". For the data analysis, part of the steps are collected from ORNL Summit and part are from Alliance Canada. 277,661,111 steps were collected in total, with good acceptance rates ($\sim 15-19\%$) and a burn-in of 80,000 steps, with the number of steps after burn-in being 230,940,527. Similar to the Asimov A analysis, the auto-correlation goal was reaching 0.2 by lag 20,000. The trace of the total negative log likelihood for all independent chains are shown in Fig. 40. Results shown in this section are produced using steps collected after burn-in.

As with the Asimov A analysis, smearing from the fake-data studies TN457 [11] have been added, and are applied by randomly smearing Δm^2_{32} by 3.6×10^{-5} eV^2.

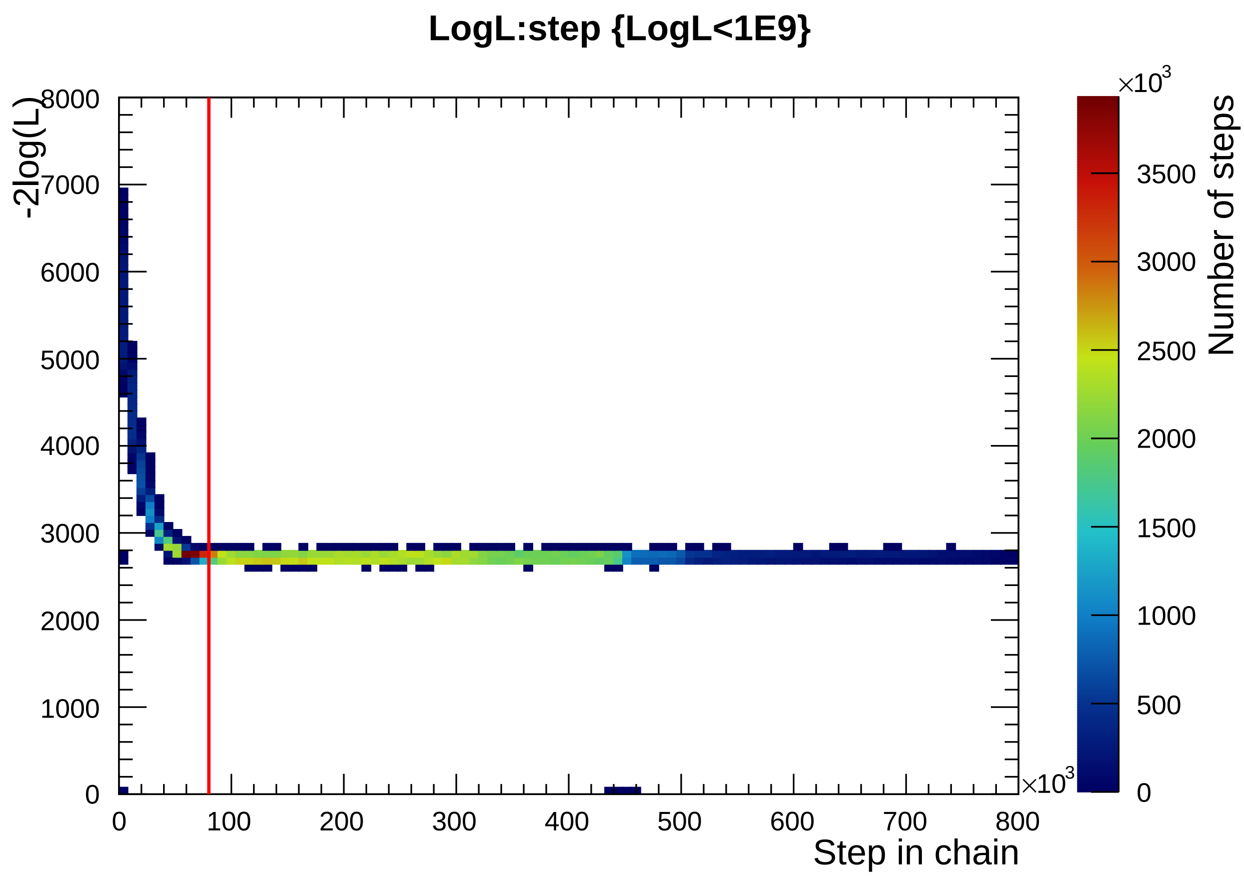

Figure 40: Collection of the traces of the negative log total likelihood from data fit chains. The red line is the cut for post burn-in at 80,000 steps. Note that a few steps post burn-in (step $\sim 450 \times 10^3$) have $-\mathrm{LogL} = 0$ near zero. They appeared after processing the raw chain output files, and were not present in the original files. These steps are excluded in the analysis.

4.1 Results applying the reactor constraint

For these results, the reactor constraint on $\sin^2\theta_{13}$ is used with the same value as the T2K OA2020 analysis TN393 [1] from the PDG [10]; $\sin^2\theta_{13} = 0.0218 \pm 0.0007$.

4.1.1 Parameter constraints, prior flat in δ_{CP}

Each parameter constraint in this section is shown in normal ordering ($\Delta m^2_{32} > 0$), inverted ordering ($\Delta m^2_{32} < 0$), and over bother orderings.

One-dimensional posteriors Fig. 41, Fig. 42, Fig. 43 and Fig. 44 show the marginalised one-dimensional posterior for δ_{CP}, Δm^2_{32}, $\sin^2\theta_{13}$ and $\sin^2\theta_{23}$, respectively.

The δ_{CP} result in Fig. 41 show $\delta_{\mathrm{CP}} = 0$ is excluded at greater than 2σ, and $\sin\delta_{\mathrm{CP}} = 0$ excluded at more than 2σ for all choices of ordering (normal, inverted and both). As further investigated in Tab. 5, after applying the interval shifts from the fake data study (Tab. 4 in TN457 [11]), the 2σ intervals for both normal and inverted ordering exclude $\delta_{\mathrm{CP}} = 0$ with a flat prior on δ_{CP}. However, this is not true for the result on δ_{CP} with a flat prior on $\sin\delta_{\mathrm{CP}}$, presented in Sec. 4.3. The CP violation statements are also studied further with the Jarlskog invariant, including the impact of the prior being flat in δ_{CP} or $\sin\delta_{\mathrm{CP}}$.

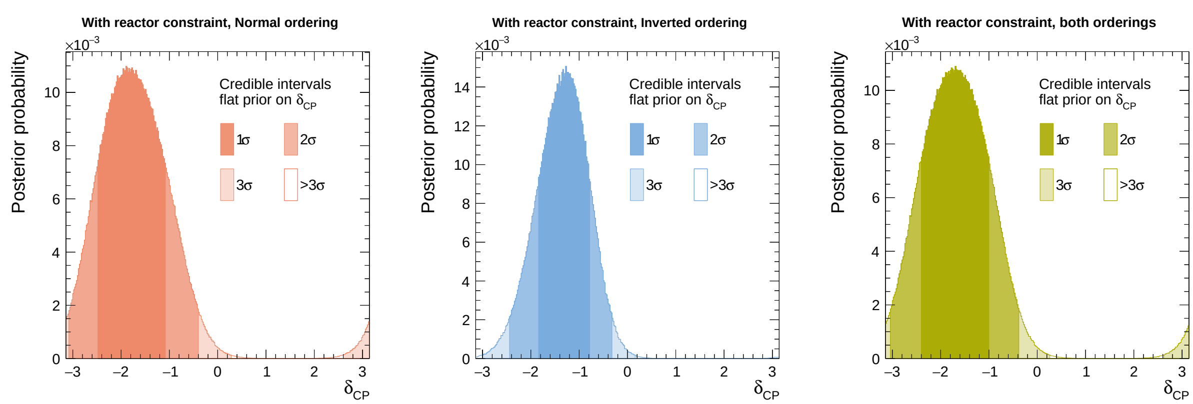

Figure 41: δ_{CP} for the real data analysis, with the reactor constraint applied, for normal (left), inverted (center), and both (right) orderings.

The Δm^2_{32} result in Fig. 42 shows a preference for the normal ordering, with a Bayes factor of 7.33 as calculated in Sec. 4.1.4.

The posterior for $\sin^2\theta_{23}$ in Fig. 44 shows a very weak preference for the upper octant when marginalising over both mass orderings, with the lower octant included in the 1σ credible interval. For the normal ordering, there is almost no octant preference at all. For

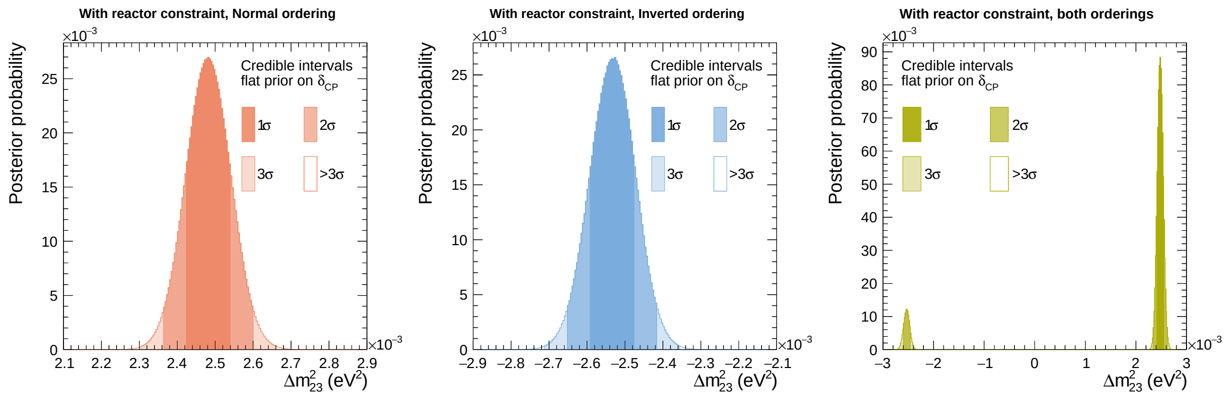

Figure 42: Δm^2_{32} for the real data analysis, with the reactor constraint applied, for normal (left), inverted (center), and both (right) orderings.

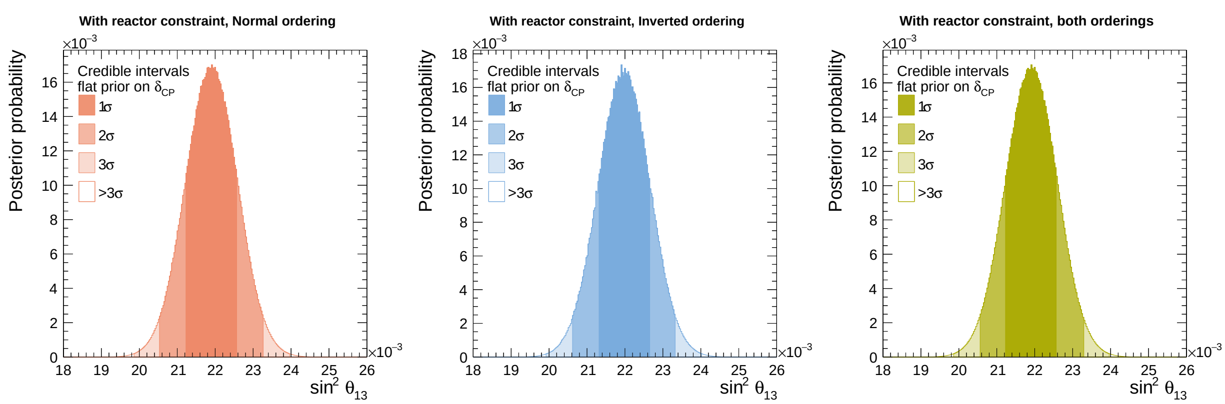

Figure 43: $\sin^2\theta_{13}$ for the real data analysis, with the reactor constraint applied, for normal (left), inverted (center), and both (right) orderings.

the inverted ordering the upper octant is more strongly preferred, although the 1σ credible interval just excludes maximal mixing around $\sin^2\theta_{23} \sim 0.513$. This is confirmed by the Bayes factor studies, which finds $B(UO/LO) = 1.78$ for both orderings, $B(UO/LO)|_{\text{NO}} = 1.63$, and $B(UO/LO)|_{\text{IO}} = 3.33$.

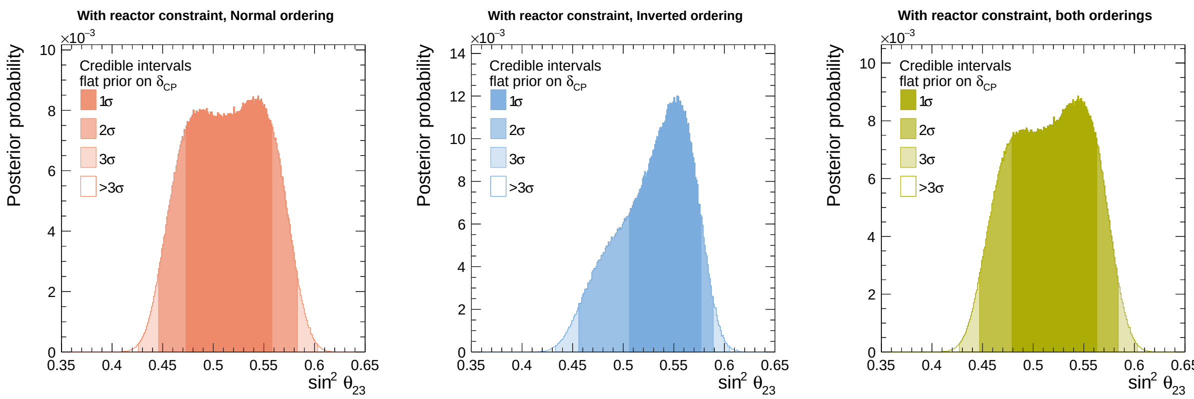

Figure 44: $\sin^2\theta_{23}$ for the real data analysis, with the reactor constraint applied, for normal (left), inverted (center), and both (right) orderings.

Normal Ordering	1sig		2sig		3sig	
	LE	UE	LE	UE	LE	UE
Fit	-2.50127	-1.10056	-3.06155	-0.380193	2.58131	0.260132
Increment	-0.034	0.122	-0.025	0.081	-0.024	0.059
Fit+Increment	-2.53527	-0.97856	-3.08655	-0.299193	2.55731	0.319132
Pass	TRUE		TRUE		FALSE	

Inverted Ordering	1sig		2sig		3sig	
	LE	UE	LE	UE	LE	UE
Fit	-1.82092	-0.780396	-2.42123	-0.300152	-3.02153	0.140071
Increment	-0.034	0.122	-0.025	0.081	-0.024	0.059
Fit+Increment	-1.85492	-0.658396	-2.44623	-0.219152	-3.04553	0.199071
Pass	TRUE		TRUE		FALSE	

Both Ordering	1sig		2sig		3sig	
	LE	UE	LE	UE	LE	UE
Fit	-2.42123	-1.02052	-3.02153	-0.380193	2.62133	0.260132
Increment	-0.034	0.122	-0.025	0.081	-0.024	0.059
Fit+Increment	-2.45523	-0.89852	-3.04653	-0.299193	2.59733	0.319132
Pass	TRUE		TRUE		FALSE	

Table 5: Summary table of δ_{CP} credible interval edges for flat prior of δ_{CP} from the data fit (with reactor constraint) and the edges after applying the shifts from the fake data study TN457 [11] for normal ordering (upper table), inverted ordering (middle table) and both orderings (lower table) respectively. 1σ, 2σ and 3σ intervals are investigated. "Fit" refers to the credible interval edges from MaCh3 data fit results with reactor constraint; "Increment" refers to the extreme shift values from the fake data study results (Table 4 of TN457 v1.3 [11]); "Fit+Increment" refers to the credible interval edges after applying the shift values from fake data studies. The criteria of "Pass" is to check whether the credible interval after applying the shift contains any one of the δ_{CP} values $-\pi, 0, \pi$. "LE" refers to the lower edge of the interval and "UE" refers to the upper edge. Note that "LE" is not necessarily smaller than "UE" because of wrapping through $-\pi = \delta_{\text{CP}} = \pi$.

Normal Ordering	1sig		2sig		3sig	
	LE	UE	LE	UE	LE	UE
Fit	-2.88146	-0.700355	3.02153	-0.180091	2.52128	0.380193
Increment	-0.047	0.168	-0.02	0.086	-0.02	0.054
Fit+Increment	-2.92846	-0.532355	3.00153	-0.094091	2.50128	0.434193
Pass	TRUE		FALSE		FALSE	

Inverted Ordering	1sig		2sig		3sig	
	LE	UE	LE	UE	LE	UE
Fit	-2.08106	-0.400203	-2.66135	-0.140071	-3.14159	0.300152
Increment	-0.047	0.168	-0.02	0.086	-0.02	0.054
Fit+Increment	-2.12806	-0.232203	-2.68135	-0.054071	3.12159	0.354152
Pass	TRUE		TRUE		FALSE	

Both Ordering	1sig		2sig		3sig	
	LE	UE	LE	UE	LE	UE
Fit	-2.82143	-0.660335	3.04154	-0.180091	2.54129	0.380193
Increment	-0.047	0.168	-0.02	0.086	-0.02	0.054
Fit+Increment	-2.86843	-0.492335	3.02154	-0.094091	2.52129	0.434193
Pass	TRUE		FALSE		FALSE	

Table 6: Summary table of $\delta_{\rm CP}$ credible interval edges for flat prior of $\sin\delta_{\rm CP}$ from the data fit (with reactor constraint) and the edges after applying the shifts from the fake data study TN457 [11] for normal ordering (upper table), inverted ordering (middle table) and both orderings (lower table) respectively. 1σ, 2σ and 3σ intervals are investigated. "Fit" refers to the credible interval edges from MaCh3 data fit results with reactor constraint; "Increment" refers to the extreme shift values from the fake data study results (Table 4 of TN457 v1.3 [11]); "Fit+Increment" refers to the credible interval edges after applying the shift values from fake data studies. The criteria of "Pass" is to check whether the credible interval after applying the shift contains any one of the $\delta_{\rm CP}$ values $-\pi, 0, \pi$. "LE" refers to the lower edge of the interval and "UE" refers to the upper edge. Note that "LE" is not necessarily smaller than "UE" because of wrapping through $-\pi = \delta_{\rm CP} = \pi$. For simplification, the interval edges for a specific sigma are the most extreme values among all connected intervals.

4.1.2 Parameter constraints, prior flat in $\sin\delta_{\rm CP}$

The results until now have applied a flat prior on $\delta_{\rm CP}$, as is commonplace in T2K and SK analyses. However, the variable which the flat prior is being applied has the ability to shape the posterior, especially if the constraint from the data on the posterior is weak. For example, a prior flat in $\delta_{\rm CP}$ is not the same as a prior flat in $\sin\delta_{\rm CP}$, since the former down-weights probabilities around $\pm\pi/2$. The $P(\nu_\mu \to \nu_e) - P(\bar{\nu}_\mu \to \bar{\nu}_e)$ has dependence on $\sin\delta_{\rm CP}$, not $\delta_{\rm CP}$. Hence, studying the impact of the shape of the prior on $\delta_{\rm CP}$ is important, especially when intending to make definitive statements on particular credible intervals. All results in this section applies the reactor constraint on $\sin^2\theta_{13}$.

Fig. 45 shows the one-dimensional posteriors for each mass ordering for $\delta_{\rm CP}$ with a prior flat in $\sin\delta_{\rm CP}$. Compared to the prior flat in $\delta_{\rm CP}$, this prior choice enforces a strong zero prior at the maximal CP violation points, $\cos\delta_{CP} = 0$, i.e. when $\delta_{\rm CP} = \pm\pi/2$. Hence, the credible intervals are discontinuous around $\delta_{\rm CP} = \pi/2$, which is near the maximal posterior density when a prior flat in $\delta_{\rm CP}$ was used.

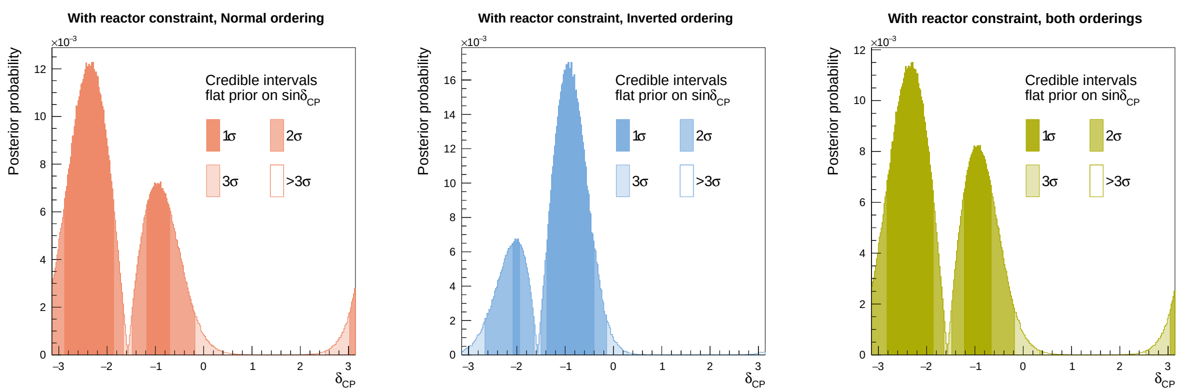

Figure 45: $\delta_{\rm CP}$ for the real data analysis, with the reactor constraint applied and a flat prior on $\sin\delta_{\rm CP}$, for normal (left), inverted (center), and both (right) orderings.

Fig. 46 and Fig. 47 show the Δm^2_{32} and $\sin^2\theta_{13}$ posteriors, respectively, which show little dependence on this choice of priors, owing largely to the lack of correlation with $\delta_{\rm CP}$.

Fig. 48 shows the results for $\sin^2\theta_{23}$, where we see a slightly more peaked distribution for the normal ordering, but otherwise looks the same.

The one-dimensional posteriors are compared in detail for the two choices of priors in Sec. 4.3.

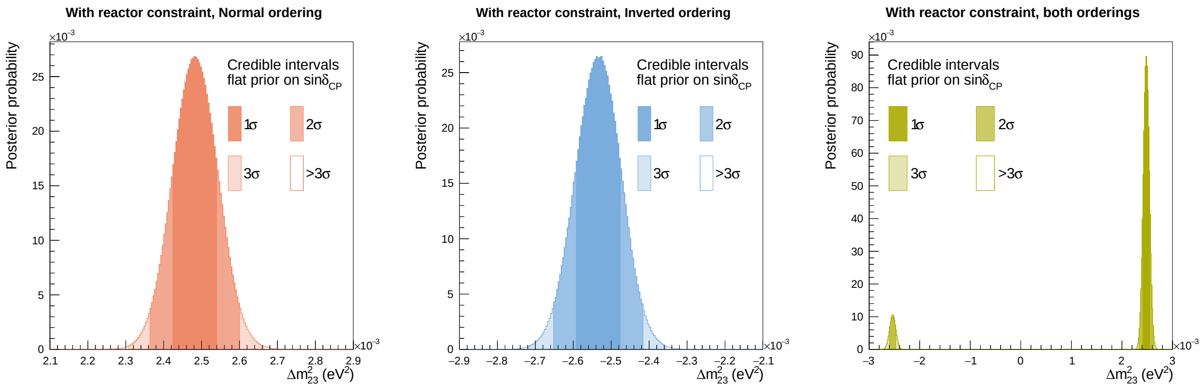

Figure 46: Δm^2_{32} for the real data analysis, with the reactor constraint applied and a flat prior on $\sin\delta_{\rm CP}$, for normal (left), inverted (center), and both (right) orderings.

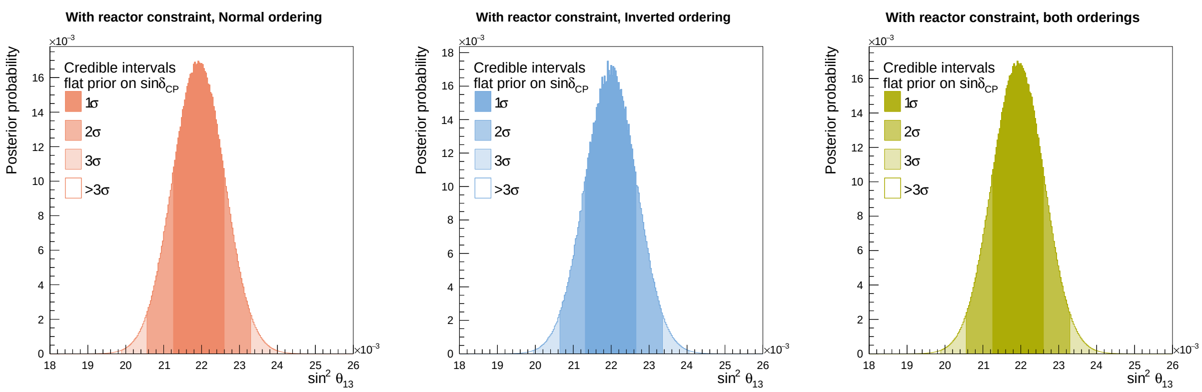

Figure 47: $\sin^2\theta_{13}$ for the real data analysis, with the reactor constraint applied and a flat prior on $\sin\delta_{\rm CP}$, for normal (left), inverted (center), and both (right) orderings.

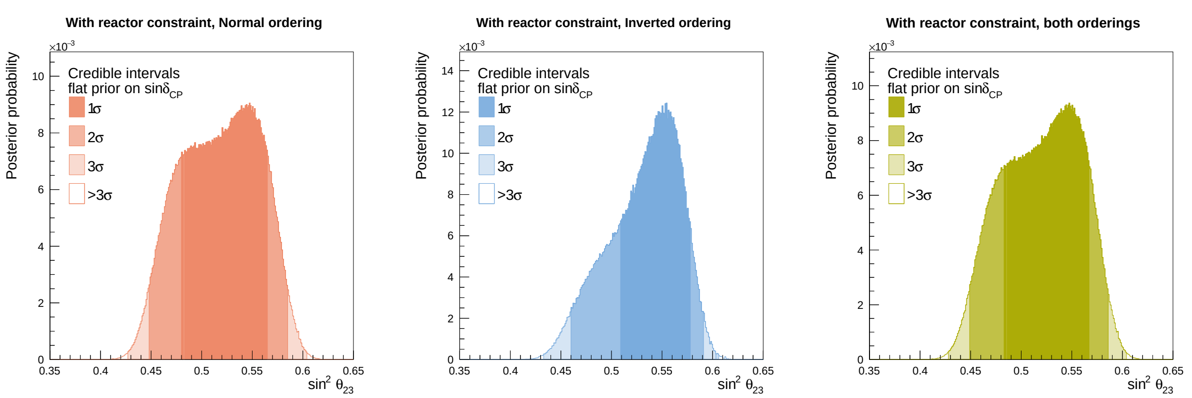

Figure 48: $\sin^2\theta_{23}$ for the real data analysis, with the reactor constraint applied and a flat prior on $\sin\delta_{\rm CP}$, for normal (left), inverted (center), and both (right) orderings.

The Jarlskog invariant Fig. 49 and Fig. 50 show the marginalised Jarlskog invariant (J) posterior for normal ordering, inverted ordering and both ordering, shown separately with a flat prior on δ_{CP} and flat prior on $\sin\delta_{\mathrm{CP}}$.

For the J with flat prior on δ_{CP}, $J = 0$ is comfortably excluded at more than 2σ credible level for all choices of mass ordering. With a prior flat in $\sin\delta_{\mathrm{CP}}$, the constraint on J lessens, and $J = 0$ is just excluded at 2σ credible interval, driven by the normal ordering.

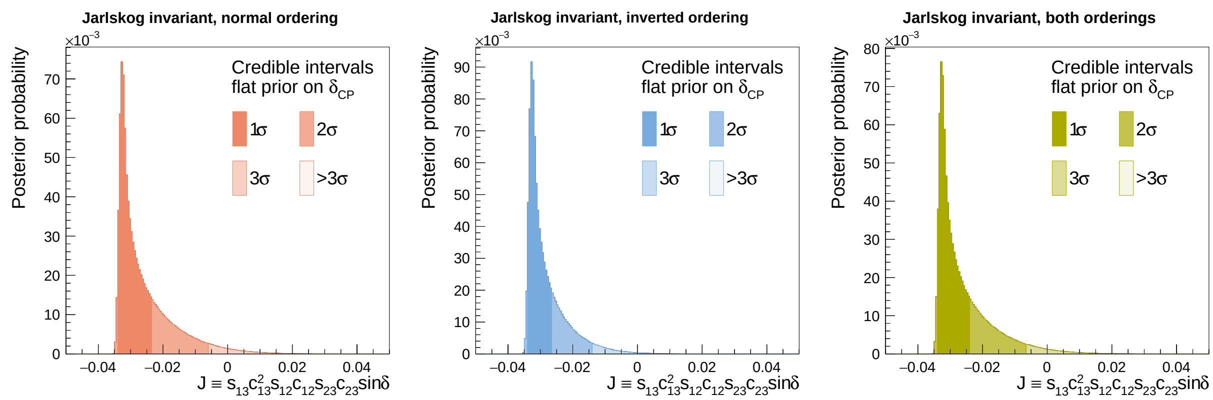

Figure 49: J for the real data analysis, with the reactor constraint applied, for normal (left), inverted (center), and both (right) orderings, with a flat prior on δ_{CP}.

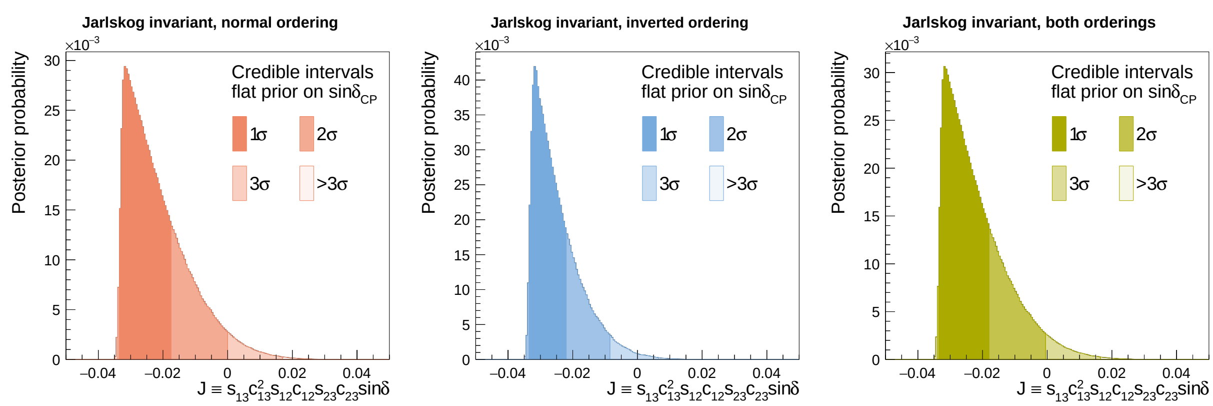

Figure 50: J for the real data analysis, with the reactor constraint applied, for normal (left), inverted (center), and both (right) orderings, with a flat prior on $\sin\delta_{\mathrm{CP}}$.

Two-dimensional posteriors Fig. 51, Fig. 52, Fig. 53, Fig. 54, Fig. 55, Fig. 56 and Fig. 57 show the two-dimensional marginal posteriors for $\delta_{\mathrm{CP}} - \sin^2\theta_{13}$, $\delta_{\mathrm{CP}} - \sin^2\theta_{23}$, $\delta_{\mathrm{CP}} - \Delta m^2_{32}$, $\Delta m^2_{32} - \sin^2\theta_{13}$, $\Delta m^2_{32} - \sin^2\theta_{23}$, $\sin^2\theta_{13} - \sin^2\theta_{23}$ and $\sin^2\theta_{23} - \Delta m^2_{32}$, respectively. These are shown separately for normal ordering, inverted ordering and both orderings, all applying the reactor constraint.

As with the Asimov A studies, the number of MCMC steps and the chosen binning is not sufficient to make reliable 3σ statements, and the 3σ credible interval should only be used to guide the reader for the approximate exclusion, and no accurate statistical statements should be made about 3σ exclusion.

In general, the results are roughly compatible with the expected sensitivity from the Asimov A analysis.

Compared to the main T2K-only results (see Fig 80 in TN393 [1]), the correlation between $\sin^2\theta_{23}$ and $\sin^2\theta_{13}$ in Fig. 56, and $\sin^2\theta_{23}$ and δ_{CP} in Fig. 52, are relaxed in the joint analysis, and they are almost independent. Similar can be said about $\sin^2\theta_{23}$ and Δm^2_{32}, likely due to the maximum likelihood being around maximal mixing.

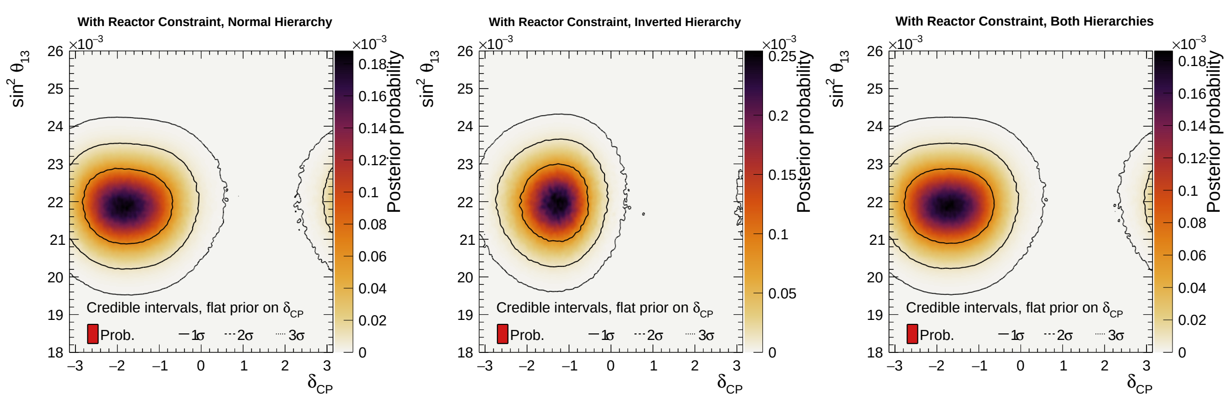

Figure 51: $\delta_{\mathrm{CP}} - \sin^2\theta_{13}$ for the real data analysis, with the reactor constraint applied, for normal (left), inverted (center), and both (right) orderings.

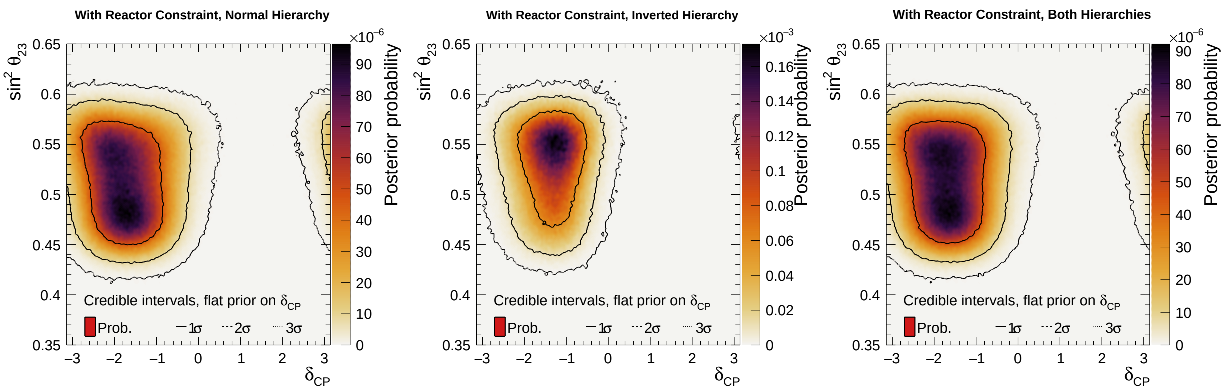

Figure 52: $\delta_{\rm CP} - \sin^2\theta_{23}$ for the real data analysis, with the reactor constraint applied, for normal (left), inverted (center), and both (right) orderings.

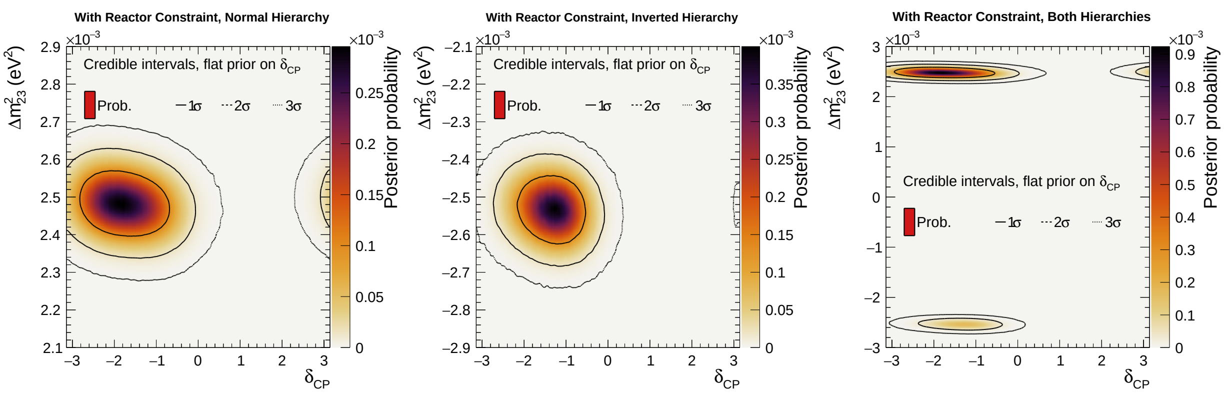

Figure 53: $\delta_{\rm CP} - \Delta m^2_{32}$ for the real data analysis, with the reactor constraint applied, for normal (left), inverted (center), and both (right) orderings.

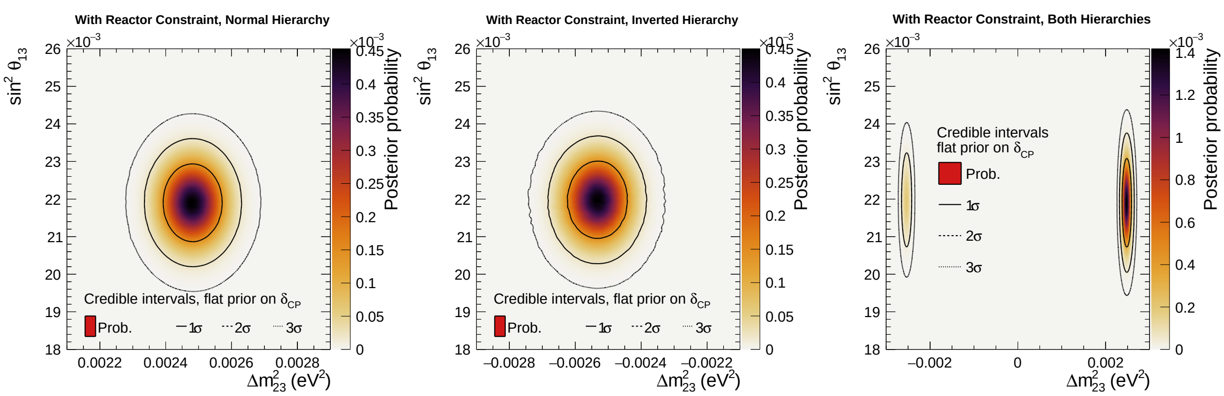

Figure 54: $\Delta m^2_{32} - \sin^2\theta_{13}$ for the real data analysis, with the reactor constraint applied, for normal (left), inverted (center), and both (right) orderings.

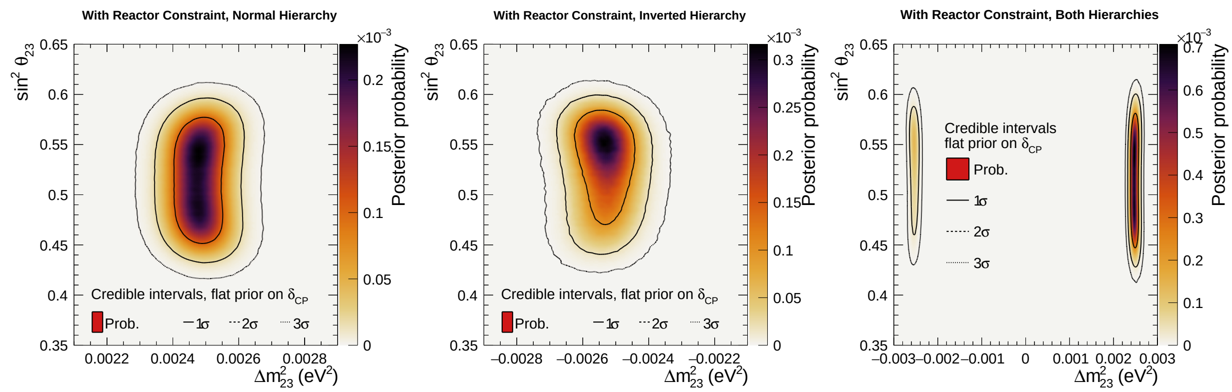

Figure 55: $\Delta m^2_{32} - \sin^2\theta_{23}$ for the real data analysis, with the reactor constraint applied, for normal (left), inverted (center), and both (right) orderings.

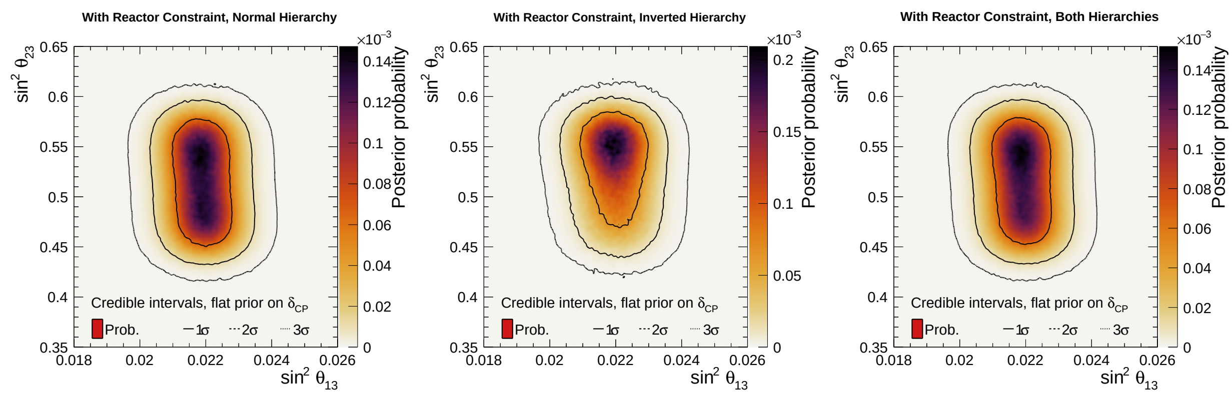

Figure 56: $\sin^2\theta_{13} - \sin^2\theta_{23}$ for the real data analysis, with the reactor constraint applied, for normal (left), inverted (center), and both (right) orderings.

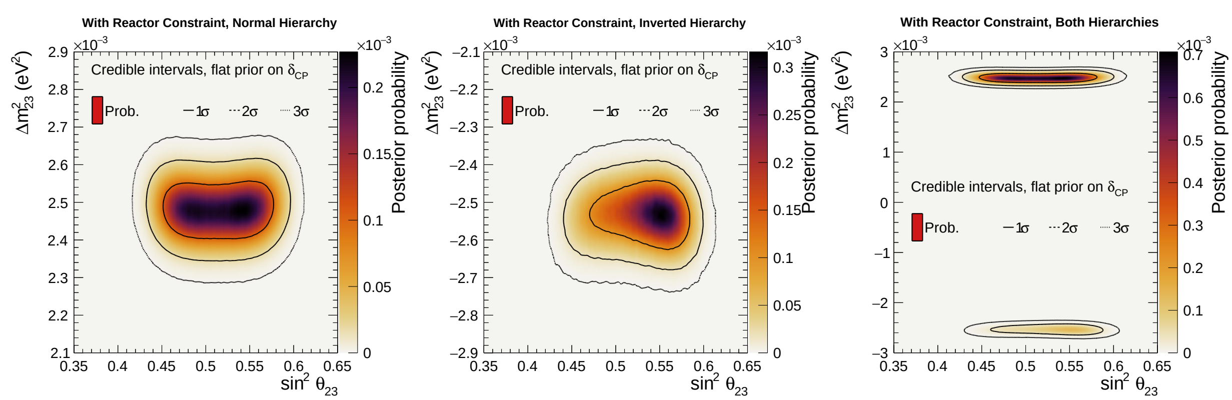

Figure 57: $\sin^2\theta_{23} - \Delta m^2_{32}$ for the real data analysis, with the reactor constraint applied, for normal (left), inverted (center), and both (right) orderings.

The Jarlskog invariant Fig. 58 and Fig. 59 show the two-dimensional $J - \sin^2\theta_{23}$ posteriors for normal ordering, inverted ordering and both orderings, with a flat prior on δ_{CP} and $\sin\delta_{\mathrm{CP}}$ respectively. Fig. 60 shows the two-dimensional $J - \delta_{\mathrm{CP}}$ posteriors for the orderings, with a flat prior on δ_{CP}.

As in the Asimov A studies and the one-dimensional posterior from the data analysis, the posterior for the analysis using a prior flat in $\sin\delta_{\mathrm{CP}}$ has a larger 1σ credible interval. The 2σ and 3σ intervals are much more similar than the 1σ interval for the two choices of flat prior.

We see the strongest constraint on J in the inverted hierarchy and the lower octant, as expected from the analysis of the one-dimensional posteriors from the data. This agrees with the expectation of the impact of the prior; a prior flat in δ_{CP} emphasises the extreme solutions at $|J| \sim 0.03$.

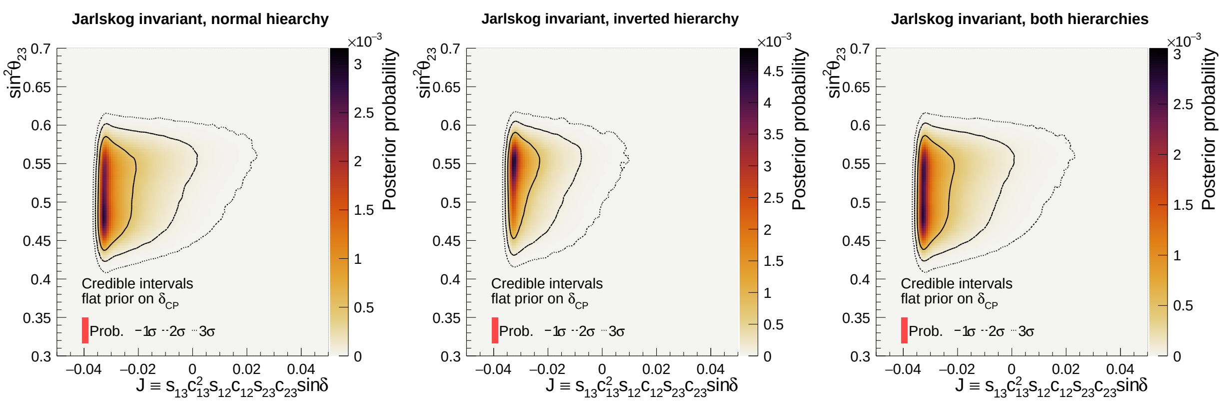

Figure 58: $J - \sin^2\theta_{23}$ for the real data analysis, with the reactor constraint applied, for normal (left), inverted (center), and both (right) orderings, with a flat prior on δ_{CP}.

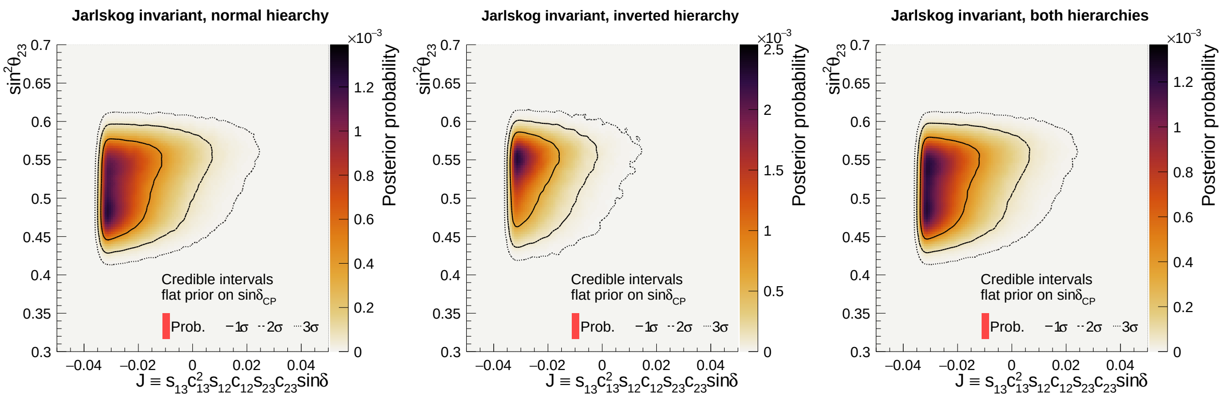

Figure 59: $J - \sin^2\theta_{23}$ for the real data analysis, with the reactor constraint applied, for normal (left), inverted (center), and both (right) orderings, with a flat prior on $\sin\delta_{\rm CP}$.

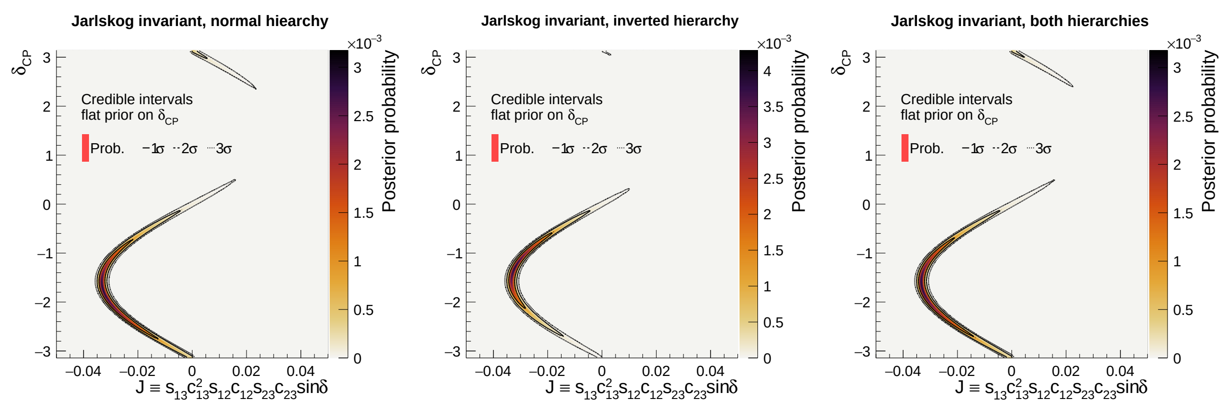

Figure 60: $J - \delta_{\rm CP}$ for the real data analysis, with the reactor constraint applied, for normal (left), inverted (center), and both (right) orderings, with a flat prior on $\delta_{\rm CP}$.

4.1.3 Triangle plots

Fig. 61, Fig. 62, and Fig. 63 show the one and two-dimensional oscillation parameters' posteriors, displayed in triangular form. These all apply the reactor constraint and use a flat prior on δ_{CP}.

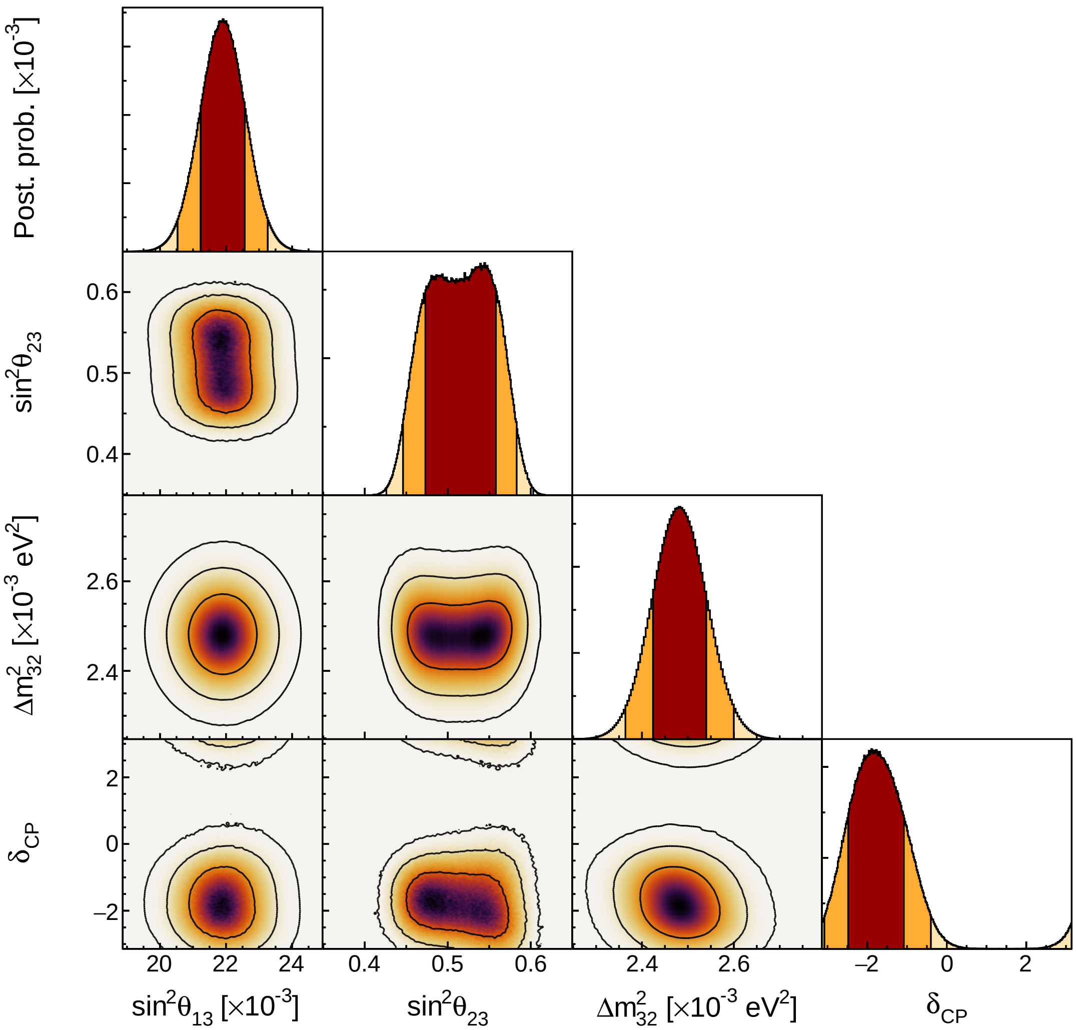

Figure 61: Triangle plots for the real data analysis, with the reactor constraint applied, for the normal ordering, with a flat prior on $\delta_{\rm CP}$. The 1, 2, and 3σ credible intervals are overlaid on the posterior.

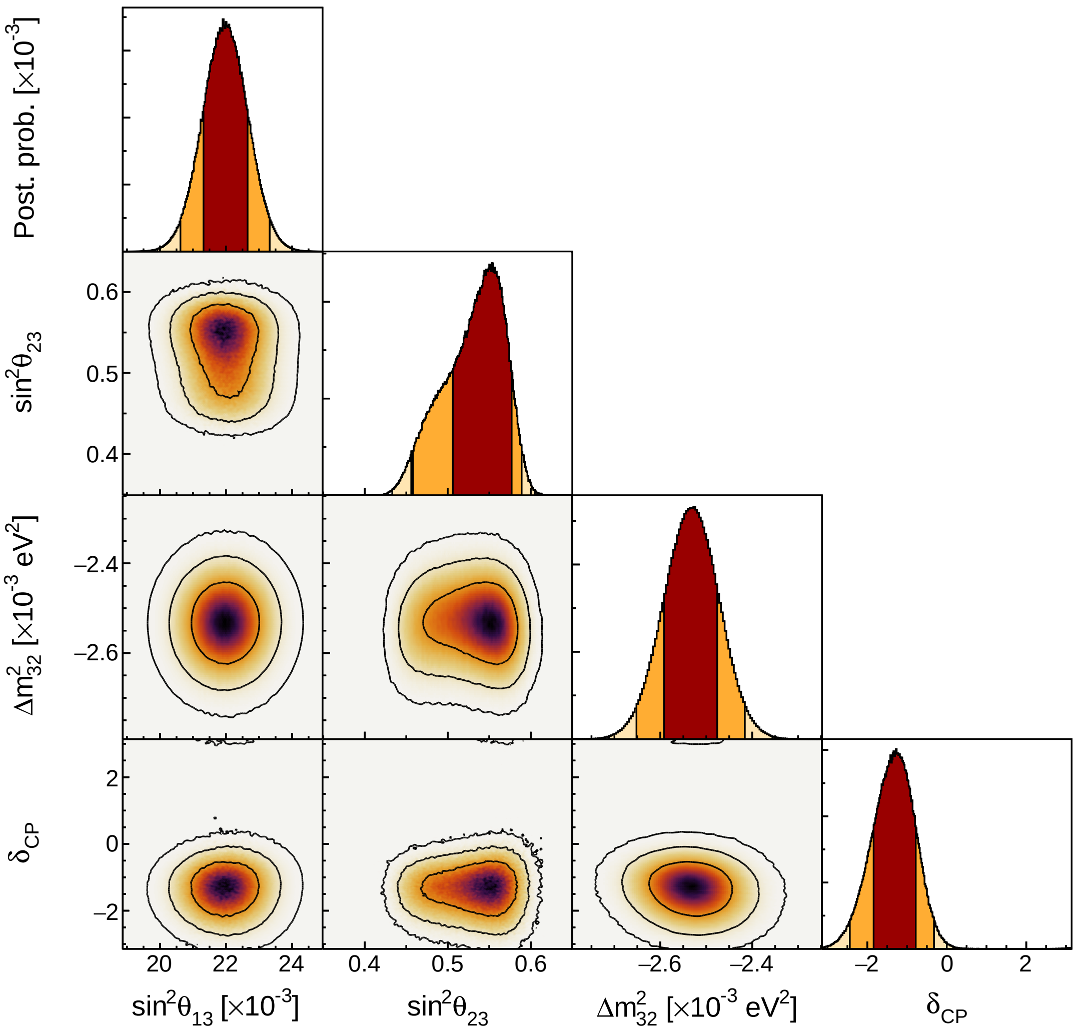

Figure 62: Triangle plots for the real data analysis, with the reactor constraint applied, for the inverted ordering, with a flat prior on $\delta_{\rm CP}$. The 1, 2, and 3σ credible intervals are overlaid on the posterior.

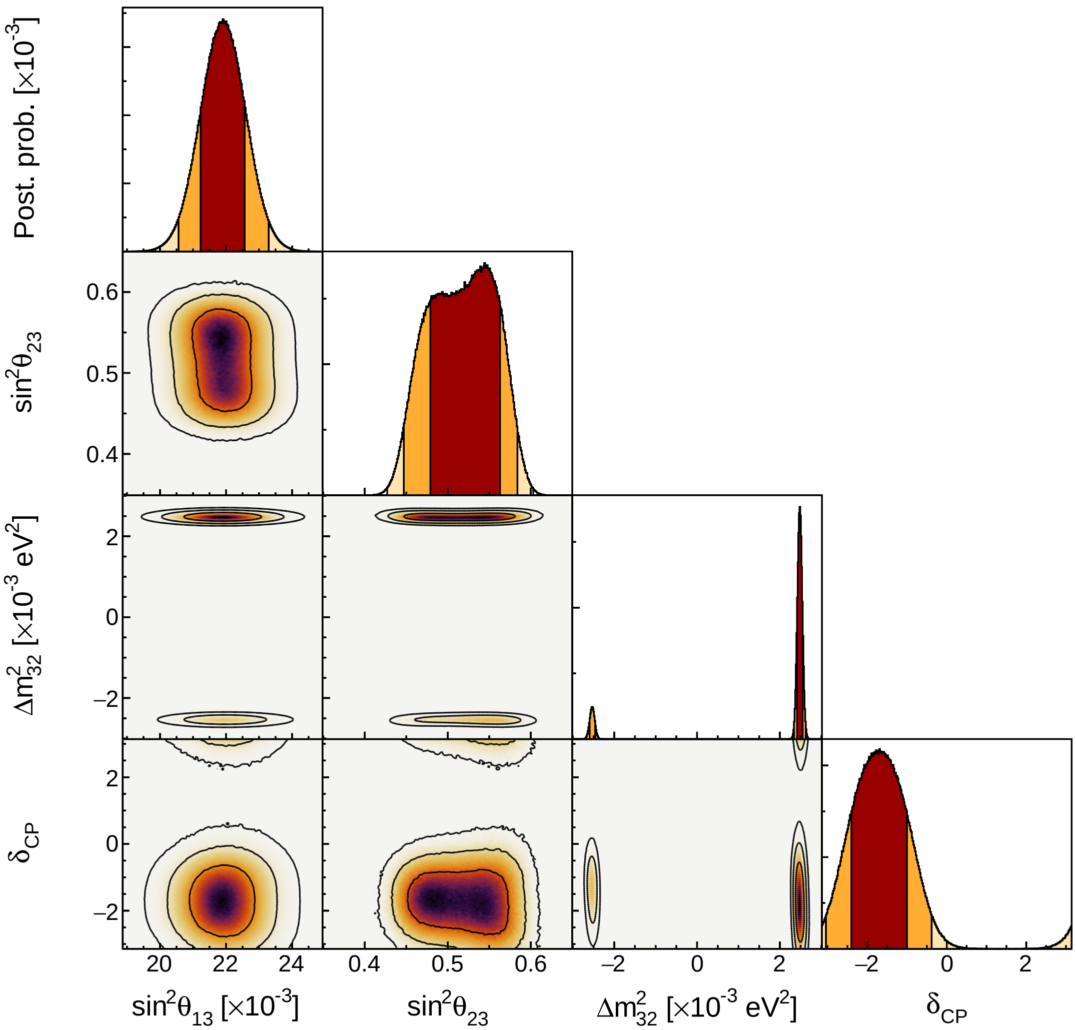

Figure 63: Triangle plots for the real data analysis, with the reactor constraint applied, for both orderings, with a flat prior on δ_{CP}. The 1, 2, and 3σ credible intervals are overlaid on the posterior.

4.1.4 Bayes factors for atmospheric parameters

Posterior probabilities from the data fit with reactor constraint for different hypothesis applying the reactor constraint are calculated and summarized in Tab. 2. The Bayes factor of upper octant over lower octant is $B(\mathrm{UO/LO}) = 1.78$ and the Bayes factor of normal ordering over inverted ordering is $B(\mathrm{NO/IO}) = 7.33$. The combined Bayes factor for UO and IO is weak, with $B([\mathrm{UO{+}NO}]/\mathrm{Other}) = 1.17$. These posterior probabilities are compatible with P-Theta's MCMC results in the data fit TN459 [12], and the mass ordering Bayes factor is notably stronger and the octant preference is weaker than the T2K-only analysis in TN393 [1]. Therein, T2K finds $B(\mathrm{NO/IO}) = 4.2$ and $B(\mathrm{UO/LO}) = 3.36$.

	$\sin^2\theta_{23} < 0.5$	$\sin^2\theta_{23} > 0.5$	Sum
NO	0.33	0.54	0.88
IO	0.03	0.10	0.12
Sum	0.36	0.64	1.00

Table 7: Posterior probabilities for the mass ordering and the octant in the real data analysis, with the reactor constraint applied.

4.2 Results without applying the reactor constraint

This section is dedicated to the data fit results without applying the reactor constraint on $\sin^2\theta_{13}$. The same data fit chains are used with a burn-in of 80,000 steps per independent chain.

4.2.1 Parameter constraints

Each parameter constraint in this section is shown in normal ordering ($\Delta m^2_{32} > 0$), inverted ordering ($\Delta m^2_{32} < 0$), and over bother orderings.

One-dimensional posteriors Fig. 64, Fig. 65, Fig. 66, and Fig. 67 show the marginalised one-dimensional posterior for δ_{CP}, Δm^2_{32}, $\sin^2\theta_{13}$ and $\sin^2\theta_{23}$, respectively.

As for the results with reactor constraint applied, the constraint on δ_{CP} is weaker in the normal ordering in Fig. 64. $\delta_{\text{CP}} = 0$ is just excluded at 2σ credible interval, and $\delta_{\text{CP}} = -\pi$ is included. The result in normal ordering is compatible with inverted ordering, although the inverted ordering highest posterior density is near $\delta_{\text{CP}} \sim -1$ whereas in normal ordering $\delta_{\text{CP}} \sim -2$.

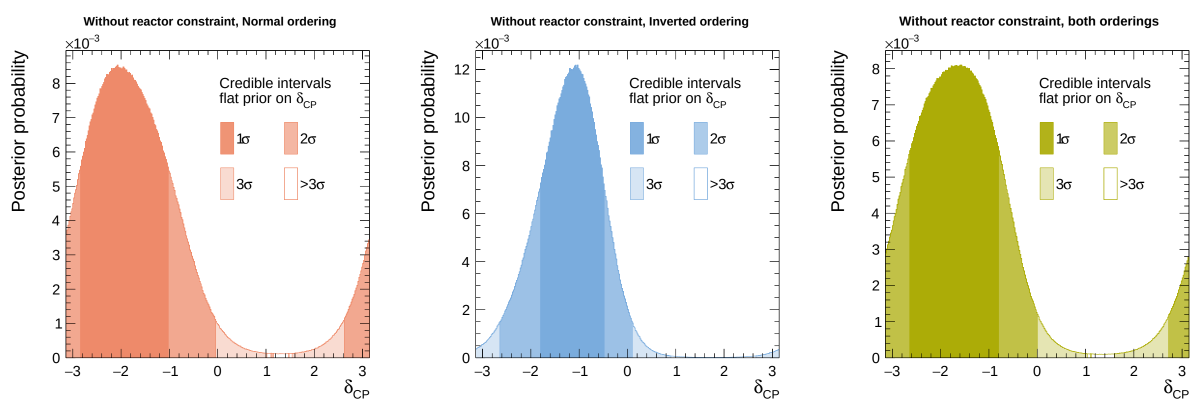

Figure 64: δ_{CP} for the real data analysis, without the reactor constraint applied, for normal (left), inverted (center), and both (right) orderings.

As for the mass ordering, Fig. 65 shows a similar but weaker preference for normal ordering.

The constraint on $\sin^2\theta_{13}$ in Fig. 66 is compatible with the reactor constraint, and is the impact of the reactor constraint is shown in more detail in Sec. 4.4.

The constraint on $\sin^2\theta_{23}$ without the reactor constraint consistently weakly prefers the lower octant for both orderings individually and combined. The constraint is weak, and the

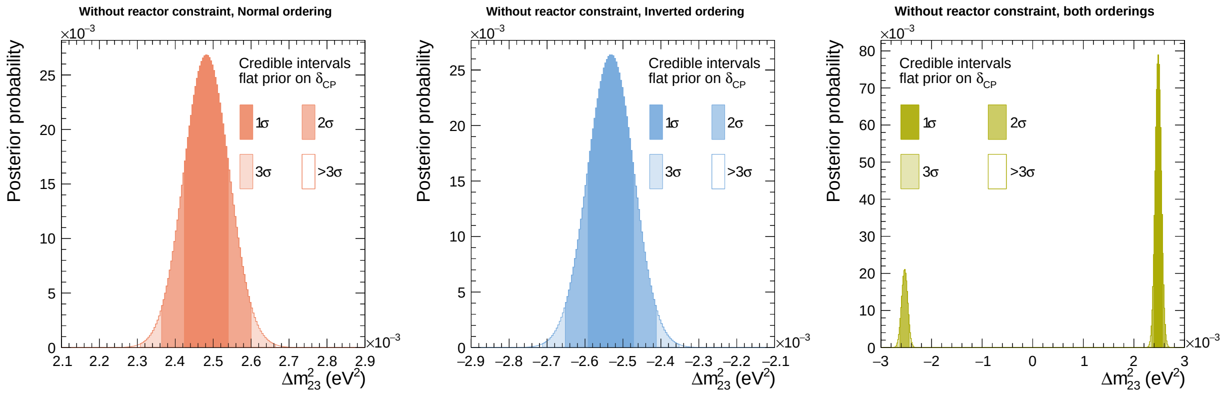

Figure 65: Δm^2_{32} for the real data analysis, without the reactor constraint applied, for normal (left), inverted (center), and both (right) orderings.

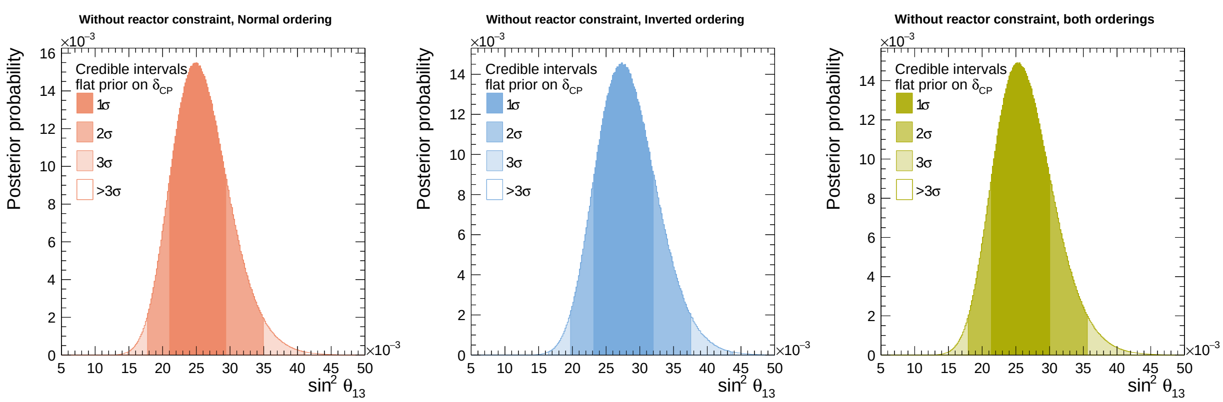

Figure 66: $\sin^2\theta_{13}$ for the real data analysis, without the reactor constraint applied, for normal (left), inverted (center), and both (right) orderings.

upper octant is also inside the 1σ credible interval, although the highest posterior density is in the lower octant. This is tabulated in the section dedicated to Bayes factors, Sec. 4.2.3.

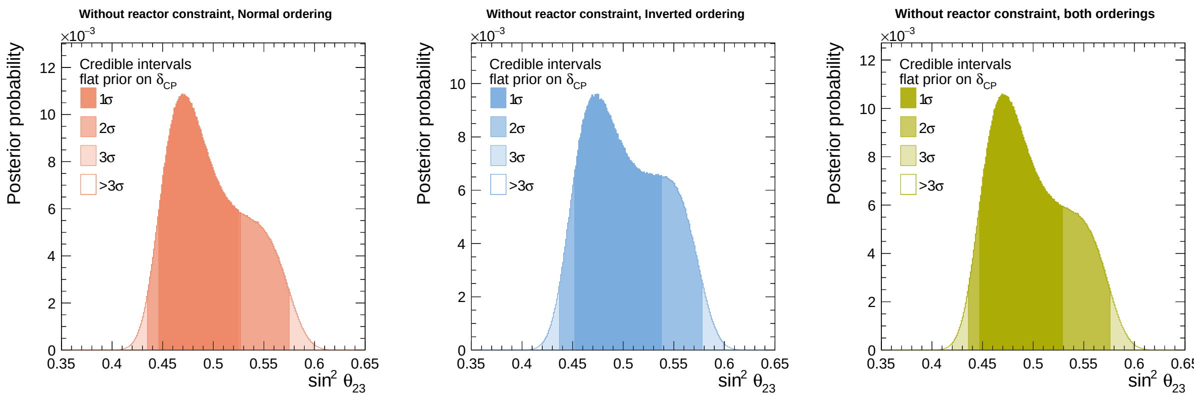

Figure 67: $\sin^2\theta_{23}$ for the real data analysis, without the reactor constraint applied, for normal (left), inverted (center), and both (right) orderings.

The Jarlskog invariant Fig. 68 and Fig. 69 show the marginalised Jarlskog invariant (J) posterior for normal ordering, inverted ordering and both orderings with flat prior on $\delta_{\rm CP}$ and $\sin\delta_{\rm CP}$, respectively.

$J = 0$ is excluded between 1-2σ for both priors.

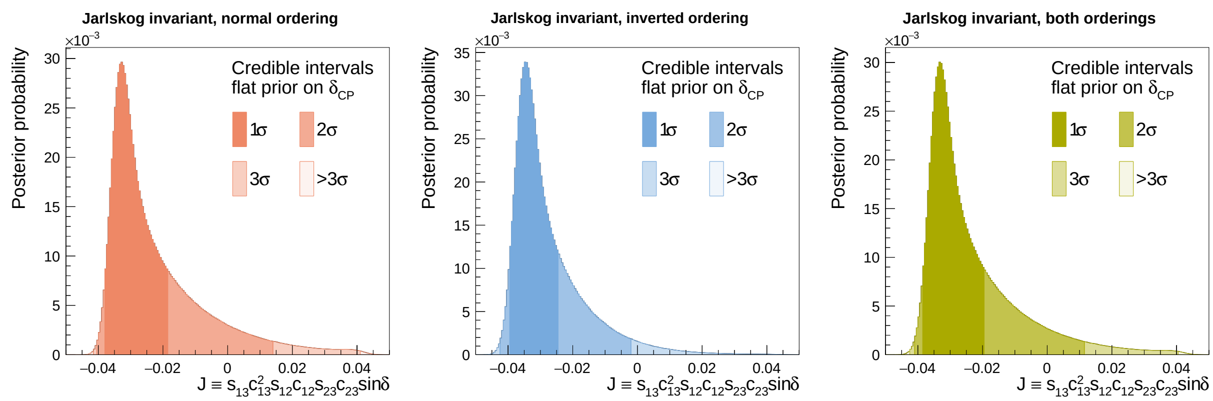

Figure 68: J for the real data analysis, without the reactor constraint applied, for normal (left), inverted (center), and both (right) orderings, with a flat prior on $\delta_{\rm CP}$.

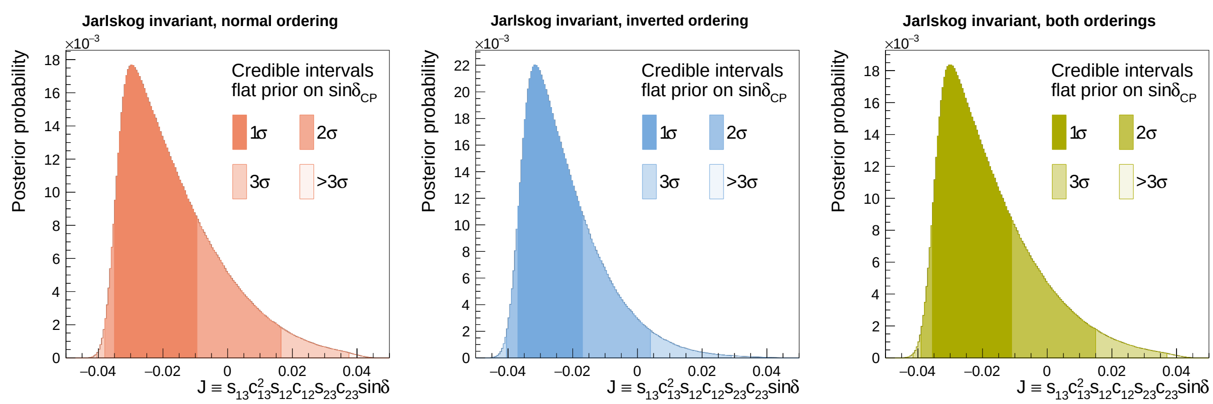

Figure 69: J for the real data analysis, without the reactor constraint applied, for normal (left), inverted (center), and both (right) orderings, with a flat prior on $\sin\delta_{\rm CP}$.

Two-dimensional posteriors Fig. 70, Fig. 71, Fig. 72, Fig. 73, Fig. 74, Fig. 75 and Fig. 76 show the two-dimensional marginal posteriors for $\delta_{\text{CP}} - \sin^2\theta_{13}$, $\delta_{\text{CP}} - \sin^2\theta_{23}$, $\delta_{\text{CP}} - \Delta m^2_{32}$, $\Delta m^2_{32} - \sin^2\theta_{13}$, $\Delta m^2_{32} - \sin^2\theta_{23}$, $\sin^2\theta_{13} - \sin^2\theta_{23}$ and $\sin^2\theta_{23} - \Delta m^2_{32}$, respectively. These are shown separately for normal ordering, inverted ordering and both orderings, all without applying the reactor constraint.

Firstly, in Fig. 70 we notice a different δ_{CP} and $\sin^2\theta_{13}$ correlation for normal and inverted orderings, and a different maximum of the posterior density. The normal ordering result favours a more negative δ_{CP} alongside a smaller $\sin^2\theta_{13}$ with a negative correlation, and the inverted ordering favours a less negative value of δ_{CP} alongside a larger $\sin^2\theta_{13}$ with a positive correlation.

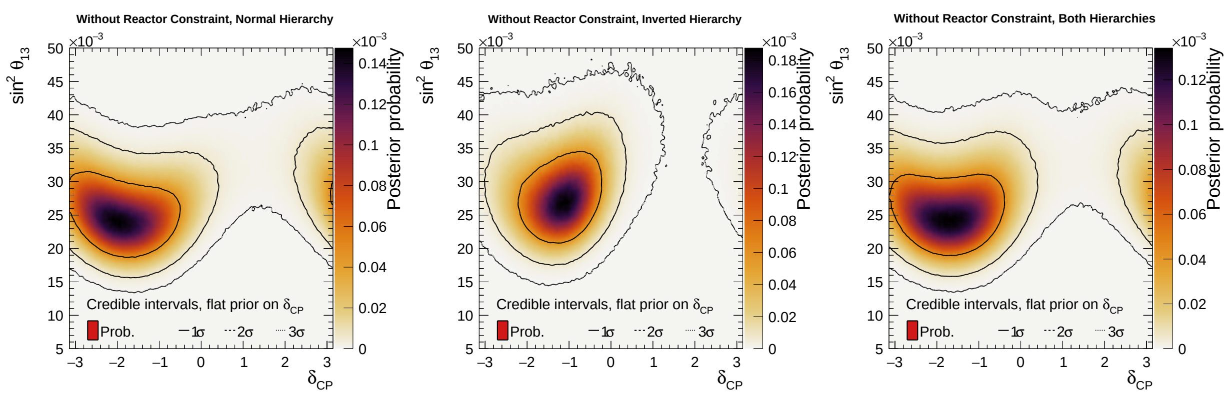

Figure 70: $\delta_{\text{CP}} - \sin^2\theta_{13}$ for the real data analysis, without the reactor constraint applied, for normal (left), inverted (center), and both (right) orderings.

For the $\delta_{\text{CP}} - \sin^2\theta_{23}$ result in Fig. 71, the constraint on δ_{CP} is weakest in the lower octant (which has the highest posterior density), especially in the normal ordering. For inverted ordering, the two are barely correlated.

For the $\sin^2\theta_{13} - \sin^2\theta_{23}$ posterior in Fig. 75, there is now an evident anti-correlation, whereas the analysis applying the reactor constraint showed barely any correlation. This stems from the external constraint on $\sin^2\theta_{13}$ decorrelating the two. The correlation is roughly the same in both hierarchies.

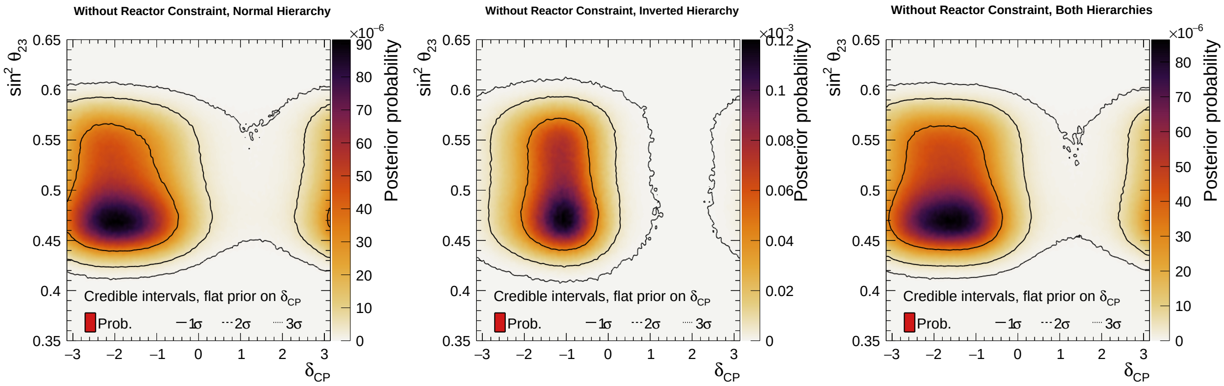

Figure 71: $\delta_{\mathrm{CP}} - \sin^2\theta_{23}$ for the real data analysis, without the reactor constraint applied, for normal (left), inverted (center), and both (right) orderings.

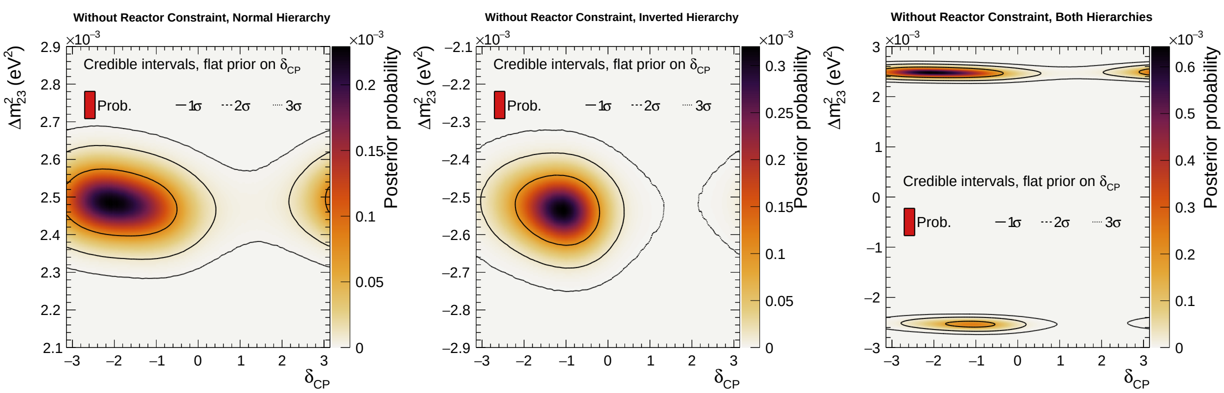

Figure 72: $\delta_{\mathrm{CP}} - \Delta m^2_{32}$ for the real data analysis, without the reactor constraint applied, for normal (left), inverted (center), and both (right) orderings.

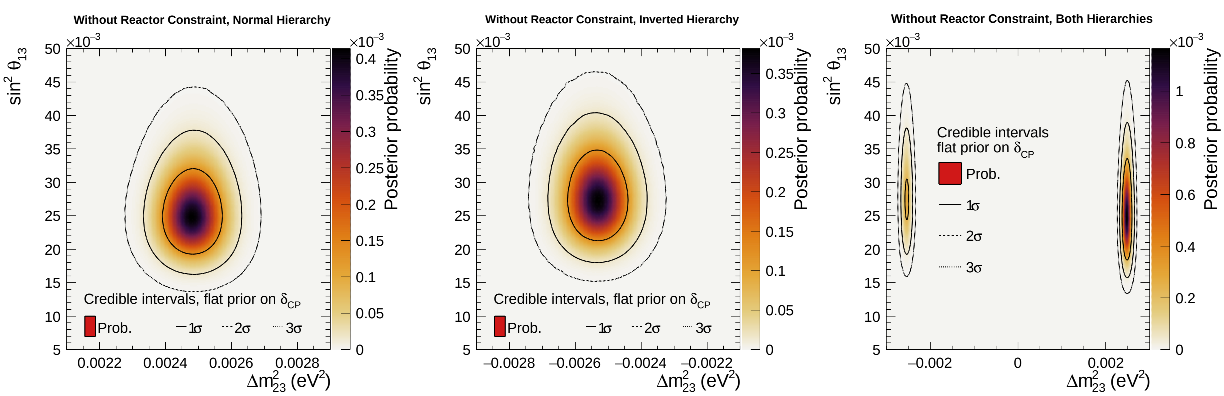

Figure 73: $\Delta m^2_{32} - \sin^2\theta_{13}$ for the real data analysis, without the reactor constraint applied, for normal (left), inverted (center), and both (right) orderings.

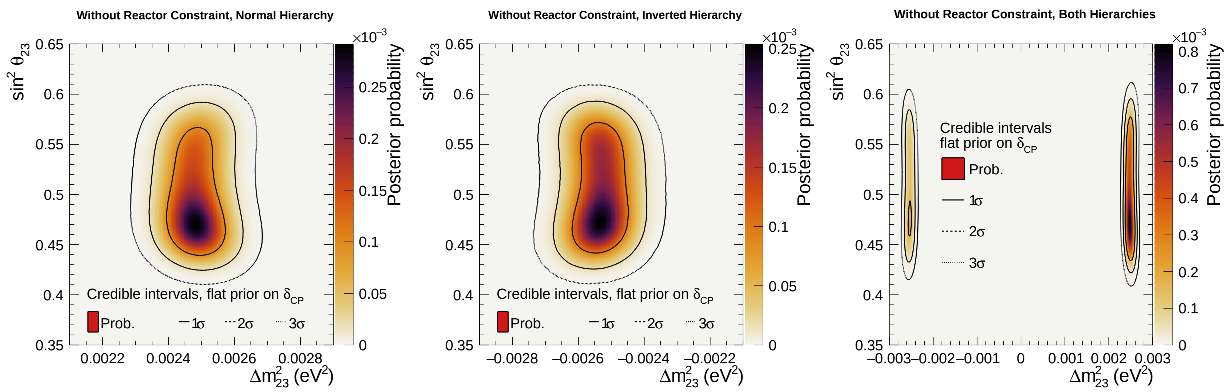

Figure 74: $\Delta m^2_{32} - \sin^2\theta_{23}$ for the real data analysis, without the reactor constraint applied, for normal (left), inverted (center), and both (right) orderings.

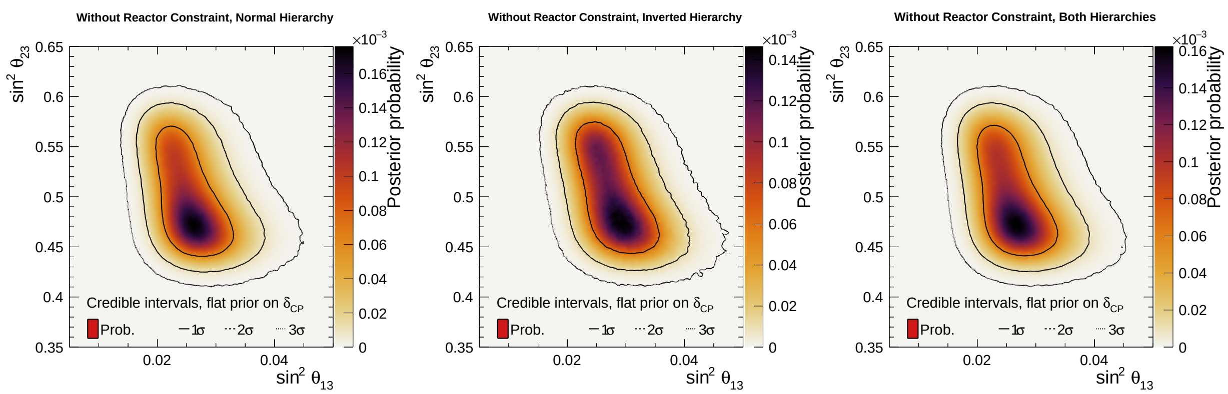

Figure 75: $\sin^2\theta_{13} - \sin^2\theta_{23}$ for the real data analysis, without the reactor constraint applied, for normal (left), inverted (center), and both (right) orderings.

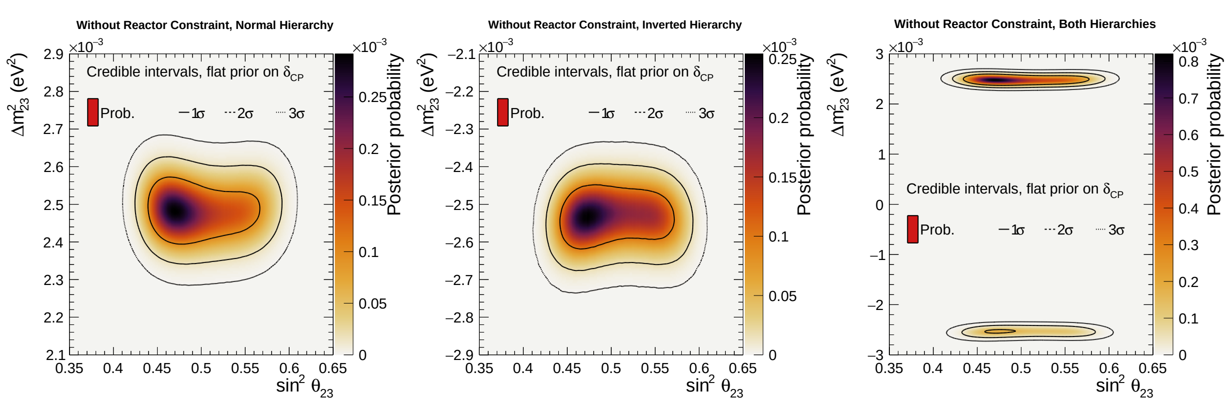

Figure 76: $\sin^2\theta_{23} - \Delta m^2_{32}$ for the real data analysis, without the reactor constraint applied, for normal (left), inverted (center), and both (right) orderings.

The Jarlskog invariant Fig. 77 and Fig. 78 show the two-dimensional $J - \sin^2\theta_{23}$ posteriors for normal ordering, inverted ordering and both orderings, with a flat prior on $\delta_{\rm CP}$ and $\sin\delta_{\rm CP}$ respectively. Fig. 79 shows the two-dimensional $J - \delta_{\rm CP}$ posteriors for the orderings, with a flat prior on $\delta_{\rm CP}$.

As for the two-dimensional $\delta_{\rm CP} - \sin^2\theta_{23}$ posteriors, J is more strongly constrained in the upper octant when the reactor constraint isn't applied. For instance, $J = 0$ is just barely excluded at 1σ in the lower octant for the analysis using a prior flat in $\sin\delta_{\rm CP}$ when marginalising over both orderings and the normal ordering only.

As seen in both the Asimov A analysis and the data analysis, the prior flat in $\delta_{\rm CP}$ or $\sin\delta_{\rm CP}$ mainly impact the 1σ credible interval, and the 2 and 3σ intervals are very similar regardless of prior choice. The positive J solution weakly appears in the analysis with a flat prior on $\delta_{\rm CP}$, but there is less probability there than in the Asimov A study.

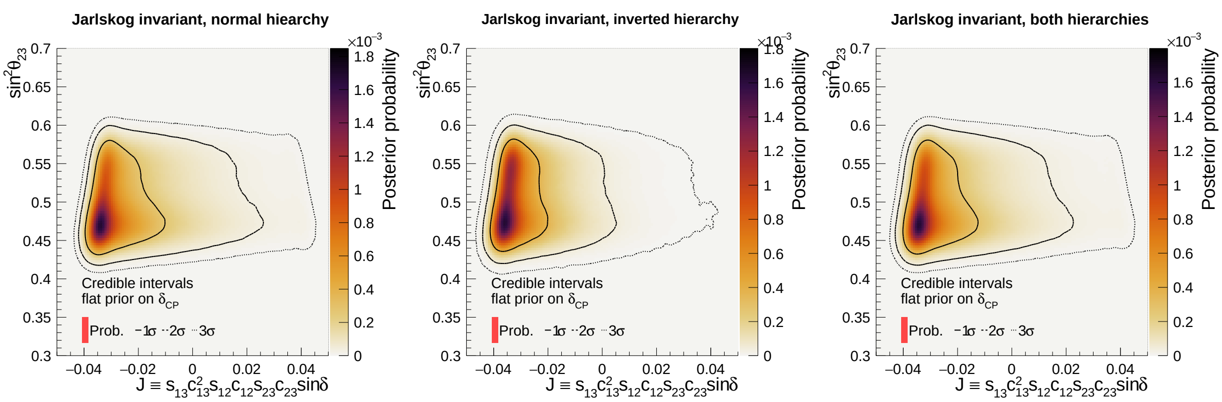

Figure 77: $J - \sin^2\theta_{23}$ for the real data analysis, without the reactor constraint applied, for normal (left), inverted (center), and both (right) orderings, with a flat prior on $\delta_{\rm CP}$.

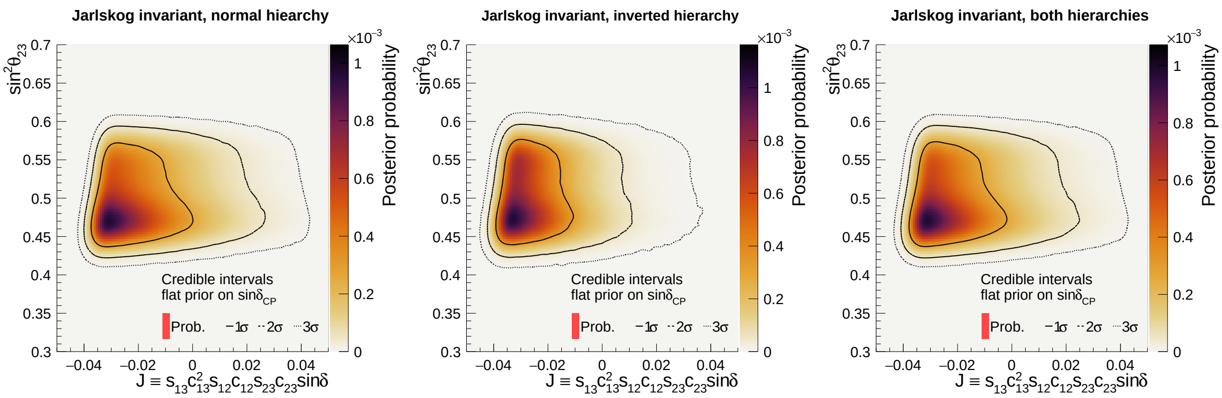

Figure 78: $J - \sin^2\theta_{23}$ for the real data analysis, without the reactor constraint applied, for normal (left), inverted (center), and both (right) orderings, with a flat prior on $\sin\delta_{\mathrm{CP}}$.

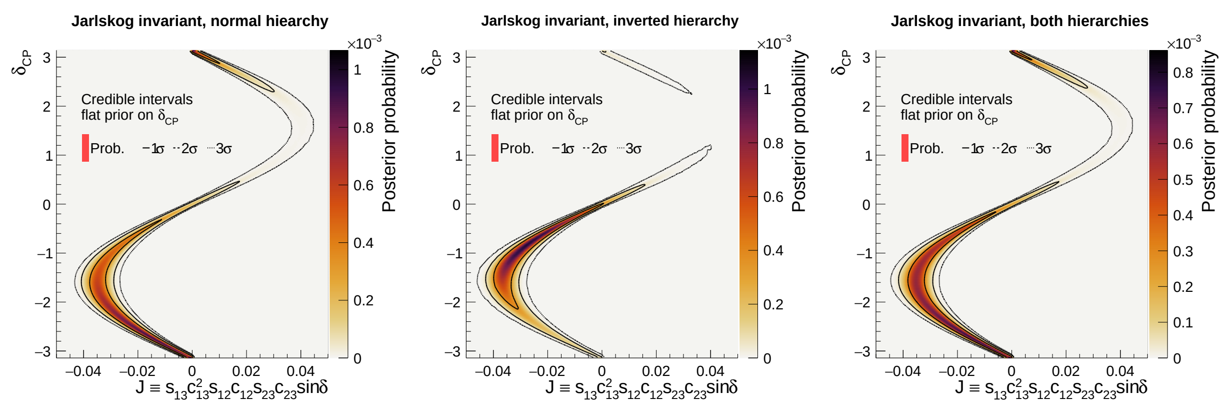

Figure 79: $J - \delta_{\mathrm{CP}}$ for the real data analysis, without the reactor constraint applied, for normal (left), inverted (center), and both (right) orderings, with a flat prior on δ_{CP}.

4.2.2 Triangle plots

Fig. 80, Fig. 81, and Fig. 82 show the one and two-dimensional oscillation parameters' posteriors, displayed in triangular form, summarising the main results. These do not apply the reactor constraint, and use a flat prior on δ_{CP}.

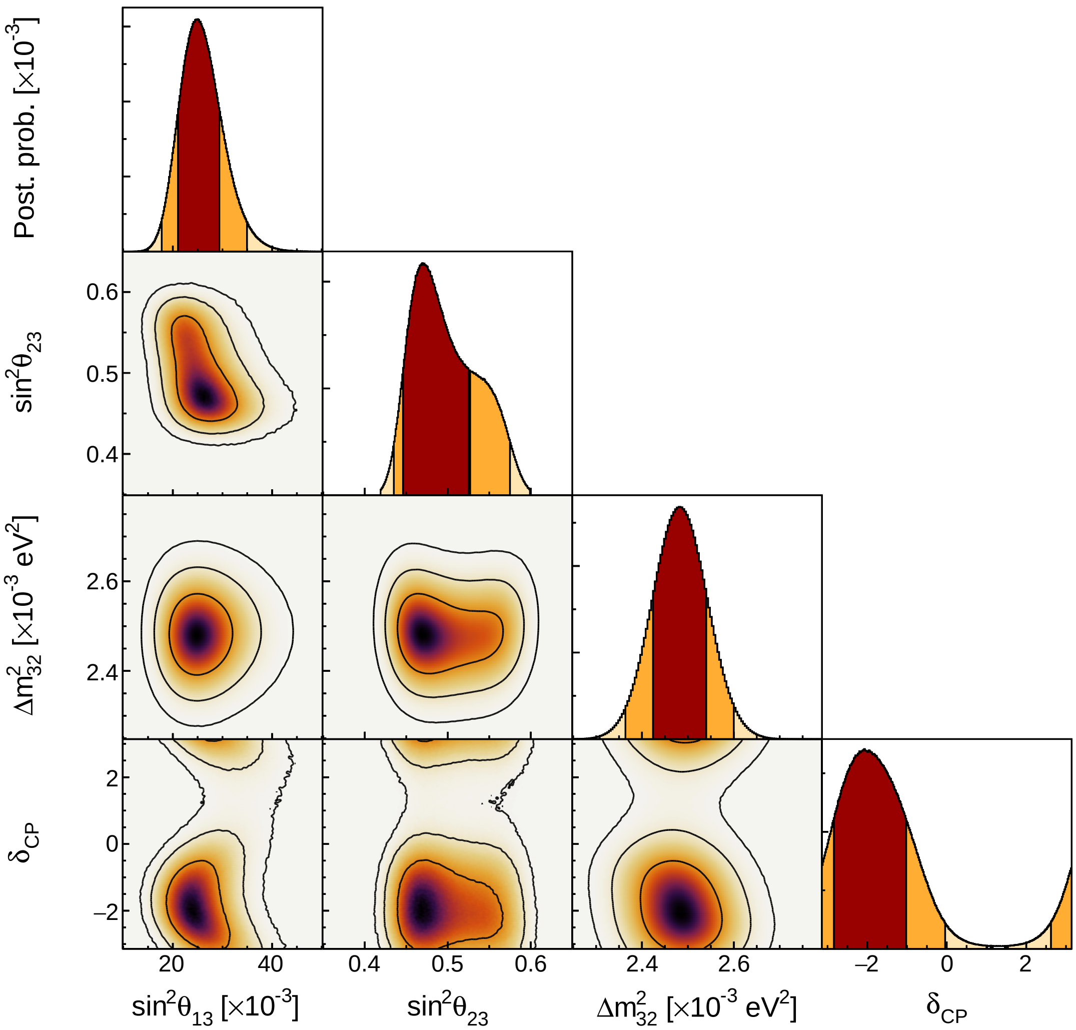

Figure 80: Triangle plots for the real data analysis, without the reactor constraint applied, for the normal ordering, with a flat prior on $\delta_{\rm CP}$. The 1, 2, and 3σ credible intervals are overlaid on the posterior.

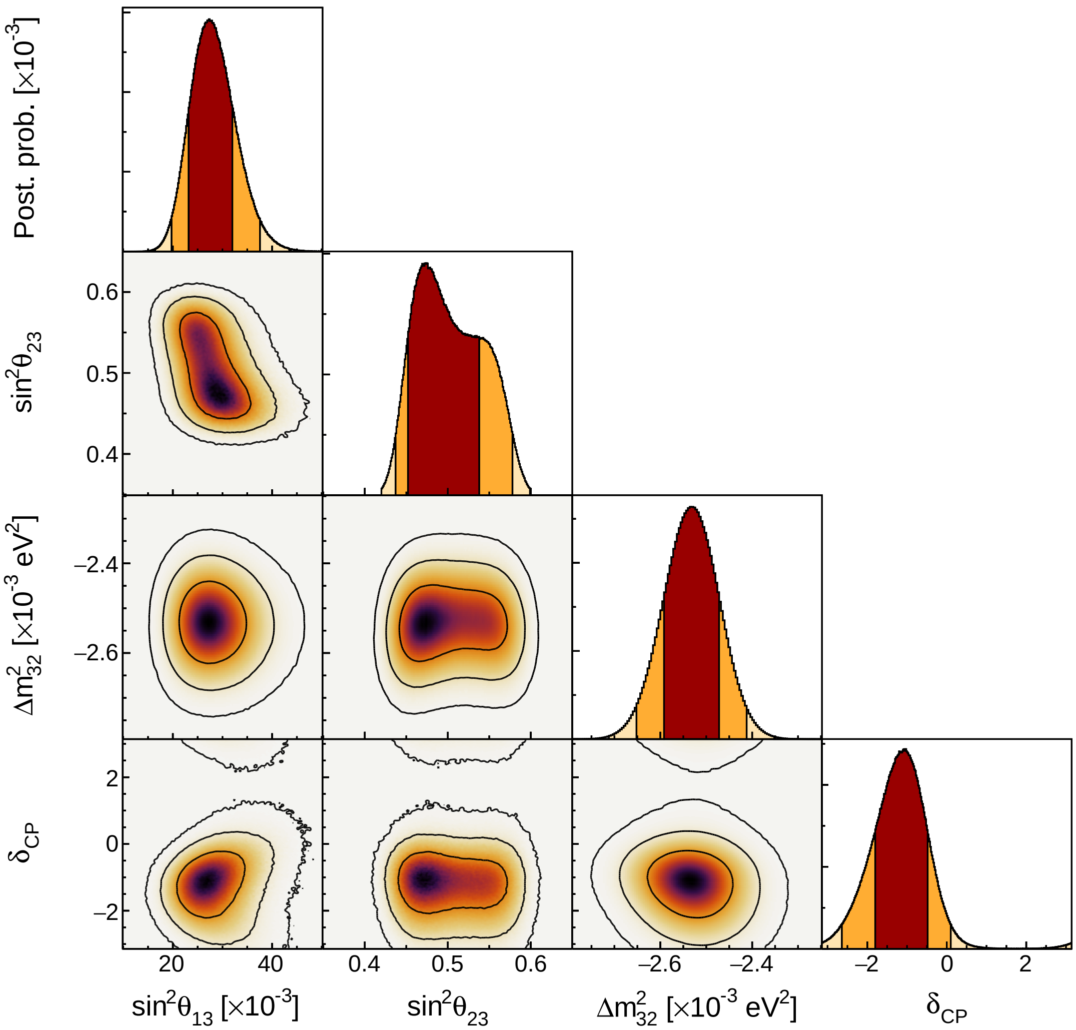

Figure 81: Triangle plots for the real data analysis, without the reactor constraint applied, for the inverted ordering, with a flat prior on δ_{CP}. The 1, 2, and 3σ credible intervals are overlaid on the posterior.

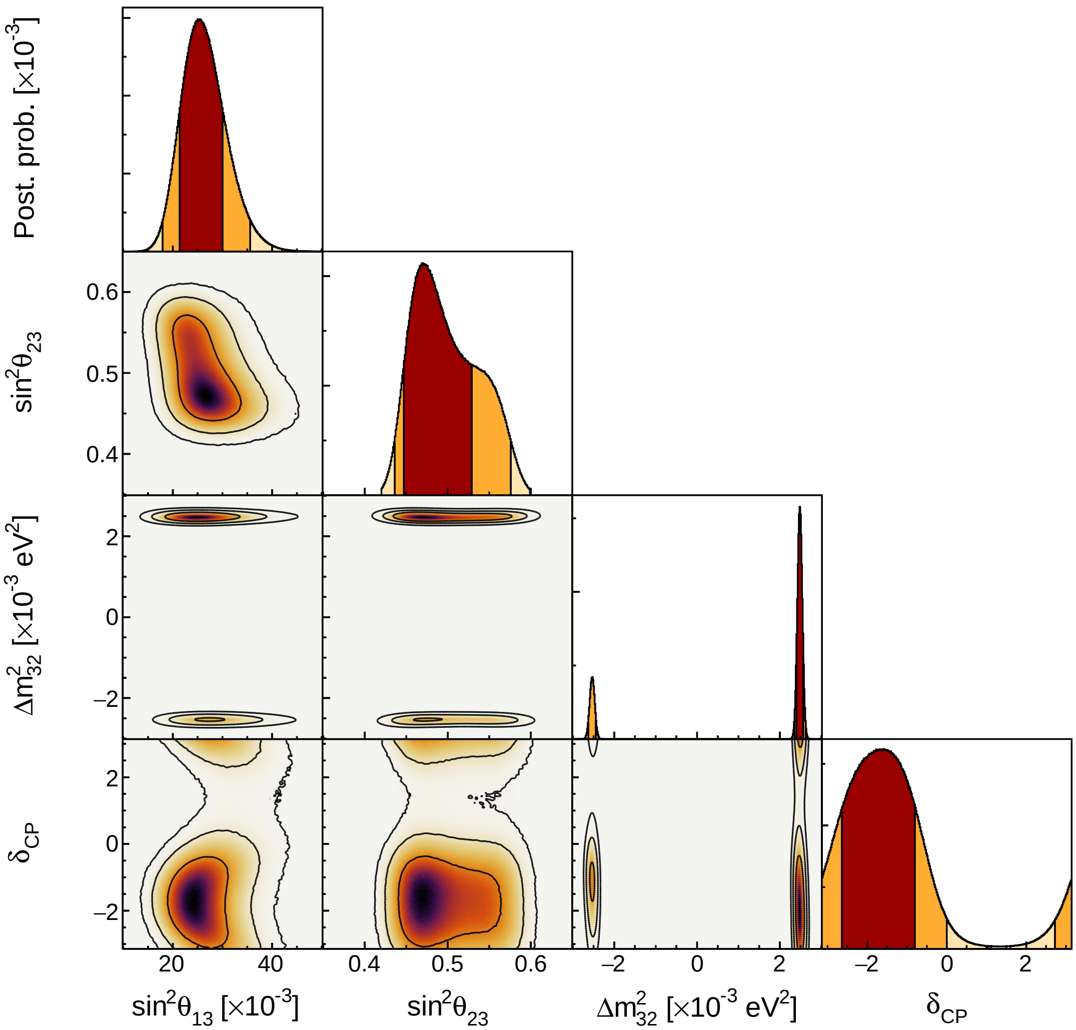

Figure 82: Triangle plots for the real data analysis, without the reactor constraint applied, for both mass orderings, with a flat prior on δ_{CP}. The 1, 2, and 3σ credible intervals are overlaid on the posterior.

4.2.3 Bayes factors for atmospheric parameters

Posterior probabilities for the data fit without reactor constraint are calculated and summarized in Tab. 8. The Bayes factor for upper octant over lower octant $B(\mathrm{UO/LO})$ is 0.82, notably weaker than the with reactor constraint case. This is expected due to the correlations between $\sin^2\theta_{23}$ and $\sin^2\theta_{13}$. The Bayes factor for normal ordering over inverted ordering $B(\mathrm{NO/IO})$ is 3.76, which is comparable to T2K's main result using reactor constraint ($B(\mathrm{NO/IO}) = 4.2$). The Bayes factor for upper octant and normal ordering over its competing hypotheses $B([\mathrm{UO{+}NO}]/\mathrm{Other})$ is 0.52.

	$\sin^2\theta_{23} < 0.5$	$\sin^2\theta_{23} > 0.5$	Sum
NO	0.44	0.34	0.79
IO	0.11	0.11	0.21
Sum	0.55	0.45	1.00

Table 8: Posterior probabilities for the mass ordering and the octant in the real data analysis, without the reactor constraint applied.

4.3 Impact of a flat prior on δ_{CP} or $\sin\delta_{\mathrm{CP}}$

This section overlays the one-dimensional posterior probabilities using a prior flat in δ_{CP} (identical to results in Sec. 4) with when applying a prior flat in $\sin\delta_{\mathrm{CP}}$. This section applies the reactor constraint for all results. Fig. 83 shows the posterior probabilities and 1, 2, 3σ credible intervals for the two choices of prior. The 2σ interval just contains $+\pi$ with a prior flat in $\sin\delta_{\mathrm{CP}}$, whereas it excludes it with a prior flat in δ_{CP}. Thus, a statement on 2σ exclusion of $\delta_{\mathrm{CP}} = 0, \pi$ is prior dependent, and should be avoided.

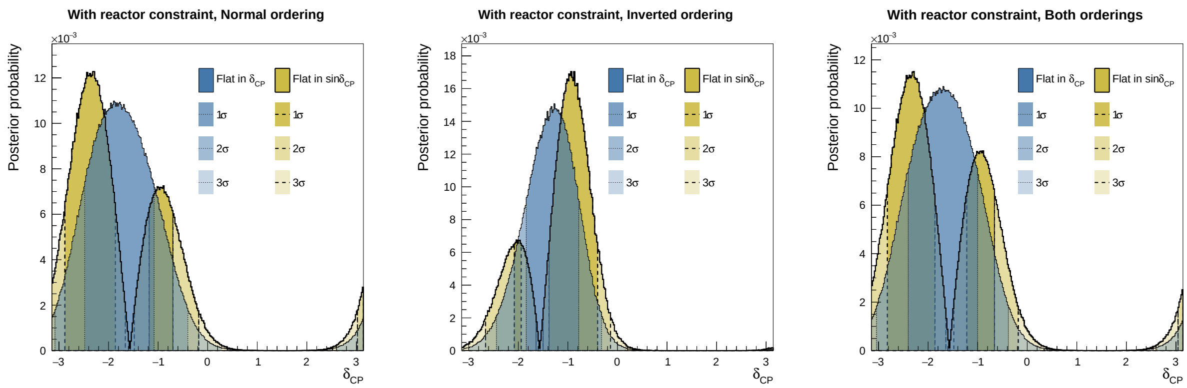

Figure 83: δ_{CP} from real data fit with a prior flat in δ_{CP} (blue shaded) and flat in $\sin\delta_{\mathrm{CP}}$ (yellow shaded) applied.

Fig. 84 shows the same result but for Δm^2_{32}, which has close to no impact on both the credible intervals and the mass ordering preference. This is expected from the weak correlation between Δm^2_{32} and δ_{CP} in Sec. 4.

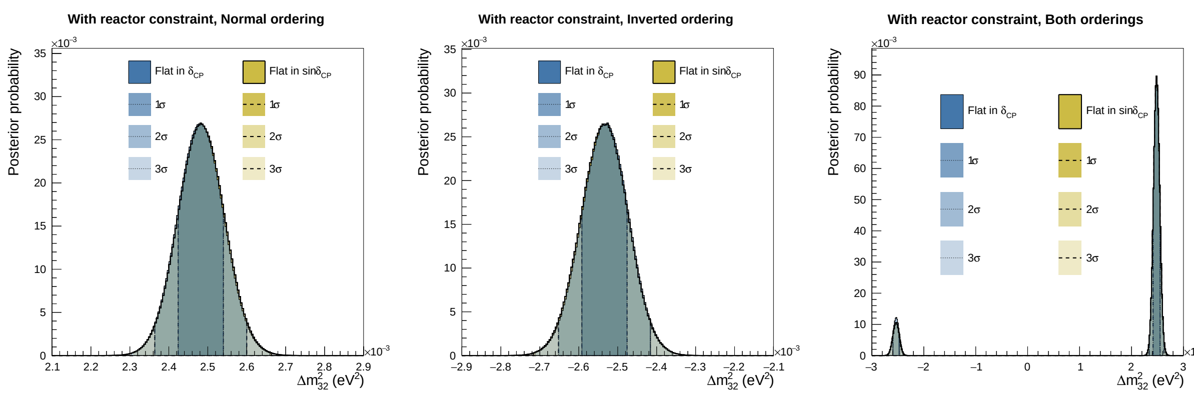

Figure 84: Δm^2_{32} from real data fit with a prior flat in δ_{CP} (blue shaded) and flat in $\sin\delta_{\mathrm{CP}}$ (yellow shaded) applied.

Similarly, the posteriors for $\sin^2\theta_{13}$ in Fig. 85 are identical.

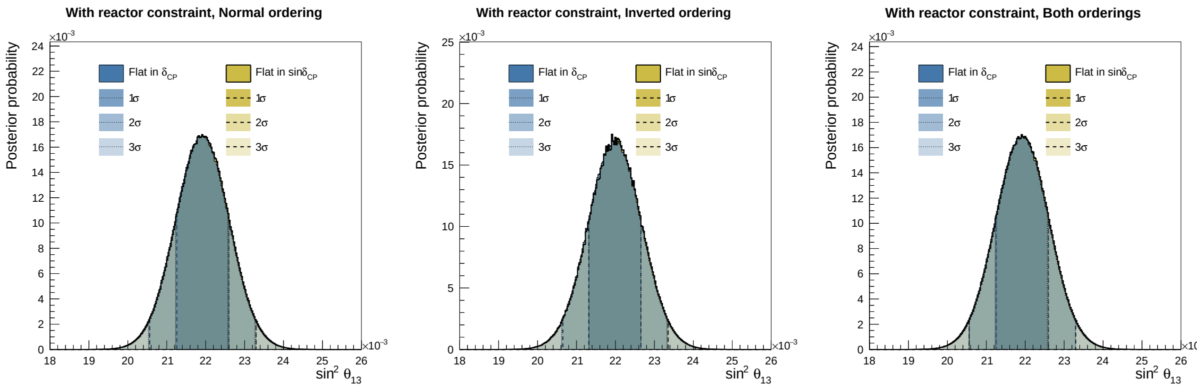

Figure 85: $\sin^2\theta_{13}$ from real data fit with a prior flat in $\delta_{\rm CP}$ (blue shaded) and flat in $\sin\delta_{\rm CP}$ (yellow shaded) applied.

Finally, the $\sin^2\theta_{23}$ is shown in Fig. 86, where there is a marginally stronger preference for the upper octant when a flat prior on $\sin\delta_{\rm CP}$ is used in the normal ordering. For inverted ordering the posterior is largely the same.

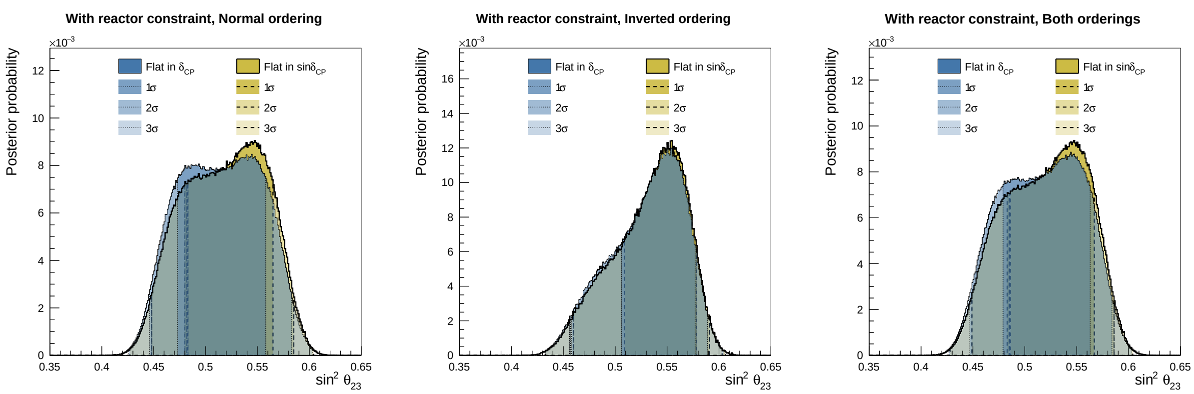

Figure 86: $\sin^2\theta_{23}$ from real data fit with a prior flat in $\delta_{\rm CP}$ (blue shaded) and flat in $\sin\delta_{\rm CP}$ (yellow shaded) applied.

4.4 Impact of reactor constraint

Fig. 87, Fig. 88, Fig. 89 and Fig. 90 are the comparison of one dimensional contours for results with reactor constraint (blue shaded) and without reactor constraint (yellow shaded) of δ_{CP}, $\sin^2\theta_{13}$, $\sin^2\theta_{23}$ and Δm^2_{32} respectively.

In Fig. 87, similar contour shape differences are observed in OA2020 with/without reactor constraint comparison (see Figure 88 in TN393 [1]). For normal ordering and inverted ordering, contours with reactor constraint have better constraint on δ_{CP} and pull the best-fit points slightly away from contours without reactor constraint, but in different directions. Results without reactor constraint can barely exclude $\delta_{\mathrm{CP}} = 0$ at 2σ for normal ordering, but cannot exclude it for inverted ordering. Results with reactor constraint can easily exclude it at 2σ for both orderings.

Fig. 88 shows the direct effect of reactor constraint on $\sin^2\theta_{13}$. The posterior probability is narrowed and is approximately a Gaussian with the central value close to 0.0218.

In Fig. 89, contrarily to the comparison in OA2020 (Fig. 88 in TN393 [1]), the results without reactor constraint show a preference of the lower octant while the results with reactor constraint show a much weaker preference of one octant over another, highlighting the impact of the SK atmospheric selections.

Fig. 90 shows that the constraint on Δm^2_{32} is largely independent of the reactor constraint on $\sin^2\theta_{13}$.

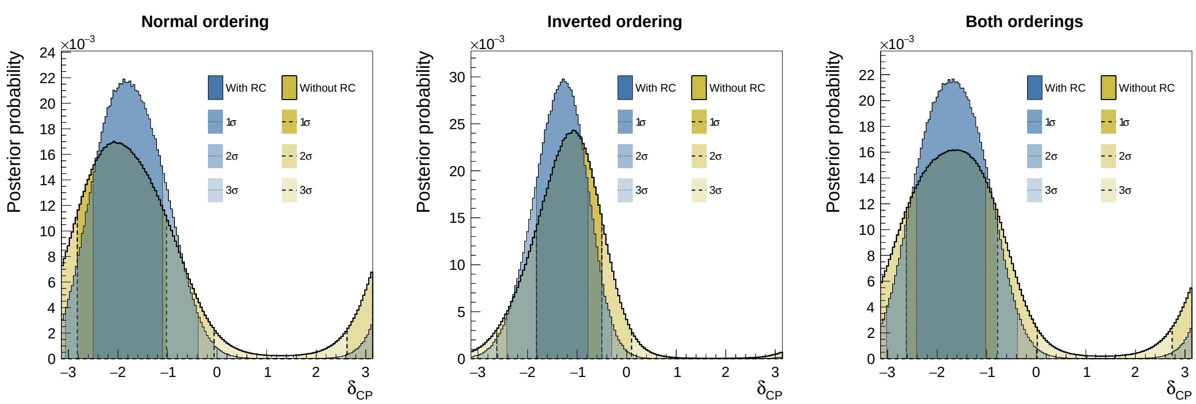

Figure 87: δ_{CP} from real data fit with (blue shaded) and without (yellow shaded) reactor constraint applied, for normal (left), inverted (center) and both (right) orderings.

Bayes factors Tab. 9 summarises the posterior probabilities of $\sin\delta_{\mathrm{CP}} \geq 0$ and $\sin\delta_{\mathrm{CP}} < 0$ without and with reactor constraint, respectively. The Bayes factor of $\sin\delta_{\mathrm{CP}} < 0$ over $\sin\delta_{\mathrm{CP}} \geq 0$ is 10.5 without reactor constraint and 50.0 with reactor constraint.

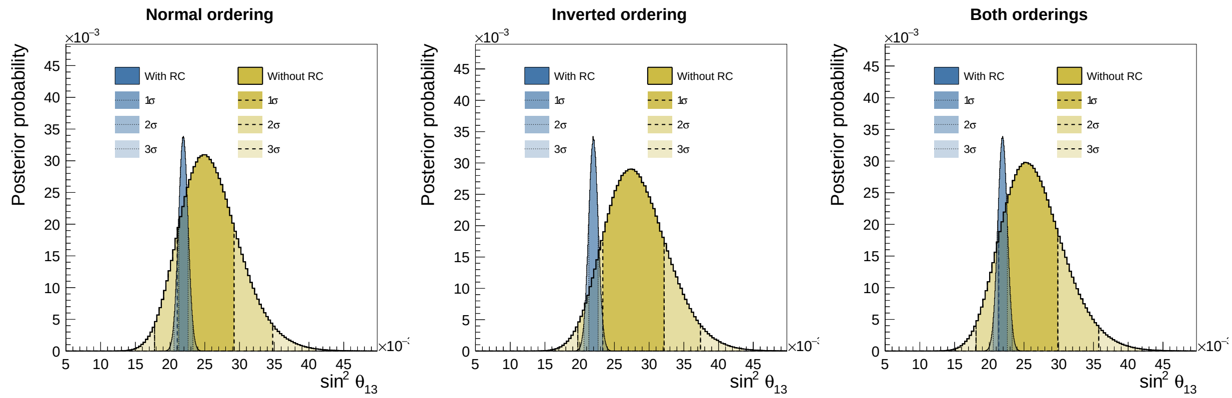

Figure 88: $\sin^2\theta_{13}$ from real data fit with (blue shaded) and without (yellow shaded) reactor constraint applied, for normal (left), inverted (center) and both (right) orderings.

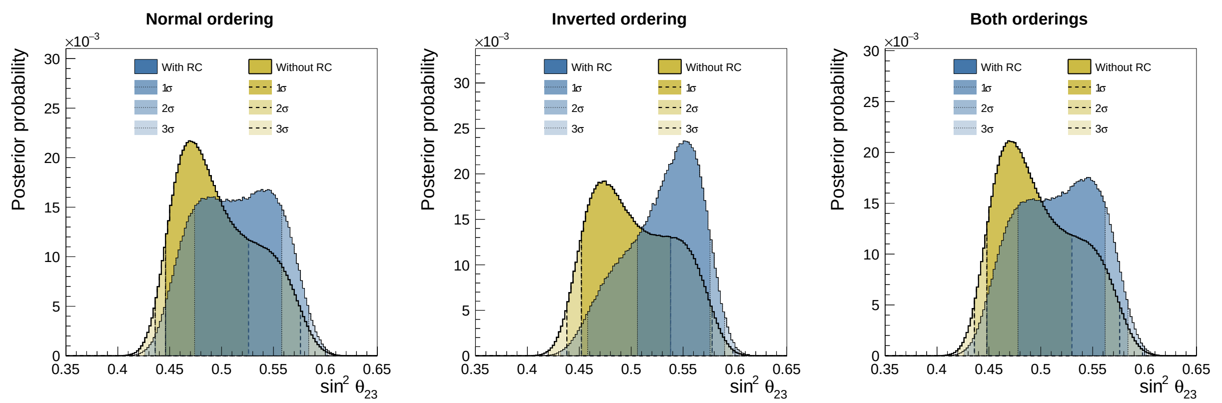

Figure 89: $\sin^2\theta_{23}$ from real data fit with (blue shaded) and without (yellow shaded) reactor constraint applied, for normal (left), inverted (center) and both (right) orderings.

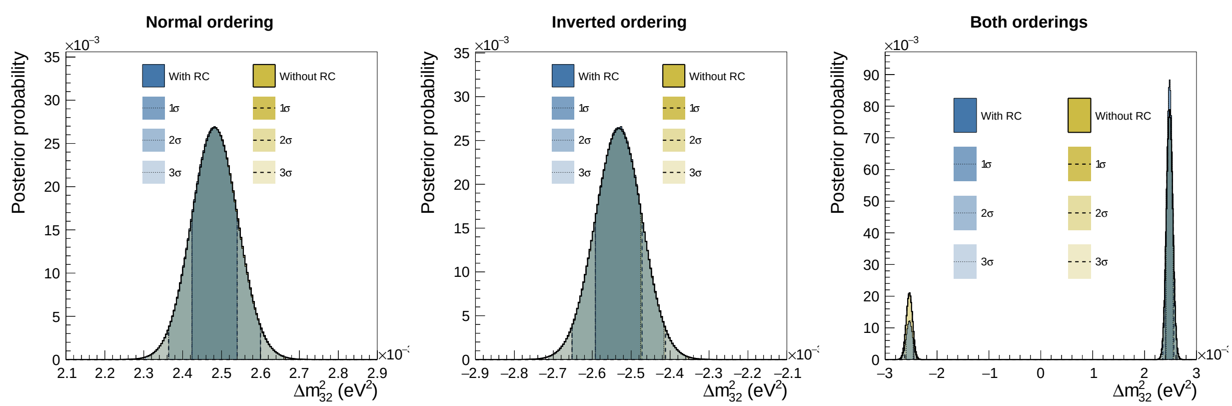

Figure 90: Δm^2_{32} from real data fit with (blue shaded) and without (yellow shaded) reactor constraint applied, for normal (left), inverted (center) and both (right) orderings.

	$\sin\delta_{\mathrm{CP}} \geq 0$	$\sin\delta_{\mathrm{CP}} < 0$	Sum
No RC	0.086	0.914	1.000
RC	0.019	0.981	1.000

Table 9: Posterior probabilities for data analysis with and without reactor constraint

Tab. 10 summarises the Bayes factors of upper octant over lower octant, and normal ordering over inverted ordering for results with and without reactor constraint. The result with the reactor constraint has a slightly stronger preference of the upper octant. For the mass ordering, results with reactor constraint has a stronger preference of normal ordering.

	B(UO/LO)	B(NO/IO)
No RC	0.82	3.76
RC	1.78	7.33

Table 10: Summary table of the Bayes factors of upper octant over lower octant and normal ordering over inverted ordering for data fit results with reactor constraint and without reactor constraint.

4.5 Posterior Predictive Spectra and p-values

4.5.1 Posterior predictive spectra

Posterior predictive spectra are constructed by randomly selecting 3000 throws from the post burn-in steps in the data fit. The mean of each reconstructed kinematic bin is calculated with the RMS of the 3000 throws distribution representing the uncertainty. The data (black markers) are also shown in the same plot. The posterior predictive spectra are shown with (blue markers) and without (red markers) reactor constraint. The posterior predictive spectra with reactor constraint are obtained by applying the reactor constraint weights to each throw.

To focus on the region where the oscillations occur, the spectra of T2K mu-like beam samples (Fig. 91) binned in reconstructed energy are only shown below 2 GeV, even though higher E_{rec} bins are included in the overall analysis. The e-like T2K samples are bined in both reconstructed neutrino energy and lepton angle, and the projections on the lepton angle are shown in Fig. 92.

Fig. 93, Fig. 95 and Fig. 97 are spectra binned in reconstructed lepton momentum for atmospheric SubGeV, MultiGeV and PC&UpMu samples respectively. Though UpMu-nonshower and UpMu-shower samples only have one bin in reconstructed lepton momentum, the overlay plots are shown. Fig. 94, Fig. 96 and Fig. 98 are the spectra binned in reconstructed cosine zenith angle for atmospheric SubGeV, MultiGeV and PC&UpMu samples respectively. Though SubGeV1Re1dcy, SubGeV1Rmu2dcy and SubGeV2Rpi0 samples only have one bin in reconstructed lepton angle, the overlay plots are shown.

4.5.2 Impact of uncertainty sources

Tab. 11 summarises different groups of systematics uncertainty contributions to the total uncertainty for each SK sample without the reactor constraint applied. The uncertainty is calculated as the change in the total number of events in the sample using to the post-fit constraints on the systematics. The uncertainty on each group is calculated by randomly drawing 3000 throws of systematics and using them to produce sample spectra from post burn-in MCMC chains while keeping the other groups fixed at nominal (AsimovA). When extracting a specific group of systematics contribution, other groups are fixed at their nominal values. Hence, the correlation between groups are not considered and thus, the total uncertainty is not naively a sum of different groups in quadrature. The total systematic uncertainties (labelled as "Total Syst.") are extracted by varying all systematics including near-detector systematics and fixing all oscillation parameters to their Asimov A values. The total uncertainties (labelled as "Total") are extracted by varying all systematics including near-detector systematics and oscillation parameters.

We see that for the T2K samples the cross-section uncertainties and detector uncertainties play the largest role, and are the largest for the FHC 1Re1de and RHC 1Re samples (7%, 4%, respectively). The uncertainties are largely the same as in T2K's analysis, with the exception of the total uncertainty on the FHC 1Re1de, which is 9.2% compared to $\sim 14\%$ on T2K, likely due to correlations in the systematics with the atmospheric selections. For the SK atmospheric samples, the atmospheric flux uncertaintes are $\sim 3\%$ for the SubGeV samples, which is similar to the impact of the other classes of systematics. As for T2K, the e-like SK samples often have large cross-section systematics than the mu-like equivalents. For the higher energy samples, the uncertainty increases to $\sim 4-6\%$ and the detector systematics are the smallest source of uncertainty. Interestingly, the overall uncertainty on the SK atmospheric samples is smaller than for the T2K samples.

The uncertainty from all sources ("Total") may be less than "Total syst" due to correlations between oscillation parameters and systematic parameters, which are not accounted for when only calculating the "Total syst". These correlations can lessen the overall uncertainty on the number of events at SK.

4.5.3 Posterior predictive p-values

Two p-values are calculated to quantify the agreement between the model and the data. One is calculated using a χ^2 based on total event rate for each sample (single bin analysis) and the other is calculated based on the shape (i.e. bin-by-bin) for each sample. We repeat these studies with and without applying the reactor constraint on $\sin^2\theta_{13}$.

The p-value calculation is based on making random draws of all the parameters (systematics and oscillation parameters) from the chain after burn in, and building the prediction of the samples for this specific draw. The χ^2 between the draw and the data is calculated, and compared to the χ^2 between the draw and a statistical fluctuation of the draw. The p-value is extracted as the percentage of draws for which the $\chi^2(\text{data, draw}) < \chi^2(\text{fluct. draw, draw})$. The p-value calculation compares the expected χ^2 for a given draw ($\chi^2(\text{fluct. draw, draw})$) against the actual realised χ^2 for the data and the given draw ($\chi^2(\text{data, draw})$). If the model is insufficiently parametrised, the $\chi^2(\text{data, draw})$ is expected to be much larger than $\chi^2(\text{fluct. draw, draw})$. If the model is sufficient, you'd expect $\chi^2(\text{data, draw})$ to be similarly sized to $\chi^2(\text{fluct. draw, draw})$. Finally, in the case where we have an over-parametrised model with too much freedom, we expect $\chi^2(\text{data, draw})$ to be much smaller than $\chi^2(\text{fluct. draw, draw})$. Hence, a p-value close to 1 is not necessarily a good thing with posterior predictive p-values, and should also be investigated.

The p-values are investigated in details in Tab. 12. First, we look at the p-value from both the total event rate and the shape of the spectrum. For the shape of the spectrum, we project the T2K samples onto the reconstructed neutrino energy E_{rec} and the SK samples on the reconstructed lepton momentum, p_{lep}, except for the UpThru samples, which are only binned in $\cos\theta_z$. Secondly, we also restrict the shape p-value to the region relevant to neutrino oscillations, that is $E_{\text{rec}} < 2$ GeV for the T2K samples and $p_{\text{lep}} < 10$ GeV/c for the SK samples. Thirdly, we also investigate the impact of the reactor constraint on $\sin^2\theta_{13}$.

The overall rate-only p-value is 0.387 without reactor constraint, and 0.420 with the reactor constraint. For the rate-only p-value, we note the T2K FHC 1Rmu (0.195) and SK MultiGeV-elike-nue (0.220) fall below $p = 0.25$. As previously noted, these are relatively strong p-values, and we conclude the rate for all samples to be well described. The reactor constraint has the largest impact on the T2K RHC 1Re sample ($0.475 \rightarrow 0.673$), T2K FHC 1Re1de ($0.444 \rightarrow 0.351$). As expected, the reactor constraint has a much smaller effect on SK samples.

The overall shape p-value falls to 0.106 (0.111) when (not) applying the reactor constraint. The shape p-value does a better job at exposing weaknesses in modelling the samples. The T2K FHC 1Rmu (0.240), T2K FHC 1Re (0.209), SK SubGeV-mulike-1dcy (0.162), SK SubGeV-pi0like (0.162), SK MultiGeV-elike-nuebar (0.207), SK MultiRingOther-1 (0.063), and SK UpThruNonShower-mu (0.03) samples fall below $p = 0.25$, with the latter two samples being particularly bad.

Breaking up the total shape p-value into the T2K and SK part, the former has $p = 0.471$ and latter has $p = 0.039$. Splitting the SK p-values into SubGeV and MultiGeV+MultiRing, the former has $p = 0.251$ and the latter has $p = 0.037$ when imposing the 10 GeV/c cut, and $p = 0.001$ when looking at the entire p_{lep} phase space. Hence, the poor shape p-value comes primarily from the MultiGeV and MultiRing samples. For the two set of samples that share systematics, the T2K and SK SubGeV, the p-values are good for both the event-rate (0.536) and shape (0.365), indicating that the correlated uncertainty model is robust in describing both set of samples.

Fig. 99 complements Tab. 12 by showing the distributions which determine the rate and shape-based p-values. We see that the underlying distribution is more circular for the rate-based p-value (implying there is roughly the equal spread in uncertainty from systematics as there are from statistics if the data is similar to the model), whereas the shape-based p-value is more oblong.

To illustrate the by-sample p-values, the same underlying distributions are shown by sample in Fig. 100 for SK atmospheric and Fig. 101 for T2K beam samples. We note that for T2K samples the distributions are more horizontal, which comes from the low statistics making the χ^2 from a statistical variation large. The relative contributions to the χ^2 from the samples can also be seen, where the χ^2 from the SK Sub-GeV samples is often below 10, whereas for T2K they are often above 20.

To further investigate the poor shape-based posterior predictive p-values of the multi-GeV and multi-ring samples at SK, we instead project the selections on the reconstructed zenith angle, $\cos\theta_z$, in Tab. 13. For these calculations, we keep the T2K samples projected onto the reconstructed neutrino energy E_{rec} and the SK SubGeV samples projected onto the reconstructed lepton momentum p_{lep}. The overall total p-value markedly improves from $p = 0.111$ to $p = 0.322$, although by-sample the change is more nuanced. The SK MultiGeV-elike-nue selection goes from relatively well described to acceptable ($p = 0.313 \to 0.098$) and the SK PCStop selection goes from 0.682 to 0.360. However, the MultiRingOther-1, which was poorly described in p_{Lep}, is now well described in $\cos\theta_z$ with $p = 0.755$. Finally, the p-value from MultiGeV and MultiRing selections, which was $p = 0.037$ in p_{lep}, improves to $p = 0.398$ in $\cos\theta_z$.

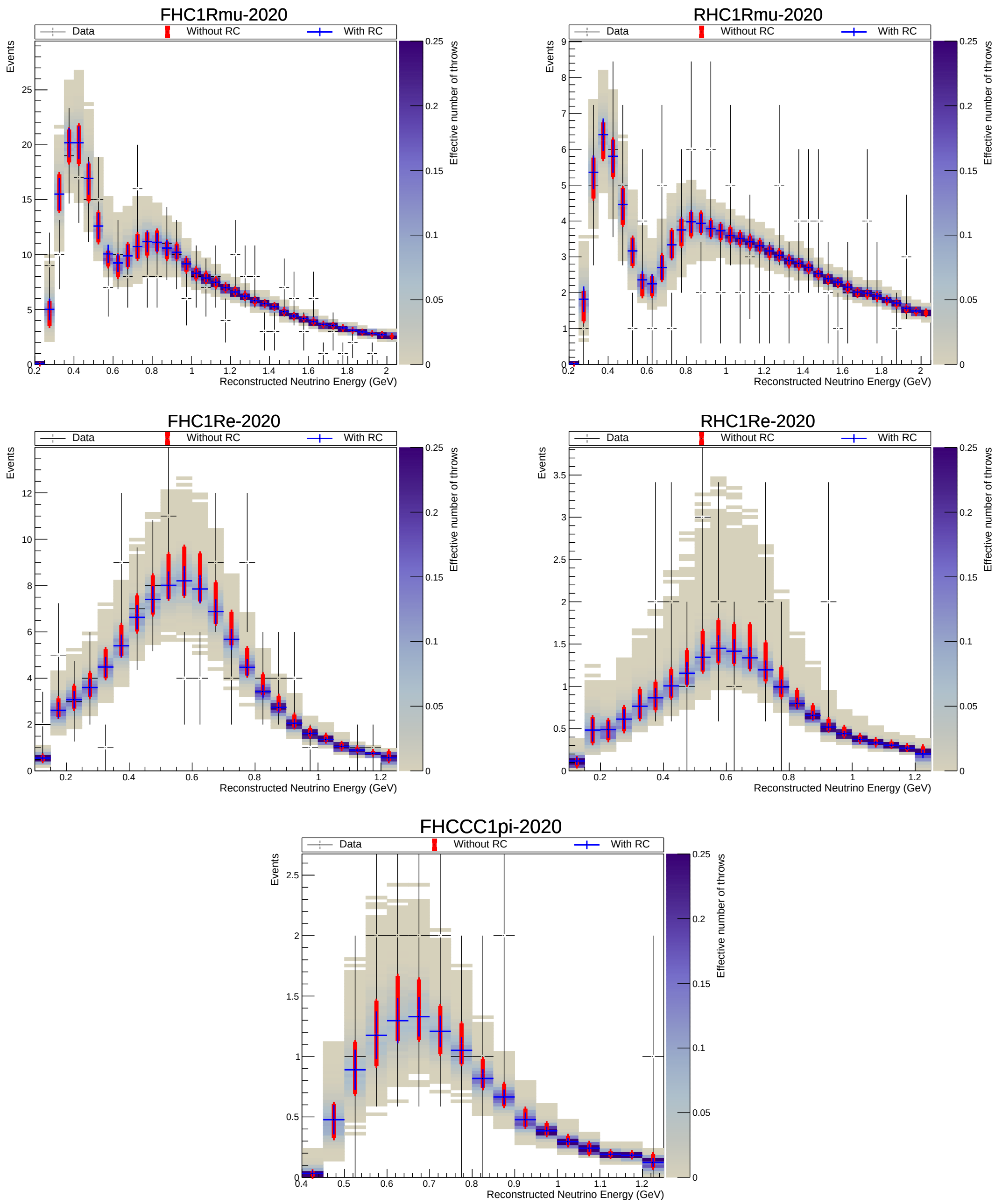

Figure 91: Posterior predictive spectra from the data fit for the T2K beam samples, binned in reconstructed energy. Spectra with (blue) and without (red) reactor constraint are shown.

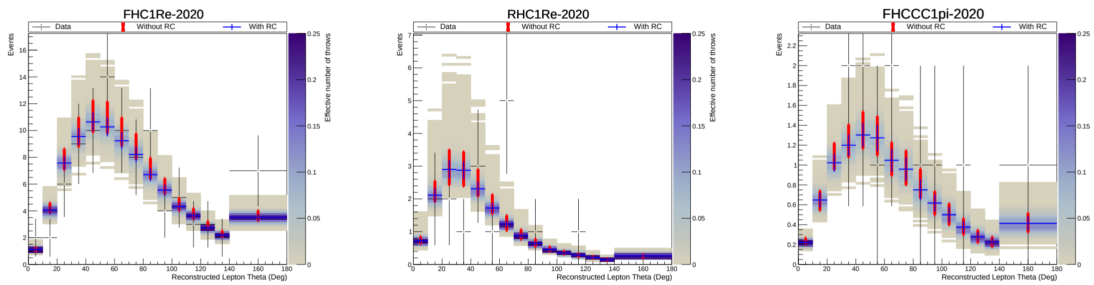

Figure 92: Posterior predictive spectra from the data fit for the T2K e-like beam samples, binned in reconstructed theta angle. Spectra with (blue) and without (red) reactor constraint are shown.

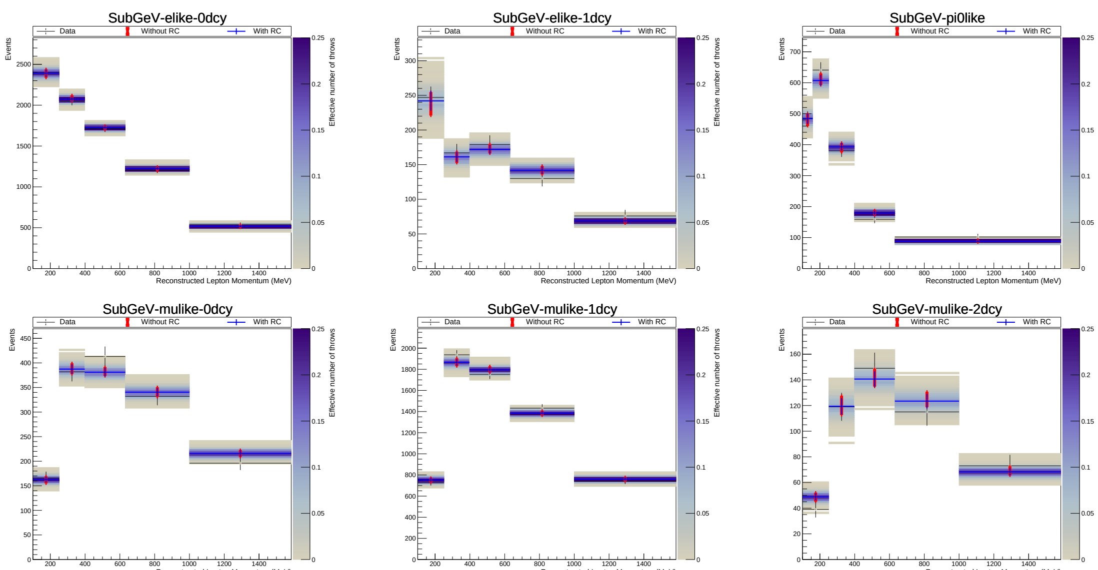

Figure 93: Posterior predictive spectra from the data fit for the SK SubGeV atmospheric samples binned in reconstructed lepton momentum. Spectra with (blue) and without (red) reactor constraint are shown.

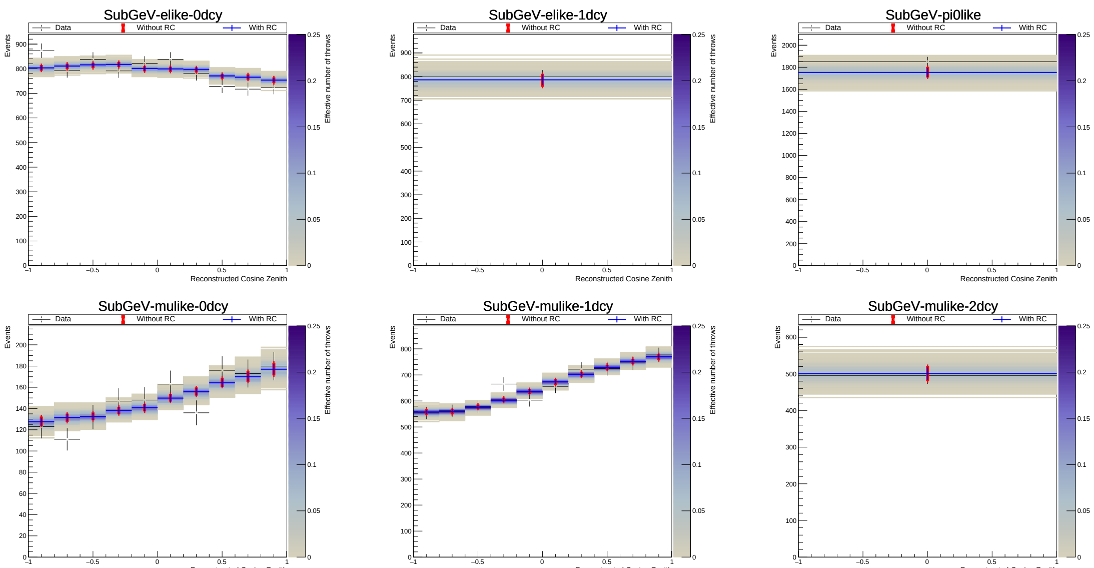

Figure 94: Posterior predictive spectra from the data fit for the SK SubGeV atmospheric samples binned in reconstructed cosine zenith angle. Spectra with (blue) and without (red) reactor constraint are shown.

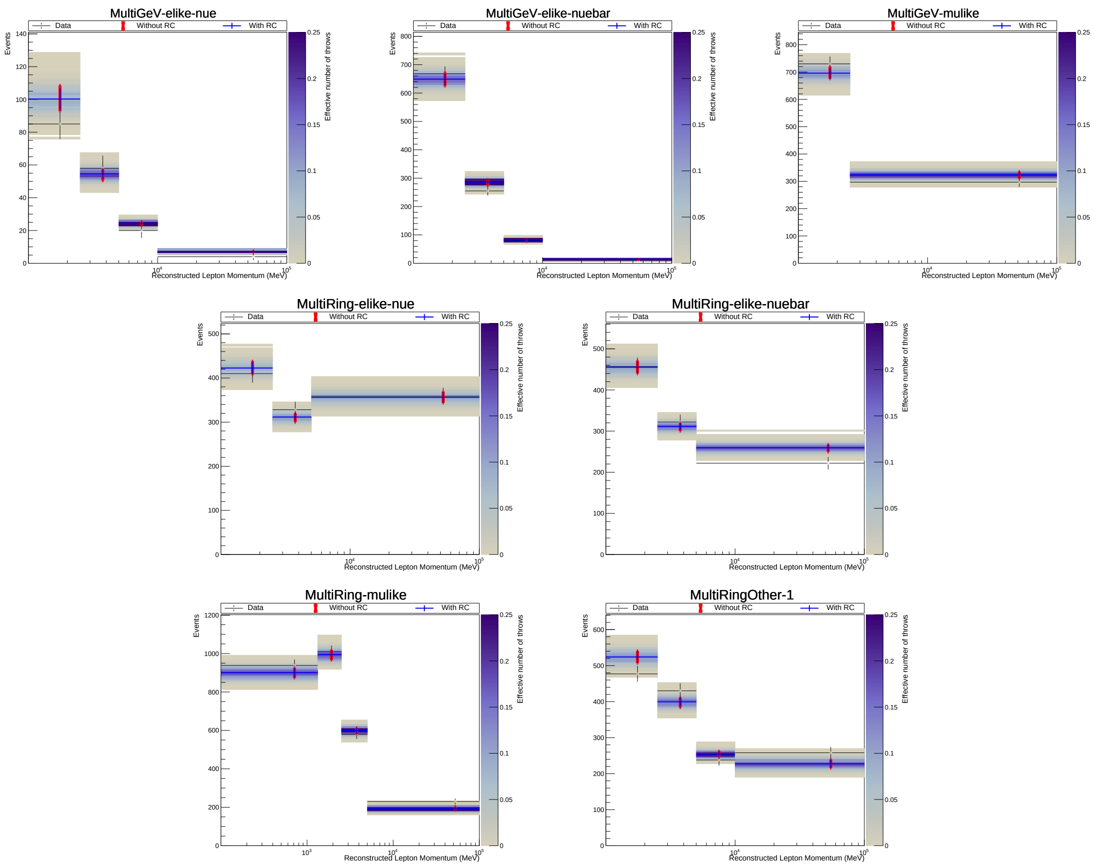

Figure 95: Posterior predictive spectra from the data fit for the SK MultiGeV atmospheric samples binned in reconstructed lepton momentum. Spectra with (blue) and without (red) reactor constraint are shown.

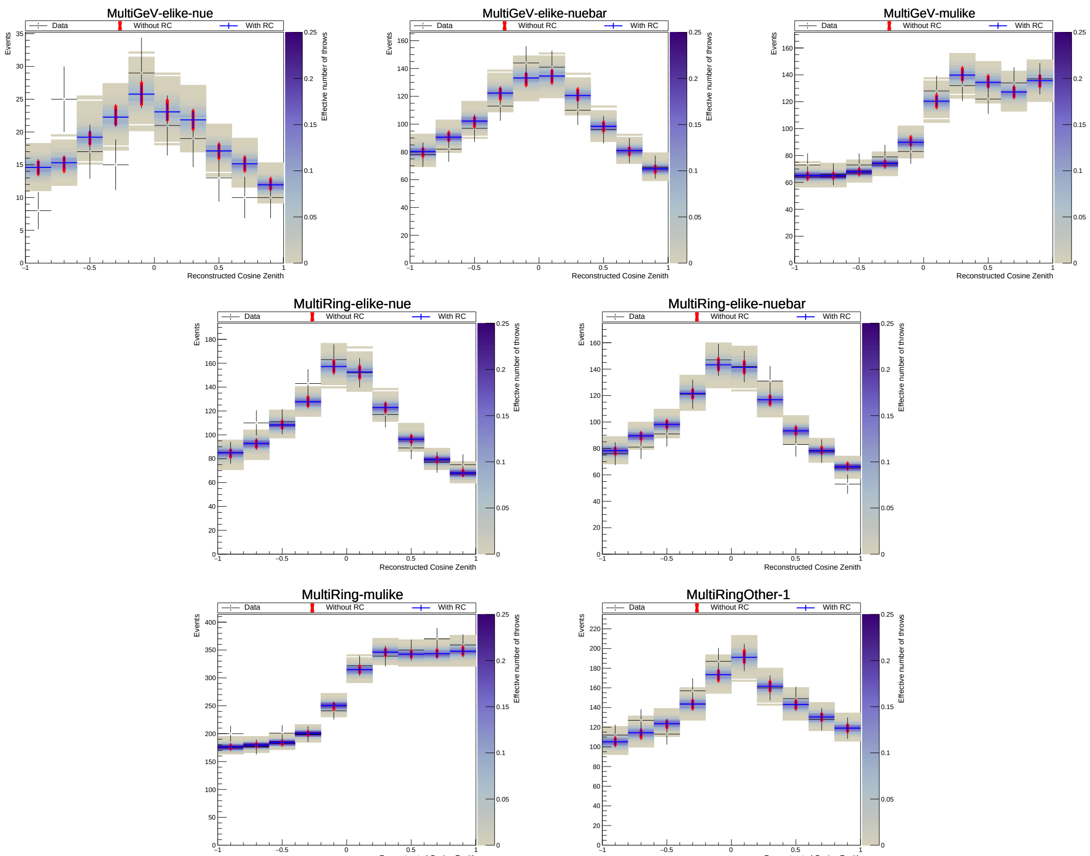

Figure 96: Posterior predictive spectra from the data fit for the SK MultiGeV atmospheric samples binned in reconstructed cosine zenith angle. Spectra with (blue) and without (red) reactor constraint are shown.

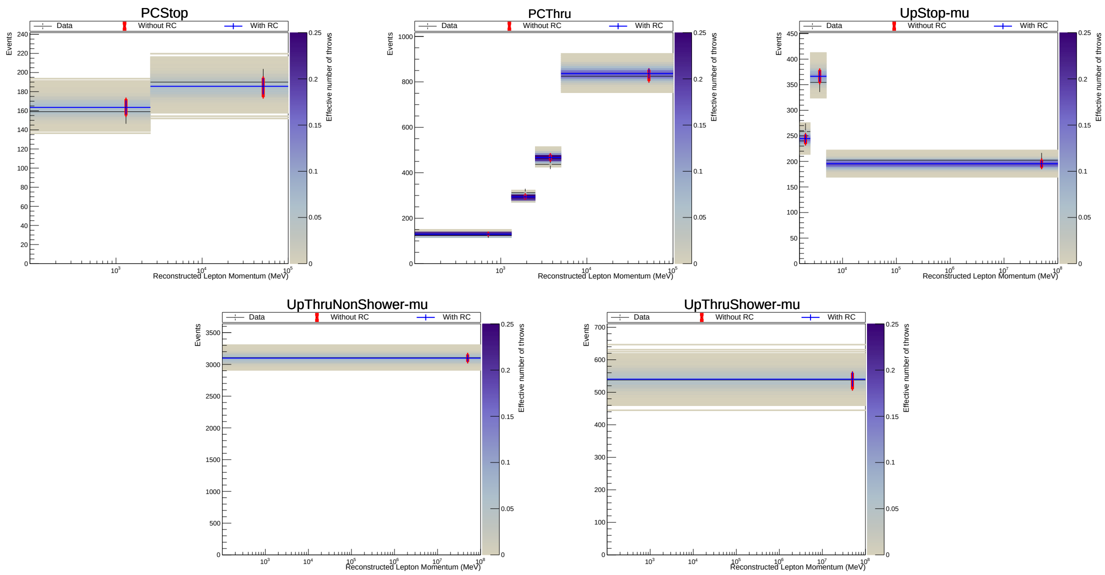

Figure 97: Posterior predictive spectra from the data fit for the SK PC (partically-contained) and UpMu atmospheric samples binned in reconstructed lepton momentum. Spectra with (blue) and without (red) reactor constraint are shown.

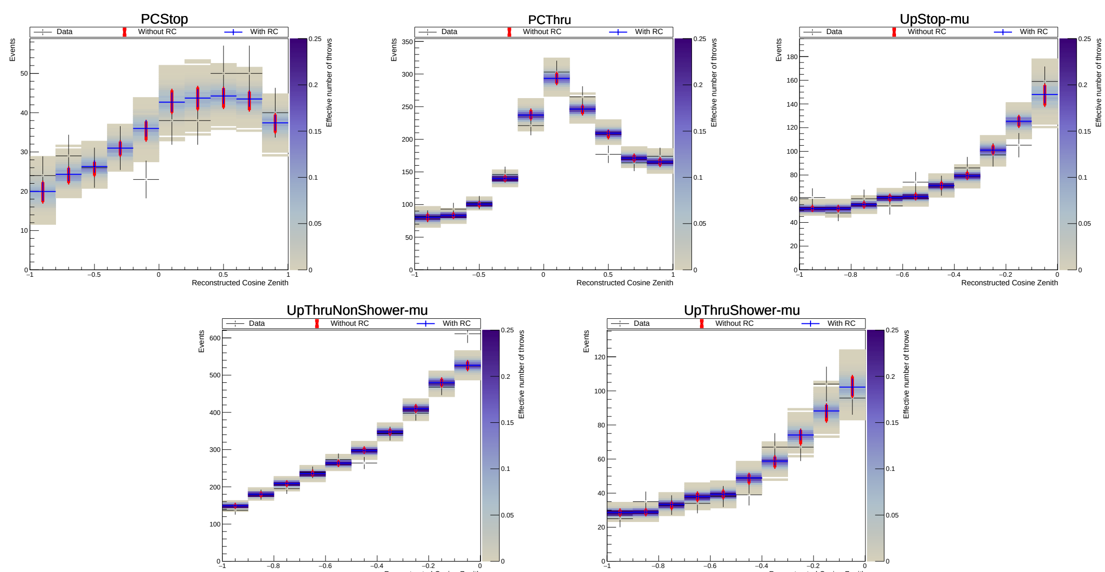

Figure 98: Posterior predictive spectra from the data fit for the SK PC (partically-contained) and UpMu atmospheric samples binned in reconstructed cosine zenith angle. Spectra with (blue) and without (red) reactor constraint are shown.

Sample	SK atm. flux	T2K beam flux	SK det.	Cross sections	Total Syst.	Total
T2K FHC 1Rmu	0.00%	2.54%	2.39%	2.65%	2.81%	3.13%
T2K RHC 1Rmu	0.00%	2.64%	2.28%	3.58%	3.69%	3.80%
T2K FHC 1Re	0.00%	2.55%	2.69%	3.95%	3.99%	8.87%
T2K RHC 1Re	0.00%	2.72%	4.35%	4.37%	6.35%	14.75%
T2K FHC 1Re1de	0.00%	2.53%	7.87%	6.37%	9.21%	12.14%
SK SubGeV-elike-0dcy	3.53%	0.00%	2.55%	3.47%	1.42%	1.07%
SK SubGeV-elike-1dcy	3.00%	0.00%	3.39%	4.38%	3.03%	2.77%
SK SubGeV-mulike-0dcy	3.02%	0.00%	3.19%	2.72%	2.29%	2.16%
SK SubGeV-mulike-1dcy	3.08%	0.00%	2.58%	2.70%	1.28%	1.13%
SK SubGeV-mulike-2dcy	3.01%	0.00%	2.72%	4.34%	3.32%	3.28%
SK SubGeV-pi0like	2.72%	0.00%	2.39%	3.61%	2.32%	2.34%
SK MultiGeV-elike-nue	4.43%	0.00%	3.26%	7.09%	5.49%	5.61%
SK MultiGeV-elike-nuebar	4.23%	0.00%	3.21%	4.43%	2.97%	2.87%
SK MultiGeV-mulike	4.20%	0.00%	2.73%	4.23%	2.87%	2.90%
SK MultiRing-elike-nue	4.30%	0.00%	3.18%	4.26%	2.76%	2.73%
SK MultiRing-elike-nuebar	4.22%	0.00%	3.37%	4.24%	2.73%	2.63%
SK MultiRing-mulike	4.22%	0.00%	2.28%	4.12%	1.76%	1.75%
SK MultiRingOther-1	4.15%	0.00%	3.84%	5.03%	2.61%	2.56%
SK PCStop	4.37%	0.00%	4.80%	3.61%	4.45%	4.50%
SK PCThru	3.17%	0.00%	2.24%	3.82%	2.09%	2.09%
SK UpStop-mu	4.51%	0.00%	2.00%	3.77%	2.92%	2.99%
SK UpThruNonShower-mu	4.33%	0.00%	1.66%	3.90%	1.80%	1.76%
SK UpThruShower-mu	5.78%	0.00%	5.16%	3.72%	4.19%	4.22%

Table 11: Table of different groups of systematics uncertainty contributions to the joint analysis. The uncertainty is calculated as the change in the total number of events in the sample using to the post-fit constraints on the systematics. “SK atm. flux” refers to the group of atmospheric flux systematics. “T2K beam flux” refers to the group of T2K beam flux systematics. “SK det.” refers to the group of correlated far detector systematics. Note that the two newly developed systematics associated with e/μ PID at low pion momentum region are included in “SK det.”. “Cross sections” refers to the group of cross-section systematics, including the new ad-hoc Adler angle parameter. “Total Syst.” refers to the total error values calculated by varying all the systematics including near-detector systematics and fixing the oscillation parameters at Asimov A. “Total” refers to the total error values calculated by varying all the systematics, including near-detector systematics, and oscillation parameters. All the uncertainties are calculated from using the standard deviations of the posterior predictive distributions. No reactor constraint is applied.

Sample	woRC rate	woRC shape	wRC rate	wRC shape
T2K FHC 1Rmu	0.195	0.240	0.191	0.241
T2K RHC 1Rmu	0.725	0.643	0.742	0.640
T2K FHC 1Re	0.515	0.209	0.498	0.222
T2K RHC 1Re	0.475	0.625	0.673	0.658
T2K FHC 1Re1de	0.444	0.912	0.351	0.902
SK SubGeV-elike-0dcy	0.491	0.574	0.492	0.580
SK SubGeV-elike-1dcy	0.500	0.553	0.533	0.571
SK SubGeV-mulike-0dcy	0.559	0.356	0.559	0.338
SK SubGeV-mulike-1dcy	0.499	0.162	0.490	0.159
SK SubGeV-mulike-2dcy	0.559	0.491	0.591	0.486
SK SubGeV-pi0like	0.481	0.162	0.482	0.162
SK MultiGeV-elike-nue	0.220	0.313	0.236	0.314
SK MultiGeV-elike-nuebar	0.454	0.207	0.431	0.201
SK MultiGeV-mulike	0.512	0.271	0.550	0.308
SK MultiRing-elike-nue	0.518	0.400	0.526	0.407
SK MultiRing-elike-nuebar	0.422	0.657	0.431	0.641
SK MultiRing-mulike	0.276	0.389	0.255	0.415
SK MultiRingOther-1	0.518	0.063	0.495	0.047
SK PCStop	0.545	0.682	0.554	0.689
SK PCThru	0.462	0.378	0.452	0.369
SK UpStop-mu	0.544	0.564	0.537	0.569
SK UpThruNonShower-mu	0.513	0.030	0.530	0.026
SK UpThruShower-mu	0.508	0.429	0.515	0.423
Total	0.387	0.111	0.420	0.106
T2K only	0.465	0.471	0.491	0.505
SK only	0.384	0.039	0.414	0.036
SK SubGeV only	0.569	0.251	0.591	0.251
T2K+SK SubGeV only	0.536	0.365	0.569	0.384
SK Multi-GeV/Ring, rest.	0.334	0.037	0.355	0.059
SK Multi-GeV/Ring, full	0.321	0.001	0.328	0.000

Table 12: Table of different p-values from the data fit broken down in to each SK sample. The χ^2 calculation is based on both total event rate and shape, and the impact of the reactor constraint is shown ("wRC" being with reactor constraint, and "woRC" being without reactor constraint). A kinematic cut of $E_{\mathrm{rec}} < 2$ GeV is applied for T2K samples and $p_{\mathrm{lep}} < 10$ GeV/c for SK samples.

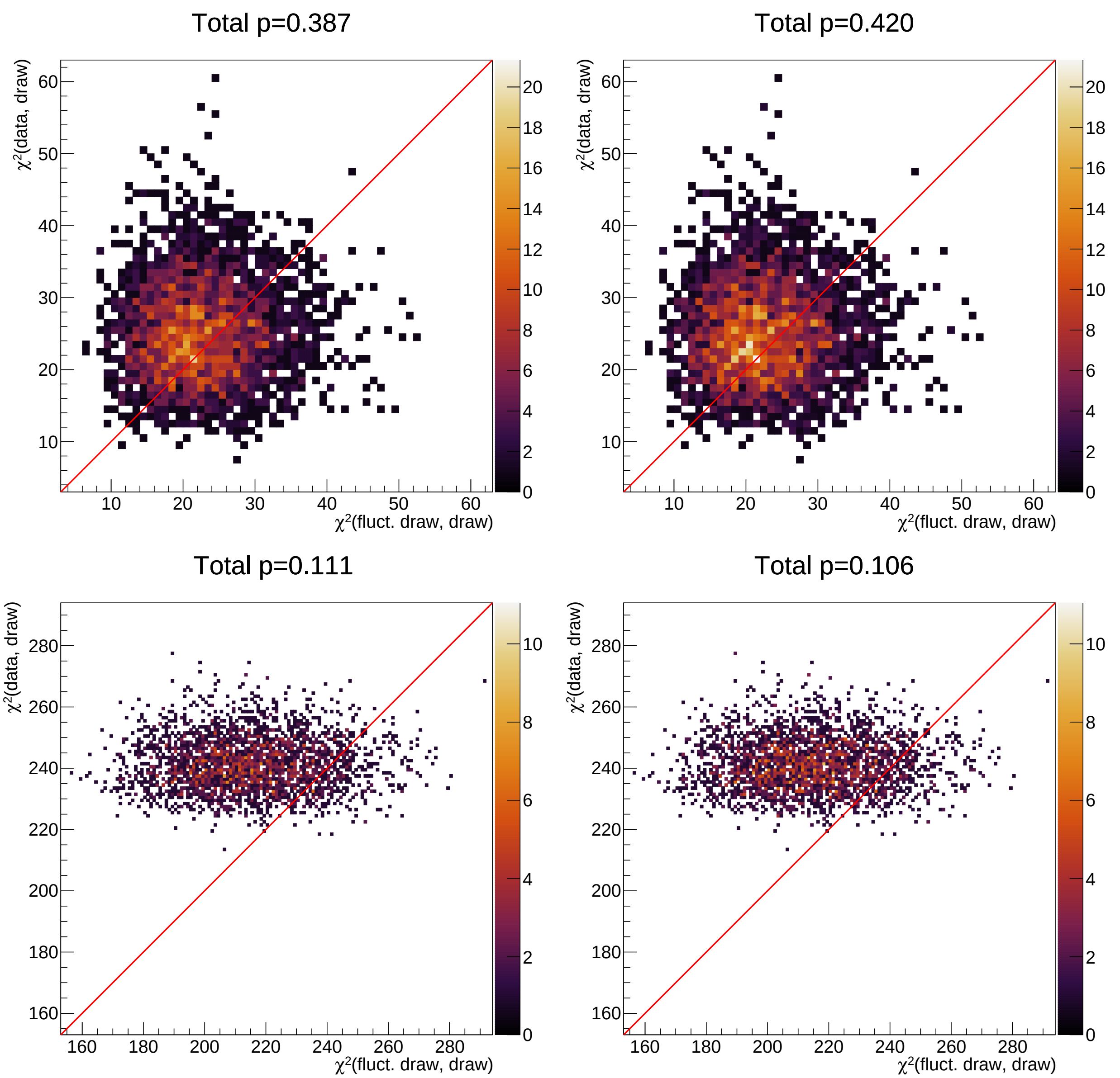

Figure 99: Rate (top) and shape (bottom) based posterior predictive p-values without reactor constraint (left) and with reactor constraint (right), using $E_{\mathrm{rec}} < 2$ GeV for the T2K samples, and $p_{\mathrm{lep}} < 10$ GeV/c for the SK atmospheric samples.

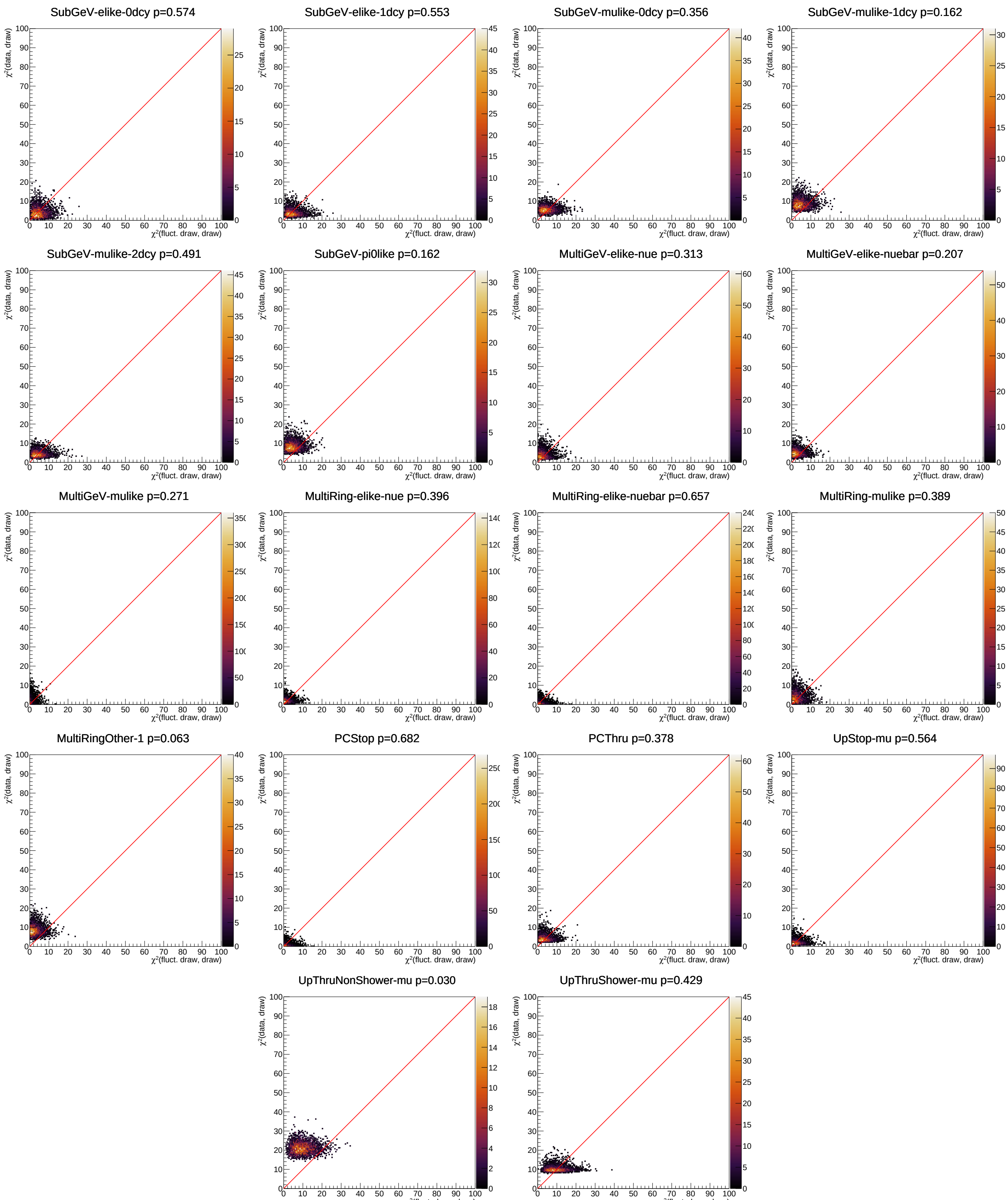

Figure 100: Shape-based posterior predictive p-value without reactor constraint for the SK atmospheric samples, using $p_{\text{lep}} < 10$ GeV/c.

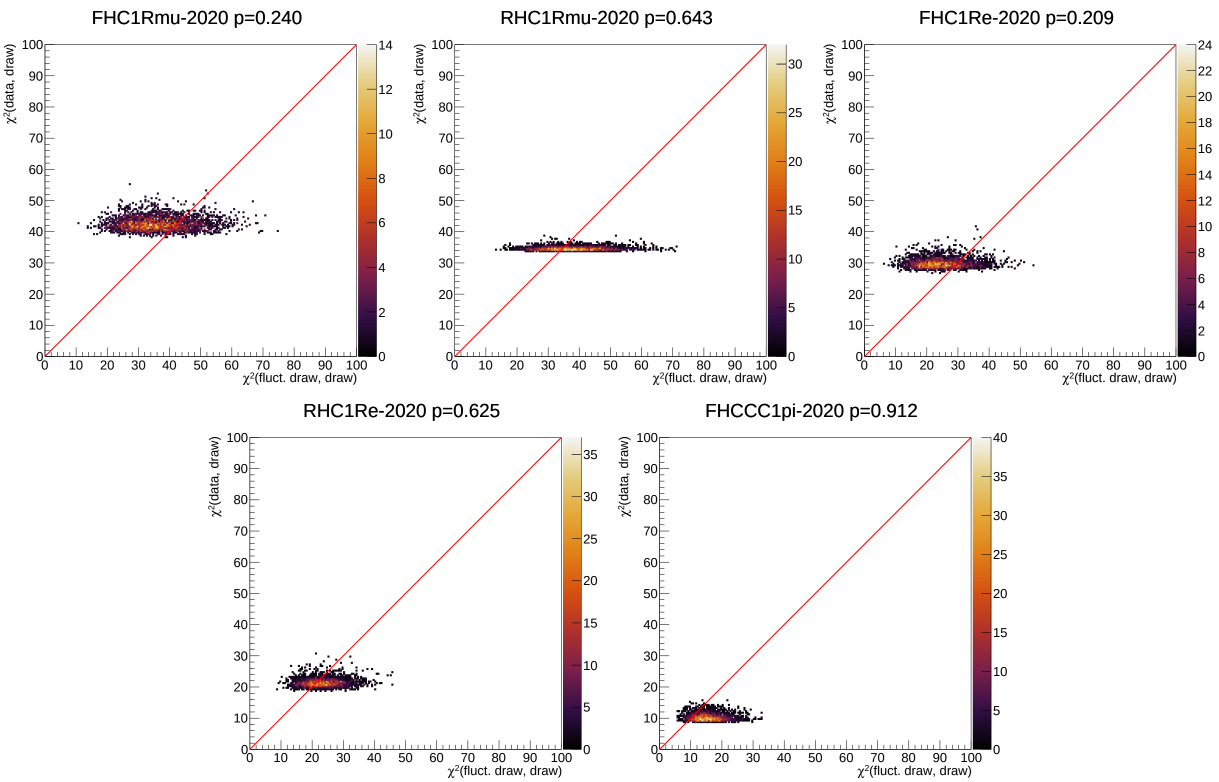

Figure 101: Shape-based posterior predictive p-value without reactor constraint for the T2K beam samples, using $E_{\rm rec} < 2$ GeV.

Sample	Shape, p_{lep}	Shape, $\cos\theta_z$
T2K FHC 1Rmu	0.240	
T2K RHC 1Rmu	0.643	
T2K FHC 1Re	0.209	
T2K RHC 1Re	0.625	
T2K FHC 1Re1de	0.912	
SK SubGeV-elike-0dcy	0.574	
SK SubGeV-elike-1dcy	0.553	
SK SubGeV-mulike-0dcy	0.356	
SK SubGeV-mulike-1dcy	0.162	
SK SubGeV-mulike-2dcy	0.491	
SK SubGeV-pi0like	0.162	
SK MultiGeV-elike-nue	0.313	0.098
SK MultiGeV-elike-nuebar	0.207	0.870
SK MultiGeV-mulike	0.271	0.841
SK MultiRing-elike-nue	0.400	0.622
SK MultiRing-elike-nuebar	0.657	0.630
SK MultiRing-mulike	0.389	0.588
SK MultiRingOther-1	0.063	0.755
SK PCStop	0.682	0.360
SK PCThru	0.378	0.321
SK UpStop-mu	0.564	0.336
SK UpThruNonShower-mu	0.030	
SK UpThruShower-mu	0.429	
Total	0.111	0.322
SK MultiGeV/ring rest.	0.037	0.398

Table 13: Table of shape-based p-values from the data fit for each far-detector sample, where T2K and SK SubGeV samples are projected on E_{rec} and p_{Lep}, respectively, and SK multi-ring and MultiGeV samples are projected on $\cos\theta_z$. The reactor constraint is not applied. For the T2K samples, a $E_{\text{rec}} < 2$ GeV cut is applied, and for the SK samples a $p_{\text{Lep}} < 10$ GeV/c cut is applied.

CW: need text editing

4.6 Systematic constriants

4.6.1 Comparison of prior and posterior constraints in joint-fit

This section shows the prior and posterior constraints of nuisance systematics in the joint-fit. The posterior constraints are extracted from the posterior probability distributions which are produced from $\sim 200M$ steps from the total burn-in steps. Note that due to time limitation and technical reasons, we were not able to merge all steps into one single file and $\sim 20M$ post burn-in steps were not considered. Currently, $200M$ post burn-in steps should be enough to extract the central values and errors for all nuisance systematics. In each plot, the upper panel shows the overlay of the prior (red bands) and posterior (black markers) systematic constraints and the lower panel shows the posterior (black markers) constraints relative to prior constraints (red lines mark the prior constraints). Reactor constraint is applied to the posterior results.

Fig. 102 and Fig. 103 show the comparison for atmospheric flux systematics and T2K beam flux systematics respectively. Fig. 104 shows the comparison for BANFF cross-section systematics. Fig. 105, Fig. 106 and Fig. 107 show the comparison for other cross-section systematics. Fig. 108 shows the comparison for the correlated far detector systematics (upper plot being the SK detector systematics plus two newly developed systematics for e/μ PID, lower plot being the T2K-SK detector systematics).

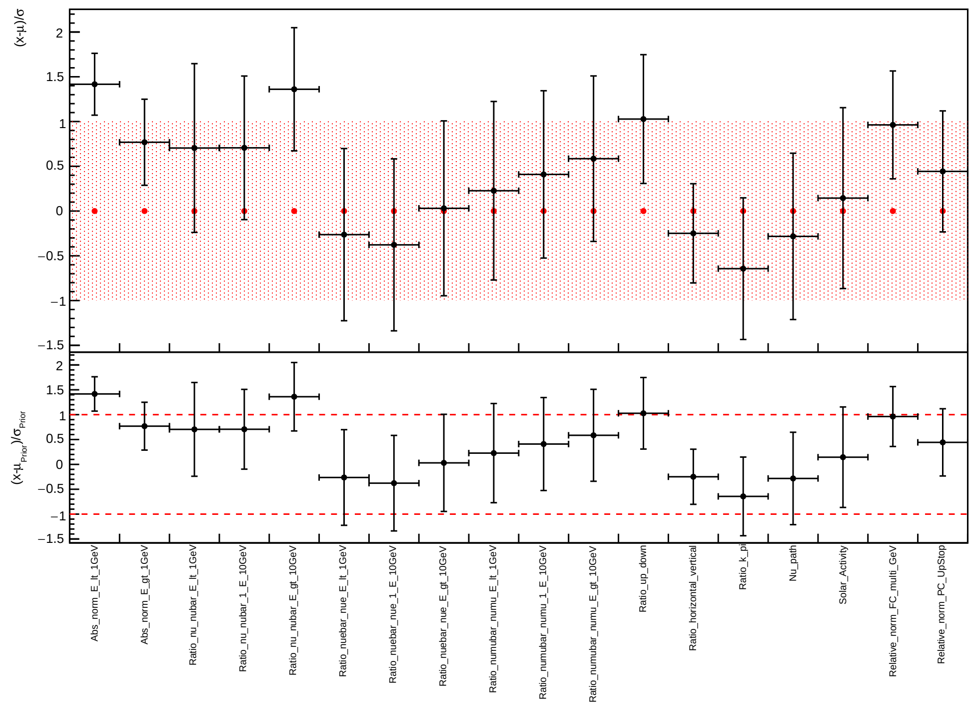

Figure 102: Comparison of prior and posterior constraints of atmospheric flux systematics. The upper panel shows the overlay of central values and error bands of prior constraints (red bands) used in joint-fit and posterior constraints (black markers) from joint-fit with reactor constraint applied. The lower panel shows the posterior constraints relative to the prior constraints. The red dashed line indicate the prior constraints. All the posterior errors are the standard deviations of the posterior probability distributions. Reactor constraint is applied to posterior distributions.

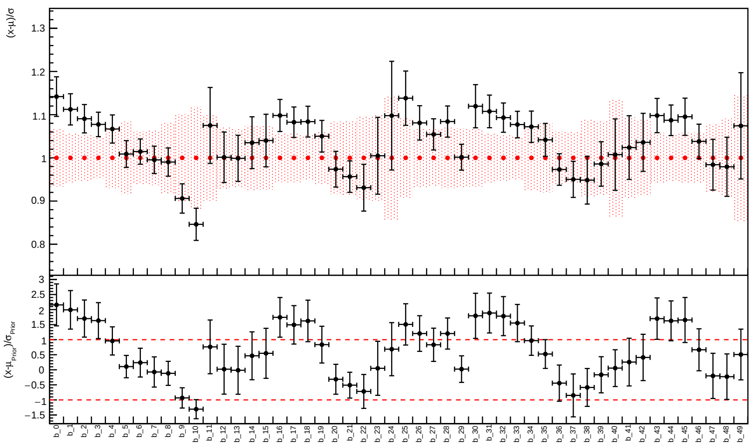

(a) T2K flux systematics at near detector

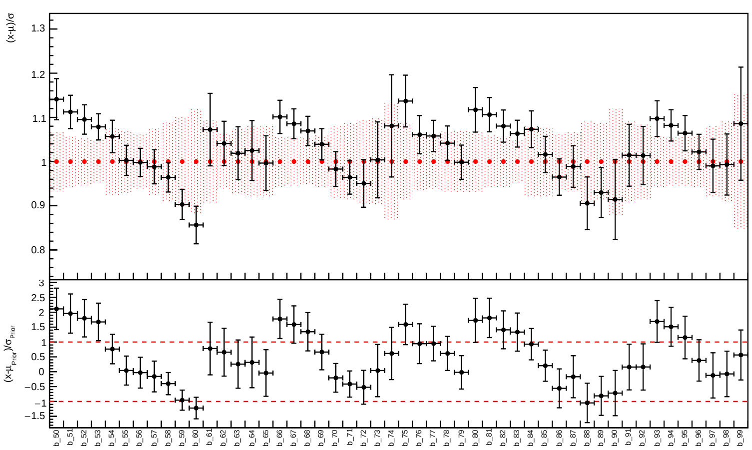

(b) T2K flux systematics at far detector

Figure 103: Comparison of prior and posterior constraints of T2K beam flux systematics. The upper plot shows the beam flux systematics at near detector and the lower shows the beam flux at far detector. For each plot, the upper panel shows the overlay of central values and error bands of prior constraints (red bands) used in joint-fit and posterior constraints (black markers) from joint-fit with reactor constraint applied. The lower panel shows the posterior constraints relative to the prior constraints. The red dashed line indicate the prior constraints. All the posterior errors are the standard deviations of the posterior probability distributions. Reactor constraint is applied to posterior distributions.

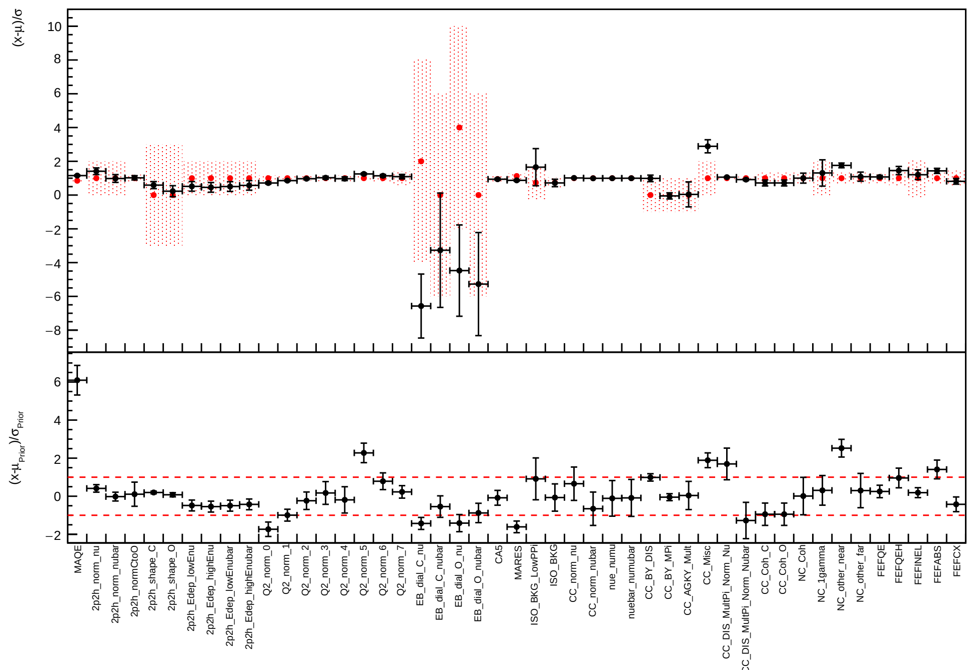

Figure 104: Comparison of prior and posterior constraints of BANFF cross-section systematics. The upper panel shows the overlay of central values and error bands of prior constraints (red bands) used in joint-fit and posterior constraints (black markers) from joint-fit with reactor constraint applied. The lower panel shows the posterior constraints relative to the prior constraints. The red dashed line indicate the prior constraints. All the posterior errors are the standard deviations of the posterior probability distributions. Reactor constraint is applied to posterior distributions.

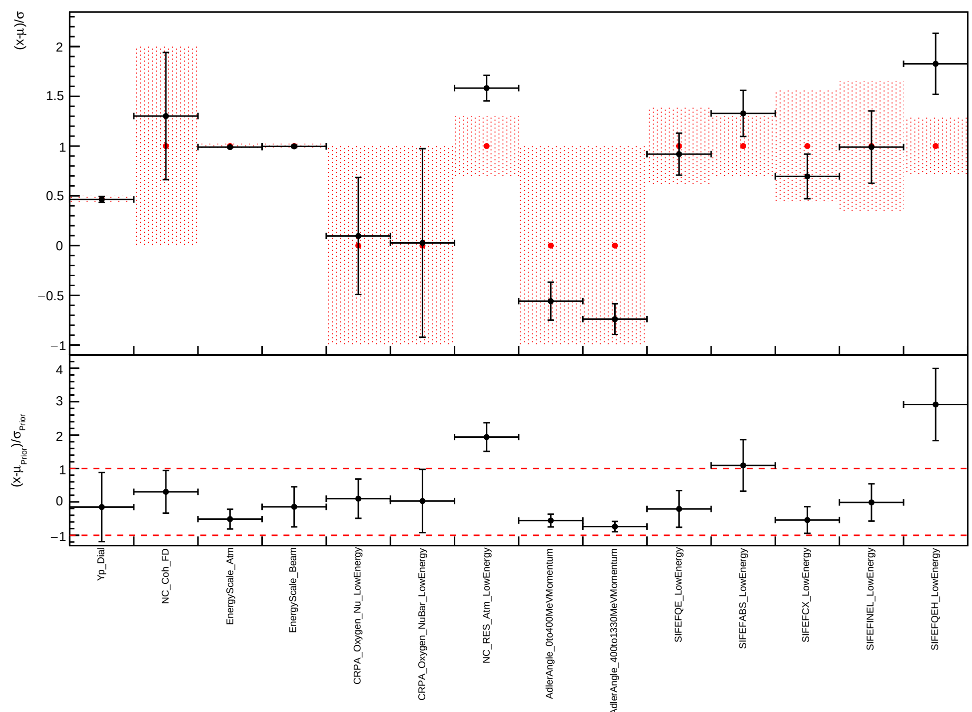

Figure 105: Comparison of prior and posterior constraints of other cross-section systematics (labeled as group 1). This group contains the two newly developed energy scale systematics, two updated Adler angle systematics and 5 SI systematics. The upper panel shows the overlay of central values and error bands of prior constraints (red bands) used in joint-fit and posterior constraints (black markers) from joint-fit with reactor constraint applied. The lower panel shows the posterior constraints relative to the prior constraints. The red dashed line indicate the prior constraints. All the posterior errors are the standard deviations of the posterior probability distributions. Reactor constraint is applied to posterior distributions.

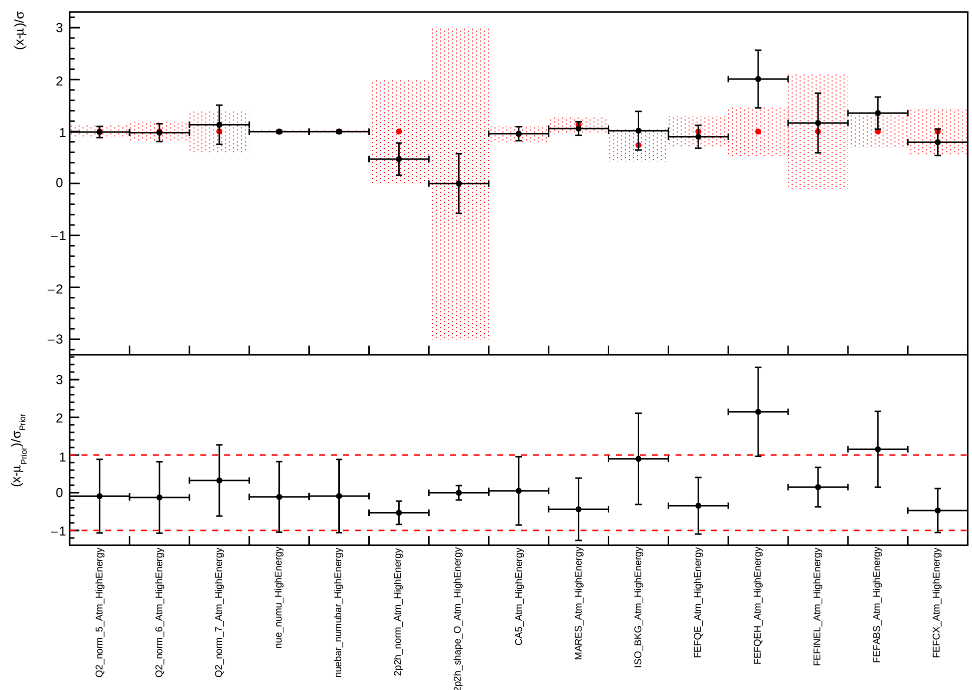

Figure 106: Comparison of prior and posterior constraints of other cross-section systematics (labeled as group 2). This group contains the high energy cross-section systematics which are inspired by the low energy cross-section model. The upper panel shows the overlay of central values and error bands of prior constraints (red bands) used in joint-fit and posterior constraints (black markers) from joint-fit with reactor constraint applied. The lower panel shows the posterior constraints relative to the prior constraints. The red dashed line indicate the prior constraints. All the posterior errors are the standard deviations of the posterior probability distributions. Reactor constraint is applied to posterior distributions.

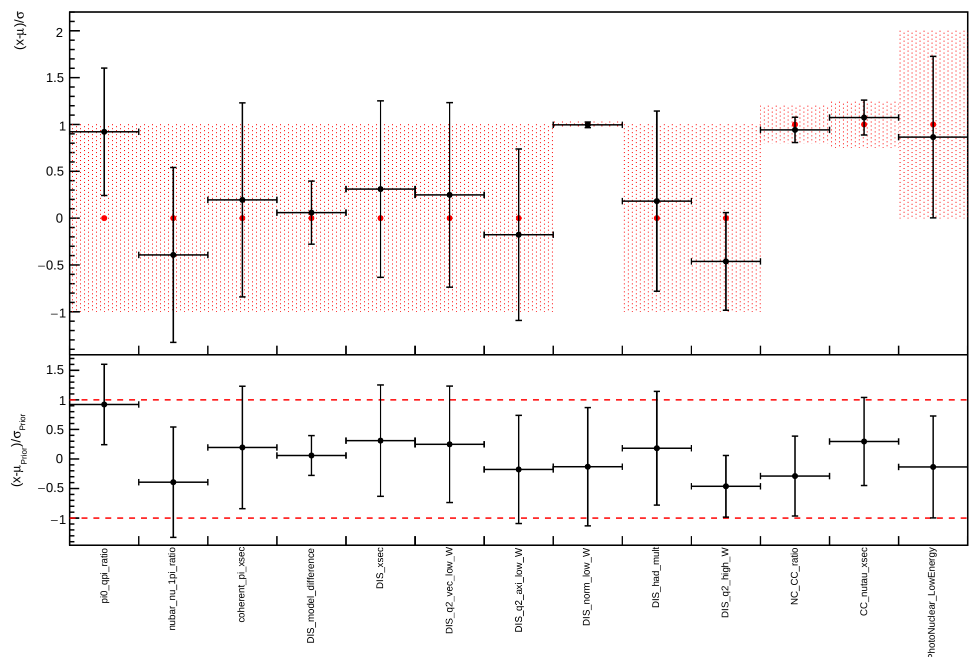

Figure 107: Comparison of prior and posterior constraints of other cross-section systematics (labeled as group 3). This group contains the SK high energy cross-section systematics. The upper panel shows the overlay of central values and error bands of prior constraints (red bands) used in joint-fit and posterior constraints (black markers) from joint-fit with reactor constraint applied. The lower panel shows the posterior constraints relative to the prior constraints. The red dashed line indicate the prior constraints. All the posterior errors are the standard deviations of the posterior probability distributions. Reactor constraint is applied to posterior distributions.

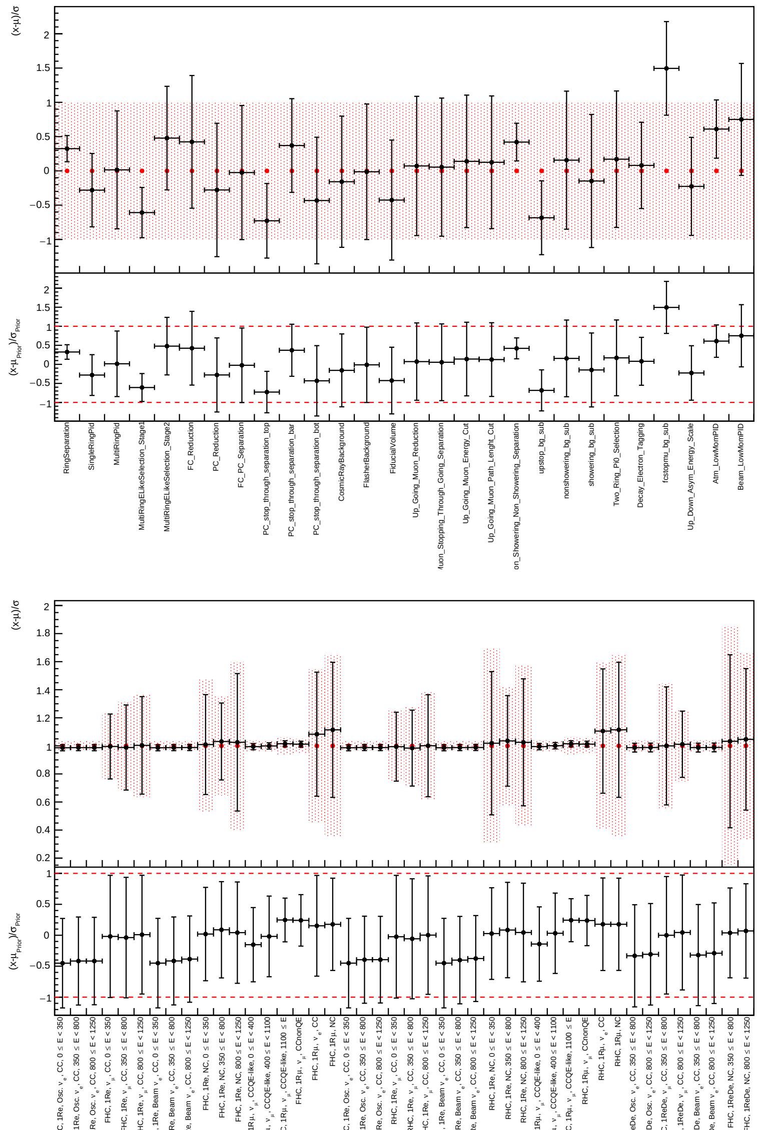

Figure 108: Comparison of prior and posterior constraints of the correlated far detector systematics. The upper plot is the SK detector group plus the Up_Down_Asym_EnergyScale and two newly developed systematics associated with e/μ PID in the low lepton momentum region. The lower plot is the T2K-SK fat detector group. For each plot, the upper panel shows the overlay of central values and error bands of prior constraints (red bands) used in joint-fit and posterior constraints (black markers) from joint-fit with reactor constraint applied. The lower panel shows the posterior constraints relative to the prior constraints. The red dashed line indicate the prior constraints. All the posterior errors are the standard deviations of the posterior probability distributions. Reactor constraint is applied to posterior distributions.

4.6.2 Comparison of posterior constraints from joint-fit and OA2020

This section shows the posterior constraints comparison of nuisance systematics from MaCh3 OA2020 and MaCh3 joint-fit results. For OA2020 results, $\sim 170M$ post burn-in steps are used and the chain files are obtained according to the documentation(https://t2k.org/asg/oagroup/inputs/F oa-inputs/FY19-oa-inputs-list). For joint-fit results, the same post burn-in steps are used as the previous section. In each plot, the upper panel shows the overlay of the OA2020 posterior (red bands) and the joint-fit posterior (black markers) systematic constraints and the lower panel shows the joint-fit posterior (black markers) constraints relative to the OA2020 posterior constraints (red lines mark the OA2020 posterior constraints). Same reactor constraint is applied to both analysis results. Note that only common systematics are compared here, i.e. BANFF cross-section and T2K beam flux.

Fig. 109 shows the comparison for BANFF cross-section systematics. Fig. 110 shows the comparison for T2K beam flux systematics. Not surprisingly, the joint-fit posterior constraints agree well with OA2020 results as MaCh3 joint-fit framework uses OA2020 framework as the basis.

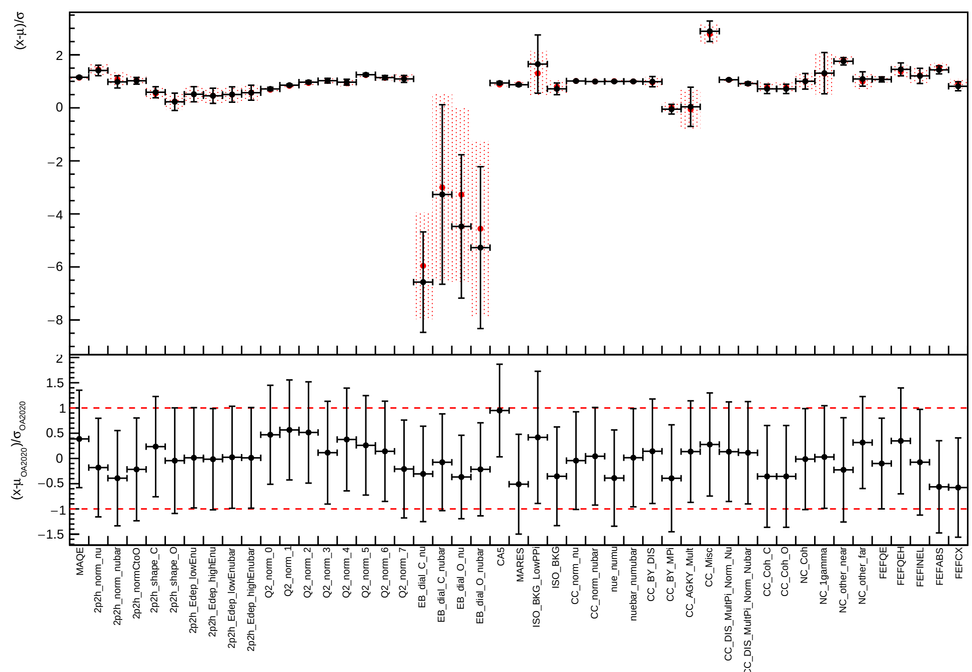

Figure 109: Comparison of posterior constraints from MaCh3 OA2020 and MaCh3 joint-fit for BANFF cross-section systematics. The upper panel shows the overlay of central values and error bands of OA2020 posterior constraints (red bands) and joint-fit posterior constraints (black markers). The lower panel shows the joint-fit posterior constraints relative to the OA2020 posterior constraints. The red dashed line indicate the OA2020 posterior constraints. All the posterior errors are the standard deviations of the posterior probability distributions. Same reactor constraint is applied to OA2020 and joint-fit.

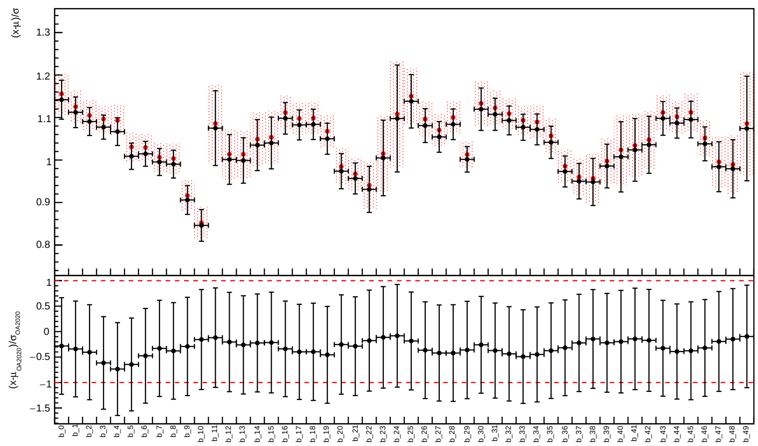

(a) T2K beam flux at near detector

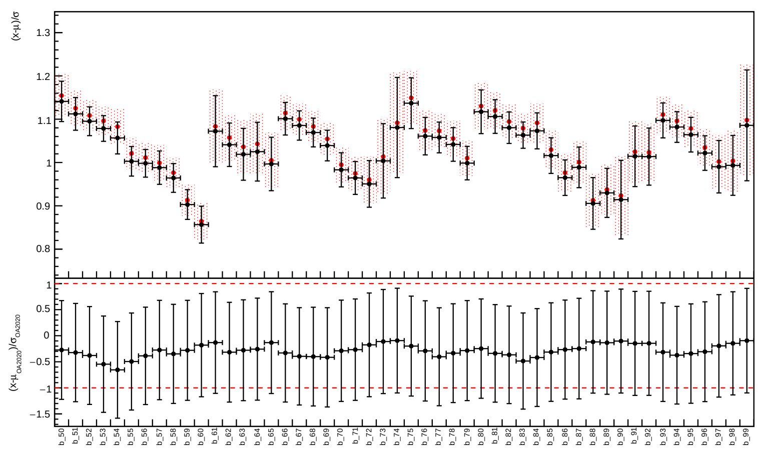

(b) T2K beam flux at far detector

Figure 110: Comparison of posterior constraints from MaCh3 OA2020 and MaCh3 joint-fit for T2K beam flux systematics. In each plot, the upper panel shows the overlay of central values and error bands of OA2020 posterior constraints (red bands) and joint-fit posterior constraints (black markers). The lower panel shows the joint-fit posterior constraints relative to the OA2020 posterior constraints. The red dashed line indicate the OA2020 posterior constraints. All the posterior errors are the standard deviations of the posterior probability distributions. Same reactor constraint is applied to OA2020 and joint-fit.

5 Results comparisons

This section is dedicated to show the comparison of the joint-fit results from MaCh3 and PTheta, the comparison of joint-fit results and T2K official analysis (OA2020) from both MaCh3 and PTheta, and also the investigation of joint-fit results differences between MaCh3 and PTheta. All MaCh3 joint-fit results are produced from post burn-in steps (burn-in being 80,000 steps). All distributions shown in this section have the same reactor constraint applied, which was the same as OA2020.

5.1 Joint-fit results comparison between MaCh3 and PTheta

Parameter constraints Fig. 111, Fig. 112, Fig. 113 and Fig. 114 show the overlay of joint-fit results for δ_{CP}, $\sin^2\theta_{23}$, Δm^2_{32} ($|\Delta m^2_{31}|$) and $\sin^2\theta_{13}$ from MaCh3 and PTheta respectively. Fig. 115 and Fig. 116 are the overlay comparison of Jarlskog invariants using flat prior on δ_{CP} and $\sin\delta_{\text{CP}}$ respectively. Results from PTheta are produced from PTheta MCMC method. Hence, for $\Delta\chi^2$ representation, MCMC results are converted for the purpose of comparisons.

In Fig. 111, PTheta has a stronger constraint on δ_{CP} than MaCh3 for normal ordering with very similar δ_{CP} value for the highest-posterior density. Although the posterior at this value is different, they are almost indistinguishable in the regions of no CP violation ($\delta_{\text{CP}} = 0, \pi$). This was also observed in OA2020 TN393 [1] (Fig. 61). For inverted ordering, the PTheta result shows a shift to higher Δm^2_{32} compared to MaCh3. For either orderings, both fitters exclude $\sin\delta_{\text{CP}} = 0$ at 2σ. A similar observation can be drawn from Fig. 115 and Fig. 116. Fig. 115 shows both fitters exclude $\delta_{\text{CP}} = 0$ at 2σ (see Fig. 49) with a flat prior on δ_{CP}, and PTheta has a stronger constraint. Fig. 116 shows a similar but weaker tendency when there's a flat prior on $\sin\delta_{\text{CP}}$, and PTheta has a slightly stronger constraint.

In Fig. 112, for normal ordering hypothesis, no strong preference to upper/lower octant is seen in either fitter results. For normal ordering, compared with the slightly bimodal contour shape from PTheta, MaCh3 shows a stronger preference for maximal mixing. For inverted ordering, both fitters show a weak preference to the upper octant. However, both results are consistent with each other at 1σ.

For normal ordering in Fig. 113, a consistent shift of the best-fit and credible intervals of PTheta is observed relative to MaCh3. Since PTheta has only $|\Delta m^2_{31}|$ for inverted ordering, MaCh3 results of Δm^2_{32} are converted to $|\Delta m^2_{31}|$ by subtracting $|\Delta m^2_{21}|$ from $|\Delta m^2_{23}|$. A similar shift of Δm^2 also exists for inverted ordering. Potential explanations are documented in Sec. 5.3.

From Fig. 114, it is clear that the results from two fitters use the same reactor constraint.

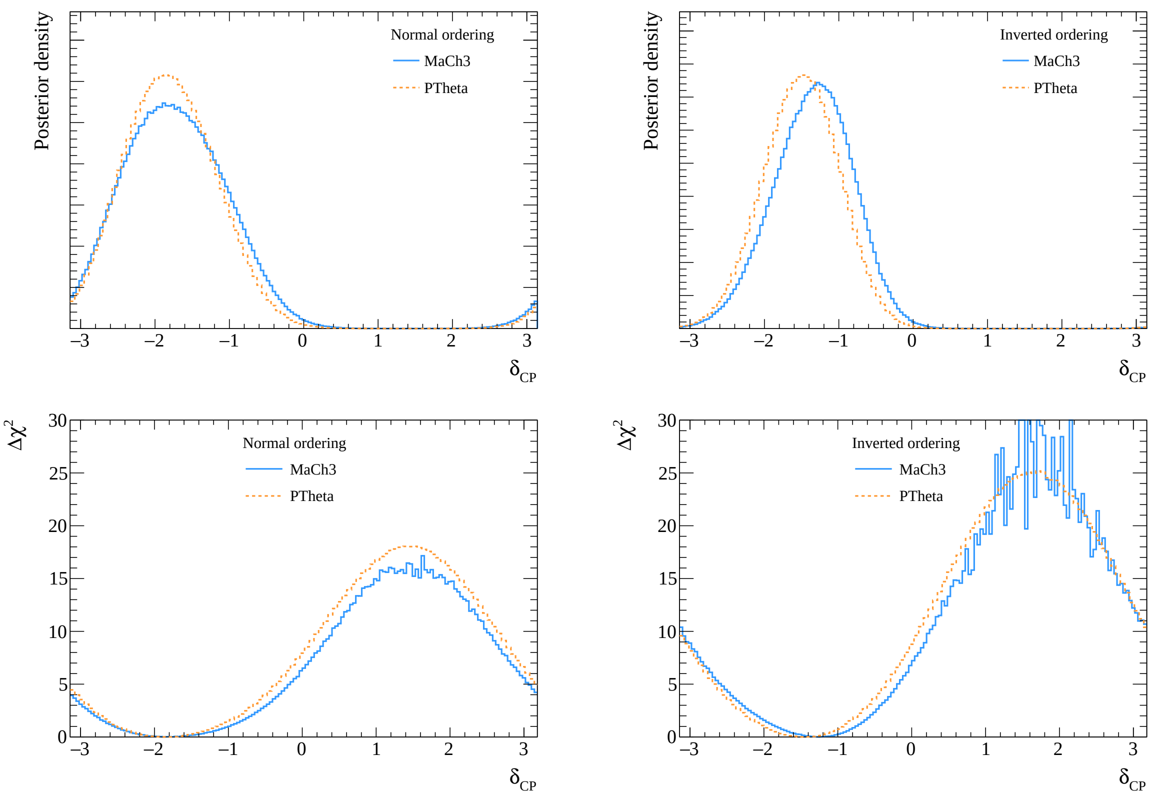

Figure 111: Overlay of δ_{CP} from data fits of MaCh3 (blue solid line) and PTheta (orange dashed line). Upper row shows the posterior probability distributions and lower row shows $\Delta\chi^2$ distributions. Left column shows the normal ordering results and right column shows the inverted ordering results. Same reactor constraint is applied.

Bayes factors for atmospheric parameters Tab. 14 summarises the Bayes factors for octant hypotheses and mass ordering from the joint fit results of MaCh3 and P-Theta. The Bayes factors from the two fitters are quite consistent. In terms of Bayes factor value, both fitters show a weaker preference of one octant over another and both fitters show a stronger preference to normal ordering compared to OA2020 results [1]. The Bayes factor values from both fitters are not sufficient to make a conclusion on hypotheses.

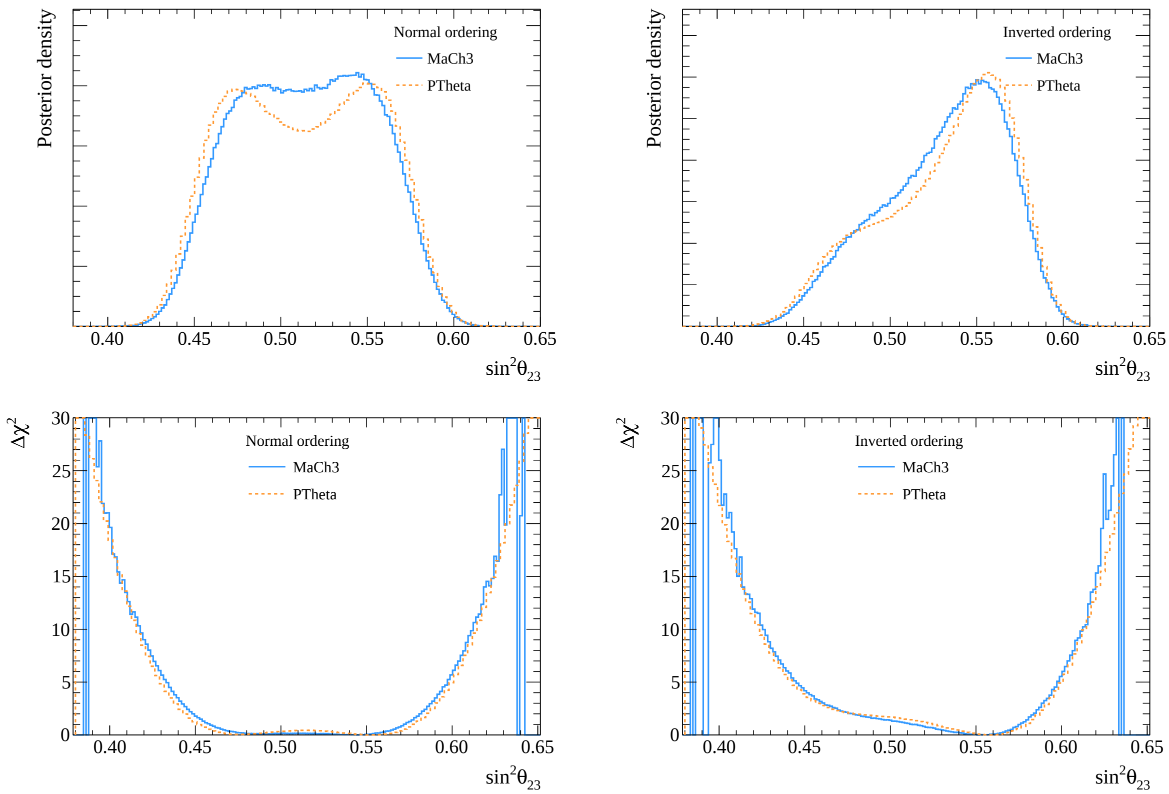

Figure 112: Overlay of $\sin^2\theta_{23}$ from data fits of MaCh3 (blue solid line) and PTheta (orange dashed line). Upper row shows the posterior probability distributions and lower row shows $\Delta\chi^2$ distributions. Left column shows the normal ordering results and right column shows the inverted ordering results. Same reactor constraint is applied.

	MaCh3	P-Theta
B(UO/LO)	1.78	1.57
B(NO/IO)	7.33	8.98

Table 14: Comparison of Bayes factors for the joint fit between MaCh3 and P-Theta. Same reactor constraint and same smearing of $\sin^2\theta_{23}$ are applied to both results. P-Theta results are documented in TN459 [12] Table 5 in v1.1.

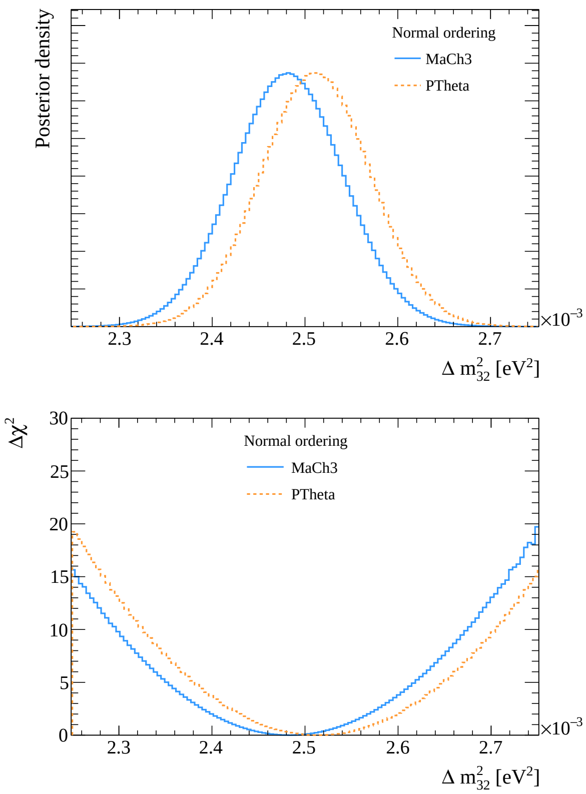

Figure 113: Overlay of Δm^2_{32} and $|\Delta m^2_{31}|$ from data fits of MaCh3 (blue solid line) and PTheta (orange dashed line). Upper row shows the posterior probability distributions and lower row shows $\Delta\chi^2$ distributions. Left column shows the normal ordering results of Δm^2_{32} and right column shows the inverted ordering results of $|\Delta m^2_{31}|$. Same reactor constraint is applied.

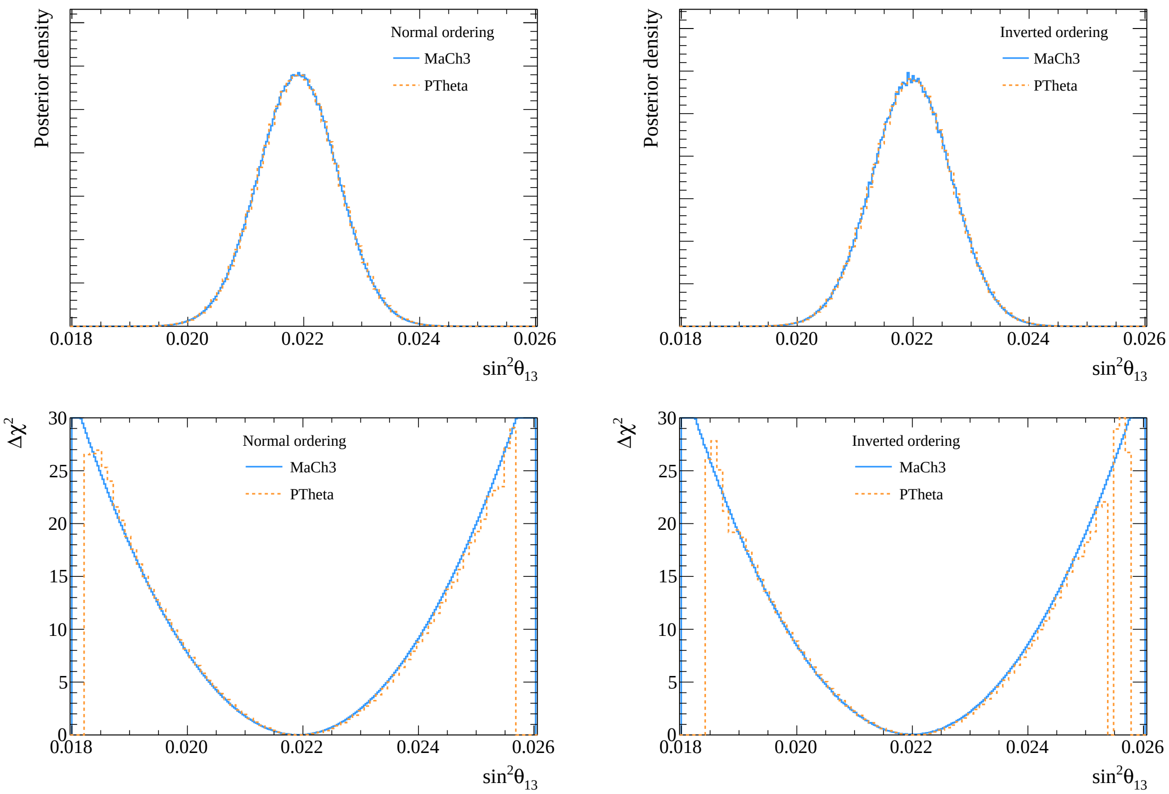

Figure 114: Overlay of $\sin^2\theta_{13}$ from data fits of MaCh3 (blue solid line) and PTheta (orange dashed line). Upper row shows the posterior probability distributions and lower row shows $\Delta\chi^2$ distributions. Left column shows the normal ordering results and right column shows the inverted ordering results. Same reactor constraint is applied.

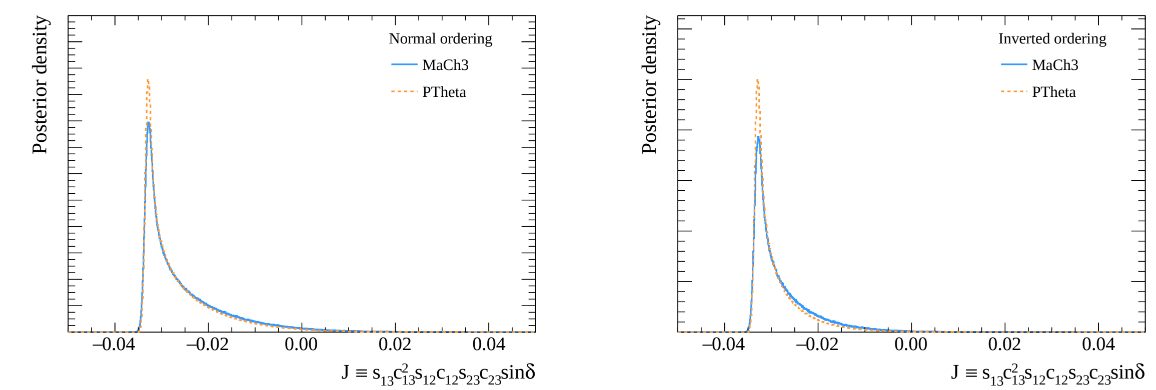

Figure 115: Overlay of J from data fits of MaCh3 (blue solid line) and PTheta (orange dashed line). Left plot shows the normal ordering results and right plot shows the inverted ordering results. Same reactor constraint is applied. Flat prior on $\delta_{\rm CP}$ is assumed.

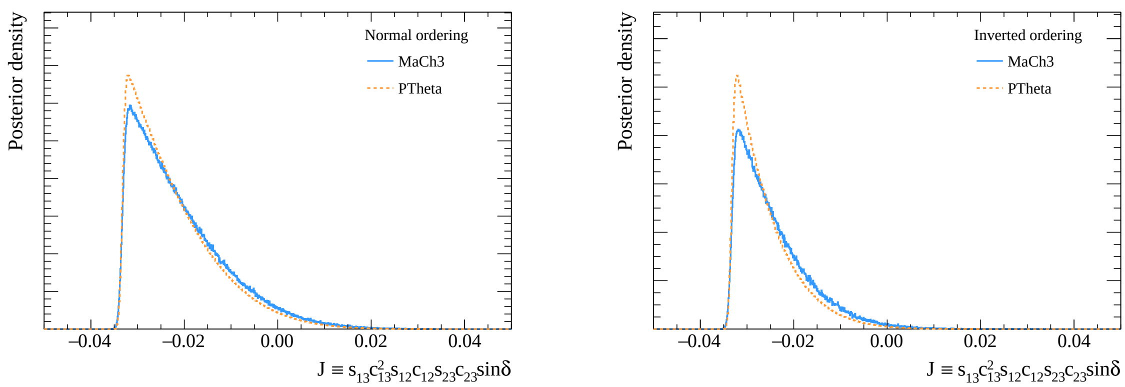

Figure 116: Overlay of J from data fits of MaCh3 (blue solid line) and PTheta (orange dashed line). Left plot shows the normal ordering results and right plot shows the inverted ordering results. Same reactor constraint is applied. Flat prior on $\sin\delta_{\mathrm{CP}}$ is assumed.

5.2 Joint-fit results and OA2020 from MaCh3 and PTheta

Fig. 117, Fig. 118, Fig. 119 and Fig. 120 show the joint-fit results overlaid with T2K official results (OA2020) from MaCh3 and PTheta. MCMC results from MaCh3 are converted to $\Delta\chi^2$ distributions for comparison purpose.

For normal ordering comparison in Fig. 117, both fitters show stronger constraints on $\delta_{\rm CP}$ in the joint-fit compared to T2K-only. MaCh3 joint-fit results are closer to MaCh3 OA2020 results because MaCh3 intended to always strictly follow OA2020 prescriptions, documented in TN393 [1]. The differences of joint-fit P-Theta and OA2020 can be found in TN459 [12] (see Appendix A.1). For normal ordering, both fitters' results from joint-fit can exclude $\sin\delta_{\rm CP} = 0$ at 2σ which shows better constraint compared to OA2020. For inverted ordering, similarly, both fitter results show better constraint than OA2020.

In Fig. 118, for normal ordering and inverted ordering, there is a weaker preference for the upper octant in the joint-fit results (both fitters) compared to OA2020 (both fitters). This behaviour mainly comes from the SK atmospheric samples, as discussed in the P-Theta joint-fit results TN459 [12] (see Fig 21 in v1.1), and can also be seen in 2019 SK oscillation analysis [13]. Especially in normal ordering, both fitters in the joint-fit show a preference of maximal mixing.

For Δm^2 in Fig. 119, the two fitters from OA2020 are very close and MaCh3 results from the joint-fit have the highest posterior density point very close to that from OA2020, but show a weaker constraint than OA2020. This might due to that the joint-fit results adopt a larger smearing on Δm^2_{32} than OA2020. Interestingly, PTheta's results from the joint-fit show a non-negligible shift compared to both OA2020 and joint-fit MaCh3 results. Detailed discussion of this shift of Δm^2_{32} can be found in TN459 [12] (see Appendix A in v1.1).

Fig. 114 shows that the same reactor constraint is applied to the results shown in this section.

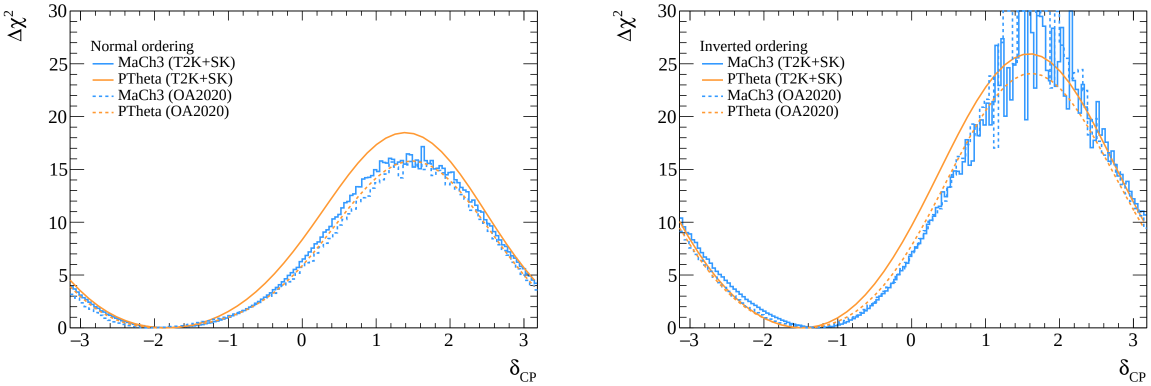

Figure 117: Overlay of δ_{CP} from data fits of joint-fit and T2K official analysis. The solid lines are results from joint-fit and the dashed lines are results from OA2020. Blue lines are MaCh3 results and orange lines are PTheta results. Left plot shows the normal ordering $\Delta\chi^2$ distributions and right plot shows the inverted ordering results. Same reactor constraint is applied.

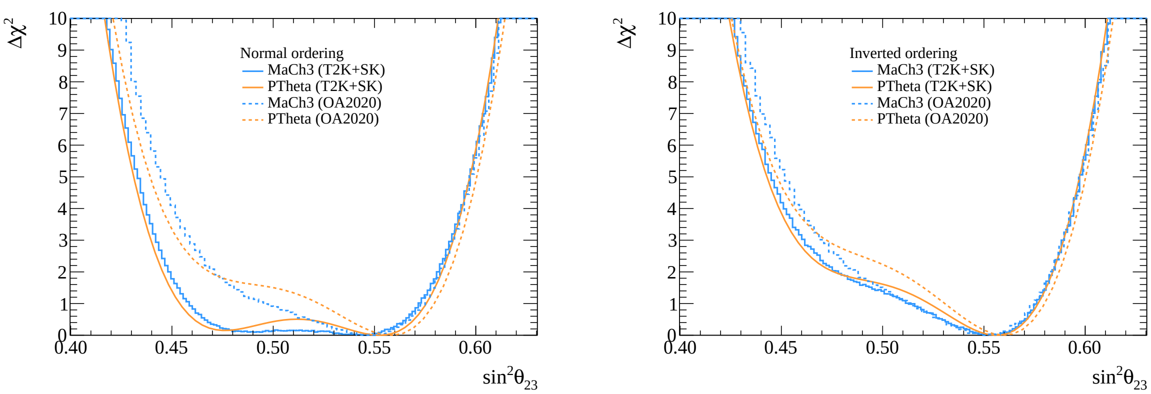

Figure 118: Overlay of $\sin^2\theta_{23}$ from data fits of joint-fit and T2K official analysis. The solid lines are results from joint-fit and the dashed lines are results from OA2020. Blue lines are MaCh3 results and orange lines are PTheta results. Left plot shows the normal ordering $\Delta\chi^2$ distributions and right plot shows the inverted ordering results. Same reactor constraint is applied.

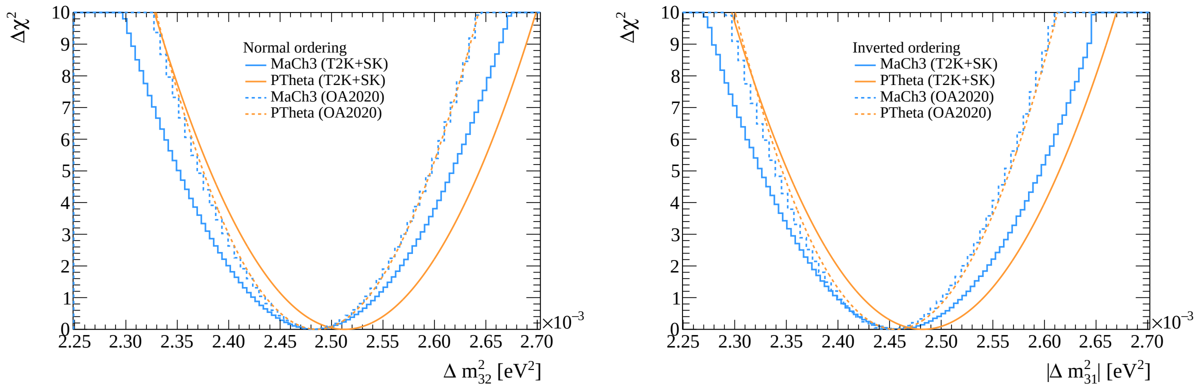

Figure 119: Overlay of Δm^2_{32} and $|\Delta m^2_{31}|$ from data fits of joint-fit and T2K official analysis. The solid lines are results from joint-fit and the dashed lines are results from OA2020. Blue lines are MaCh3 results and orange lines are PTheta results. Left plot shows the normal ordering $\Delta\chi^2$ distributions of Δm^2_{32} and right plot shows the inverted ordering $\Delta\chi^2$ distributions of $|\Delta m^2_{31}|$. Same reactor constraint is applied.

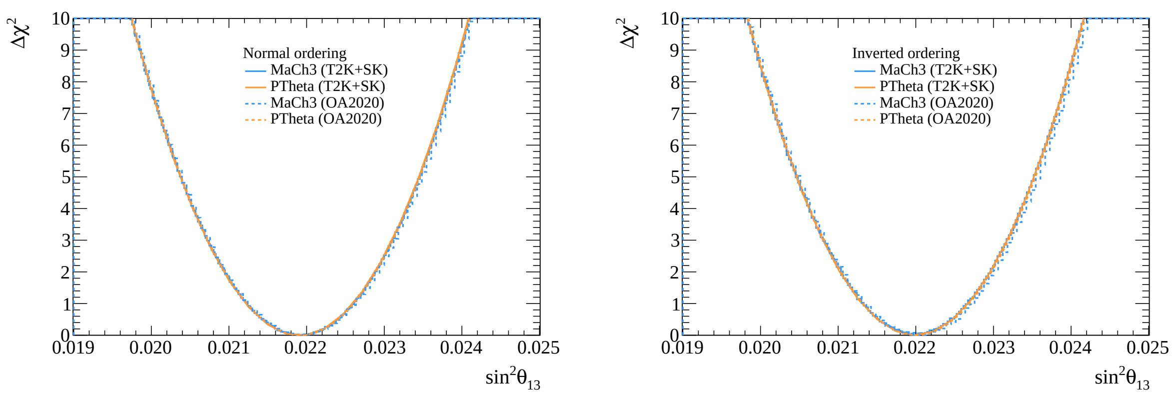

Figure 120: Overlay of $\sin^2\theta_{13}$ from data fits of joint-fit and T2K official analysis. The solid lines are results from joint-fit and the dashed lines are results from OA2020. Blue lines are MaCh3 results and orange lines are PTheta results. Left plot shows the normal ordering $\Delta\chi^2$ distributions and right plot shows the inverted ordering results. Same reactor constraint is applied.

5.3 Potential explanation of results differences

In this section, implementation differences are investigated to understand the differences between the joint-fit results from MaCh3 and PTheta.

Kinematic cut: the order of applying the cut and applying the shifts (e.g. Coulomb correction) to the reconstructed kinematics in the event selections is different in the two fitters. MaCh3 follows the OA2020 style and applies the cut before any corrections, whilst PTheta applies the cut afterwards following the OA2021 approach. When testing this option, PTheta uses the same order as MaCh3 while keeps other implementation unchanged.

E_{rec} **binning:** MaCh3 uses E_{rec} binning for beam μ-like samples and $E_{rec} - \theta$ binning for beam e-like samples while PTheta uses $E_{rec} - \theta$ binning for beam μ-like samples and $p_{rec} - \theta$ for beam e-like samples. When testing this option, PTheta uses the same binning as MaCh3 whilst keeping other implementation choices unchanged.

Kinematic cut + E_{rec} **binning:** to investigate the combined effect of the above two implementation differences, PTheta uses the same implementation as MaCh3 whilst keeping other implementation choices unchanged.

Near detector fit: PTheta and MaCh3 fit near detector samples in different ways. MaCh3 fits near detector samples simultaneously with far detector samples while PTheta uses BANFF inputs to propagate near detector constraints to far detector samples. This has been previously studied in OA2020, as documented in TN393 [1]. Its impact will be studied in the next round of TNs.

Fig. 121, Fig. 122, Fig. 123 and Fig. 124 show the overlays of joint-fit results for the oscillation parameters from MaCh3 and PTheta with different options of implementation described above.

In Fig. 121, PTheta with the same beam sample binning pulls the results towards MaCh3 results while the results with the same kinematic cut implementation cannot explain the fitter results differences very well. The **kinematic cut +** E_{rec} **binning** option shows very similar results compared to E_{rec} **binning** option.

In Fig. 122, similar to Fig. 121, E_{rec} **binning** option pulls PTheta results towards MaCh3 and can thus better explain the differences. The **kinematic cut +** E_{rec} **binning** option shows very similar results compared to E_{rec} **binning** option for inverted ordering.

In Fig. 123, unlike in Fig. 121 and Fig. 122, **kinematic cut** option pulls PTheta results towards MaCh3 the most for both normal and inverted orderings. The **kinematic cut +** E_{rec} **binning** option shows very similar effect as **kinematic cut**. Although the three listed options cannot perfectly explain the shift in Δm^2 for both orderings, they still show

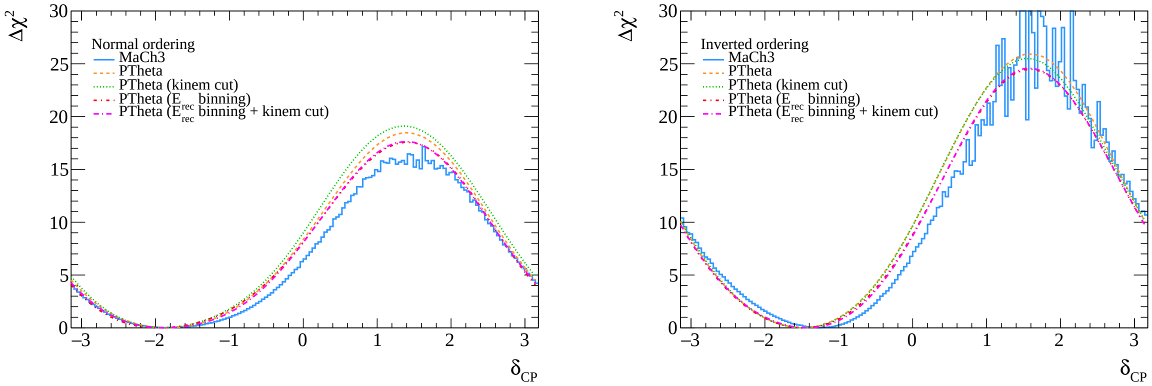

Figure 121: Overlay of δ_{CP} from joint-fit of MaCh3 and PTheta testing different framework implementation options. The solid blue lines are results from MaCh3 joint-fit. The orange dashed lines are results from PTheta joint-fit. The green dashed lines are results from PTheta joint-fit using the same kinematic cut implementation as MaCh3 (i.e.applying the kinematic cut before applying any corrections to the kinematic). The red dashed lines are results from PTheta joint-fit using the same T2K beam sample binnings as MaCh3 (i.e.using E_{rec} rather than p_{rec} for e-like samples). The magenta dashed lines are results from PTheta joint-fit using both the same kinematic cut and same beam sample binnings as MaCh3. Left plot shows the normal ordering $\Delta\chi^2$ distributions and right plot shows the inverted ordering results. Same reactor constraint is applied.

non-negligible influence on the contours.

Fig. 124 confirms the same reactor constraint used in all results shown in this section.

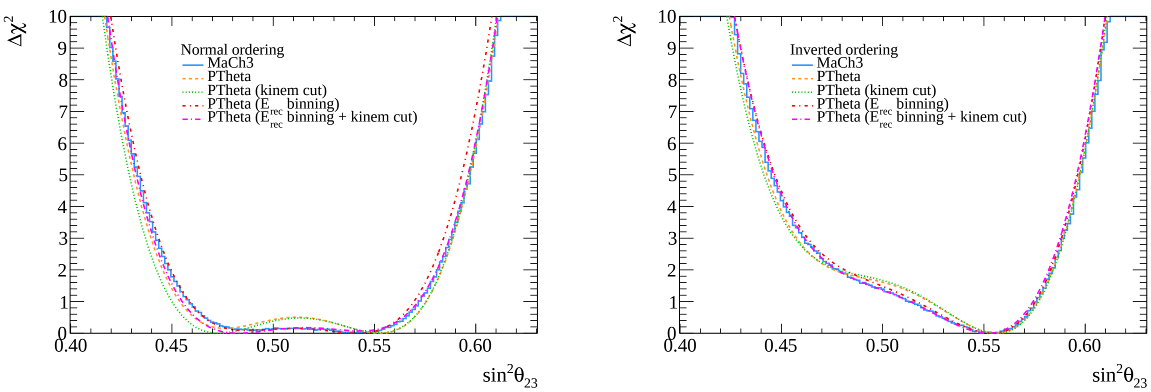

Figure 122: Overlay of $\sin^2\theta_{23}$ from joint-fit of MaCh3 and PTheta testing different framework implementation options. The solid blue lines are results from MaCh3 joint-fit. The orange dashed lines are results from PTheta joint-fit. The green dashed lines are results from PTheta joint-fit using the same kinematic cut implementation as MaCh3 (i.e.applying the kinematic cut before applying any corrections to the kinematic). The red dashed lines are results from PTheta joint-fit using the same T2K beam sample binnings as MaCh3 (i.e.using E_{rec} rather than p_{rec} for e-like samples). The magenta dashed lines are results from PTheta joint-fit using both the same kinematic cut and same beam sample binnings as MaCh3. Left plot shows the normal ordering $\Delta\chi^2$ distributions and right plot shows the inverted ordering results. Same reactor constraint is applied.

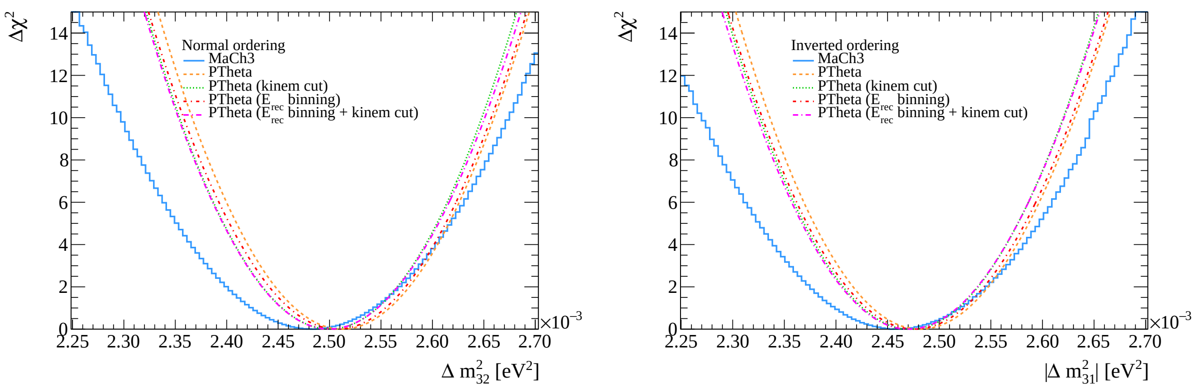

Figure 123: Overlay of Δm^2_{32} and $|\Delta m^2_{31}|$ from joint-fit of MaCh3 and PTheta testing different framework implementation options. The solid blue lines are results from MaCh3 joint-fit. The orange dashed lines are results from PTheta joint-fit. The green dashed lines are results from PTheta joint-fit using the same kinematic cut implementation as MaCh3 (i.e.applying the kinematic cut before applying any corrections to the kinematic). The red dashed lines are results from PTheta joint-fit using the same T2K beam sample binnings as MaCh3 (i.e.using E_{rec} rather than p_{rec} for e-like samples). The magenta dashed lines are results from PTheta joint-fit using both the same kinematic cut and same beam sample binnings as MaCh3. Left plot shows the normal ordering $\Delta\chi^2$ distributions of Δm^2_{32} and right plot shows the inverted ordering $\Delta\chi^2$ distributions of $|\Delta m^2_{31}|$. Same reactor constraint is applied.

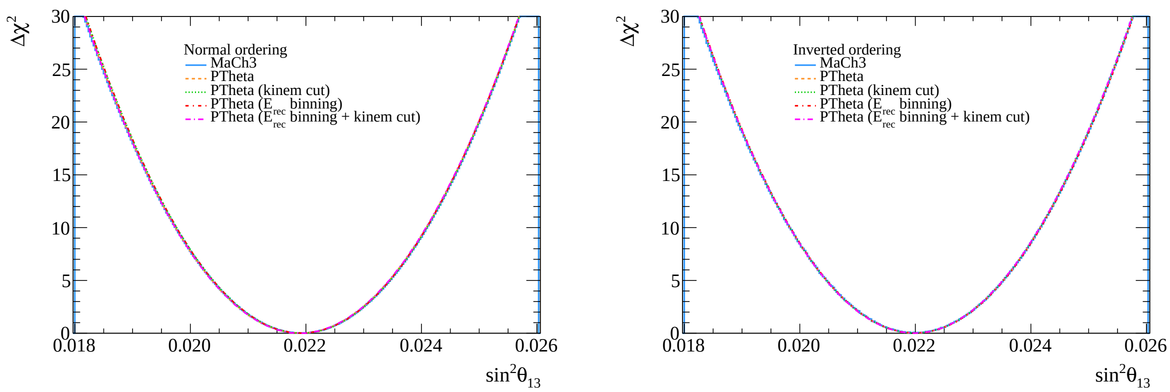

Figure 124: Overlay of $\sin^2\theta_{13}$ from joint-fit of MaCh3 and PTheta testing different framework implementation options. The solid blue lines are results from MaCh3 joint-fit. The orange dashed lines are results from PTheta joint-fit. The green dashed lines are results from PTheta joint-fit using the same kinematic cut implementation as MaCh3 (i.e.applying the kinematic cut before applying any corrections to the kinematic). The red dashed lines are results from PTheta joint-fit using the same T2K beam sample binnings as MaCh3 (i.e.using E_{rec} rather than p_{rec} for e-like samples). The magenta dashed lines are results from PTheta joint-fit using both the same kinematic cut and same beam sample binnings as MaCh3. Left plot shows the normal ordering $\Delta\chi^2$ distributions and right plot shows the inverted ordering results. Same reactor constraint is applied.

5.4 Comparison of the systematic posterior distributions

In this section, we compare the post-fit systematic constraints between MaCh3 and P-theta. We should note that the comparisons shown in this section do not show the effect of correlations between systematic parameters. In addition, some parameters have intrinsic differences at the implementation level. Therefore, even if there are differences in the individual parameter's distribution, it does not necessarily mean that we have a problem in either of the fitters.

To perform this comparison, we construct the MCMC posterior distributions for each systematic using the 200 million post-burn-in steps both for MaCh3 and P-theta. The summary of the mean and variance of each systematic parameter's posterior distribution is shown in Fig. 125.

For the T2K and SK flux systematic parameters, MaCh3 and P-theta distributions agree within 1 post-fit σ ranges. We can see a trend that MaCh3 has larger values of flux systematic parameters in the low-energy region (< 1 GeV). A similar trend was seen in the comparison of near detector constraints of these parameters between MaCh3 and BANFF (Appendix 3 of TN397 [7]). Since these parameters are well constrained by the near detector fit, the differences in the post-fit distributions could also affected by the difference of near detector fit. This can be confirmed once the effect of the near detector fit is studied.

For the T2K detector systematic parameters, we only compare the ones relevant to the μ-like samples because the two fitters use the different binning for the e-like samples (MaCh3 uses E_{rec} binning while P-theta uses momentum binning) and we cannot simply compare the corresponding systematics. These T2K detector systematic parameters show very consistent results between the two fitters, except for the $\nu_e/\bar{\nu}_e$ background components in the μ-like samples (`SK_nu_dis_nue_nueb_CC`, `SK_nubar_nue_nueb_CC`) where MaCh3 has stronger constraints compared to P-theta. We should note that, as described in Section 6.6 of TN422 [5], P-theta includes the secondary interaction (SI) systematics not as the independent dials but as the combined effect in the detector systematics. On the other hand, MaCh3 implements these systematics as independent dials, and therefore the detector systematics do not include the effect of SI in MaCh3. These different treatments of SI systematics could cause the differences seen in the T2K detector systematic parameters. Among the other T2K and SK detector systematics, the SI systematics (`SI_*`) and the energy-scale systematics (`SK_p_scale`, `SK_atm_p_scale`, `UpDown_Asymmetry_Energy_Scale`) also show some differences. These systematic parameters are implemented in different ways and are known to behave differently due to the different implementation philosophies of both fitters.

The cross-section systematics in the high-energy model and the new cross-section systematics introduced in the joint analysis have very consistent distributions between MaCh3 and P-theta. The low-energy cross-section systematics show some differences, but they mostly agree within 1 post-fit σ ranges. The posterior distributions of selected cross-section systematics are shown in Fig. 126. Similarly to the T2K flux systematics, these distributions show a similar trend with the near detector constraints of these parameters between MaCh3 and BANFF (Appendix 3 of TN397 [7]). Therefore, these differences could be further understood once the effect of the near detector fit is studied.

In conclusion, we have observed some differences in the systematic posterior distributions but these differences are thought to be understandable level considering the different implementations of each systematic between MaCh3 and P-theta.

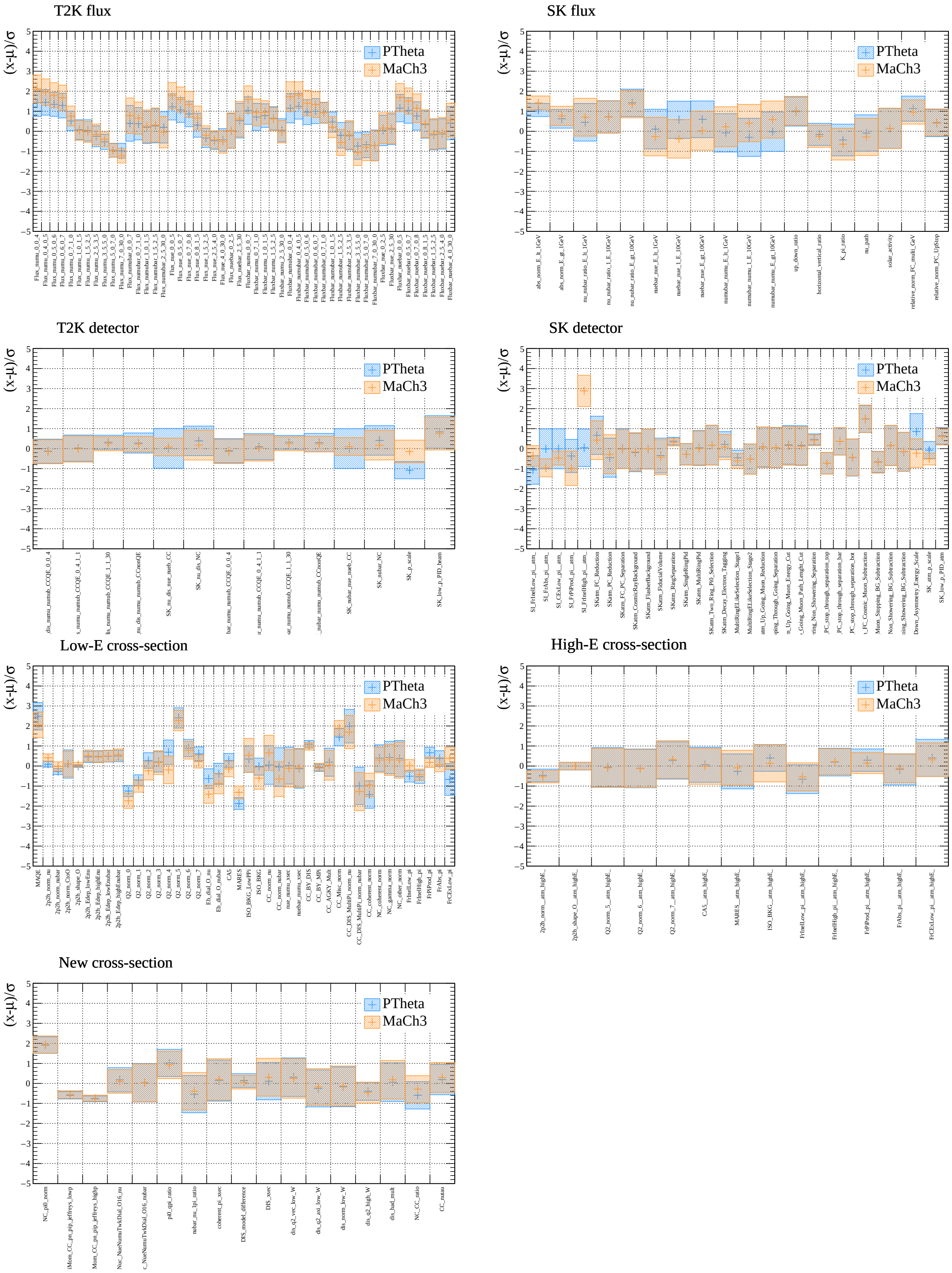

Figure 125: Comparison of the post-fit systematic constraints between MaCh3 and P-theta computed from the MCMC posterior distributions. The center and error of each parameter error band show the arithmetic mean and variance of posterior distributions. The parameter values are normalized using their prior mean and variance.

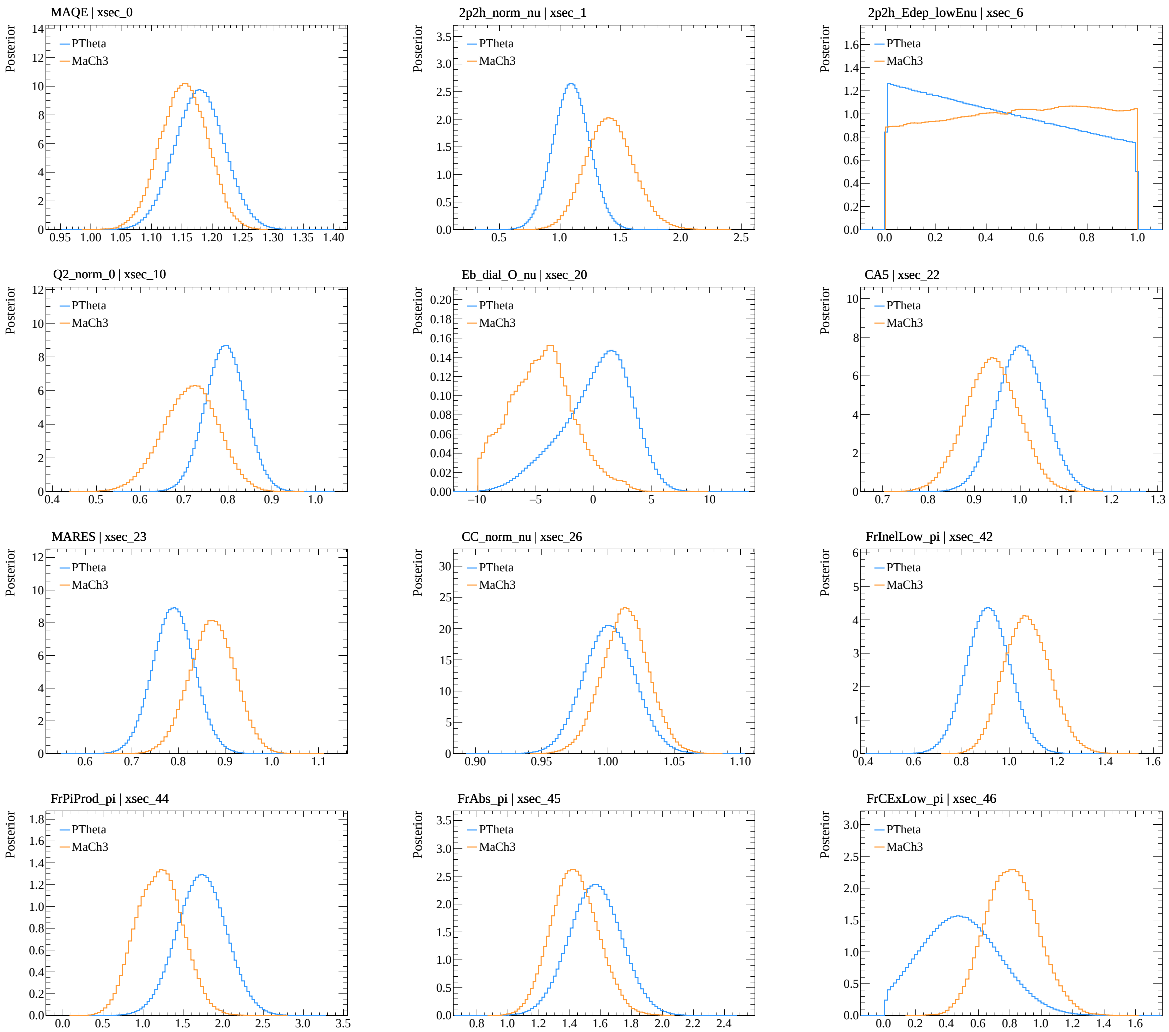

Figure 126: Comparison of the posterior distributions for selected cross-section systematic parameters between MaCh3 and P-theta. The parameter values are **not** normalized with their prior mean and variance.

6 Summary

This technical note presented the joint analysis of SK atmospheric neutrinos and T2K beam neutrinos with the MaCh3 framework, with model updates in TN456 [6]. Analyses of Asimov data (set A) and the real data were presented, simultaneously fitting the near detector samples and far detector samples (5 T2K beam samples and 18 SK atmospheric samples) using Markov chain Monte Carlo to sample the posterior probability in systematic phase space.

For both the Asimov A and real data analyses, results were presented with and without the reactor constraint on $\sin^2\theta_{13}$ applied. All results were smeared with Δm^2_{32} by 3.6×10^{-5} eV^2 from the fake-data studies. For each fit, one dimensional and two dimensional oscillation parameter contours were produced, and Bayes factors of octant hypotheses, mass ordering and CP violation were calculated. For the data fit, the posterior predictive spectra (both with and without reactor constraint) were compared to the data spectra and the corresponding posterior predictive p-values (total p-value and by-sample p-values) were extracted. The data fit results were also compared to the MaCh3 analysis in OA2020 and to P-Theta results in the joint fit and OA2020.

Mass ordering For the Asimov A fit, the Bayes factor of normal ordering over inverted ordering B(NO/IO) is 7.26(3.98) with(out) the reactor constraint applied. For the data fit, the Bayes factor of normal ordering over inverted ordering B(NO/IO) is 7.33(3.76) with(out) the reactor constraint applied. Compared to T2K OA2020 MaCh3 results, the Bayes factor B(NO/IO) is 4.2(1.8) with(out) the reactor constraint applied. Although none of the values reach a level of significance where conclusions could be drawn to exclude either possibilities of the mass ordering, we can still see an enhancement of substantial evidence of normal ordering over inverted ordering according to Jeffrey's scale [14].

CP violation For the Asimov A fit, the Bayes factor $B[(\sin\delta_{\mathrm{CP}} < 0)/(\sin\delta_{\mathrm{CP}} \geq 0)]$ is 24.5(6.3) with(out) the reactor constraint applied. For the data fit, the Bayes factor $B[(\sin\delta_{\mathrm{CP}} < 0)/(\sin\delta_{\mathrm{CP}} \geq 0)]$ is 50.0(10.5) with(out) the reactor constraint applied. From the δ_{CP} contours of data fit with reactor constraint, $\delta_{\mathrm{CP}} = 0$ can be easily excluded between 2σ and 3σ credible intervals. Hence, from both the contours and Bayes factor values, joint-fit results show support for CP violation neutrinos.

$\sin^2\theta_{23}$ **octant** For the Asimov A fit, the Bayes factor of upper octant over lower octant $B(\mathrm{UO/LO})$ is 2.72(1.67) with(out) the reactor constraint applied. For the data fit, the Bayes factor of upper octant over lower octant $B(\mathrm{UO/LO})$ is 1.78(0.82) with(out) the reactor constraint applied. Compared to OA2020 MaCh3 results [1], joint-fit data fit results show a weaker preference of upper octant.

References

[1] E. Atkin et al. "Measuring PMNS parameters in a joint ND280-SK analysis using MCMC". In: *T2K Technical Note* 393 (2020).

[2] D Barrow et al. "SK atmospheric T2K beam joint fit technical note, MaCh3 details". In: *T2K Technical Report* 426 (2022).

[3] Roger Wilking Michael Wilking Cris Vilela. "Event Selection and Detector Systematic Uncertainties for the SK+T2K Joint Fit". In: *T2K Technical Report* 428 (2021).

[4] D. Barrow et al. "Oscillation probability calculation for the T2K+SK atmospheric joint fit". In: *T2K Technical Note* 425 (2021).

[5] C. Bronner et al. "Flux and interaction models for the T2K-SK atmospheric joint fit". In: *T2K Technical Note* 422 (2021).

[6] L. Berns et al. "T2K+SK atmospheric joint analysis: model updates for the data fit". In: *T2K Technical Note* 456 (2023).

[7] L. Berns et al. "P-theta 2020 Run 1-10 Joint-fit Analysis". In: *T2K Technical Note* 397 (2020).

[8] A. Eguchi et al. "Fitter validations for joint T2K+SK atmospheric Asimov fits". In: *T2K Technical Note* 471 (2023).

[9] L. Munteanu et al. "Constraining the Flux and Cross Section Models with Data from ND280 using FGD1 and FGD2 for the 2020 Oscillation Analysis". In: *T2K Technical Note* 395 (2020).

[10] M. Tanabashi et al. "Review of Particle Physics". In: *Phys. Rev. D* 98 (2018), p. 030001.

[11] A. Eguchi et al. "Fake data studies for the T2K+SK atmospheric joint analysis". In: *T2K Technical Note* 457 (2023).

[12] L. Berns et al. "P-theta SK+T2K joint analysis". In: *T2K Technical Note* 459 (2023).

[13] M Jiang et al. "Atmospheric neutrino oscillation analysis with improved event reconstruction in Super-Kamiokande IV". In: *Progress of Theoretical and Experimental Physics* 2019.5 (May 2019). ISSN: 2050-3911. DOI: 10.1093/ptep/ptz015. URL: http://dx.doi.org/10.1093/ptep/ptz015.

[14] H. Jeffreys. "The theory of probability". In: *UOP Oxford* (1998).